UNIVERSITY OF SOUTHERN CALIFORNIA

DEPARTMENT OF CIVIL ENGINEERING

STATIC, DYNAMIC AND ROTATIONAL COMPONENTS OF
STRONG EARTHQUAKE SHAKING NEAR FAULTS

by

M. Dravinski and M.D. Trifunac

Report No. CE 79-06

Los Angeles, California

October, 1978

ABSTRACT

SH and Love waves in homogeneous isotropic linear and elastic layered medium are considered. Roots (wave numbers) of the corresponding frequency equation are complex in general, thus implying solution in terms of progressing waves and locally standing waves, which decay exponentially with increasing distance from the source. Using the orthogonality of characteristics functions, the displacement field due to a vertical strike-slip dislocation is evaluated in closed form. The results can be summarized as follows:

1) Displacement and rotation spectra exhibit greater sensitivity to the depth of the source as number of layers increases.

2) Contribution of locally standing waves to the total energy density spectrum is significant within a distance which is of the order of the thickness of the top layer.

3) In case of a single layer, the time displacement field due to locally standing waves at the surface $z=0$ can be neglected for $x > 2h_1$, where x and h_1 represent the distance from the source and the thickness of the layer, respectively.

4) The average ratio of progressing rotation spectra vs. product of displacement spectra and frequency, remains constant for a wide range of frequencies. The same ratio is strongly frequency-dependent for locally standing waves.

1.1 Introduction

To improve current design criteria for structures close to the active faults, it is worthwhile to explore the details of strong ground motion there by means of simple analytical models. At present, the numerical methods (e.g., finite elements) do not seem suitable for modeling high frequency (f > 1 Hz, short wavelength) motions. Insufficient observational knowledge of the high frequency faulting phenomena and strong ground motion in the near field, and lack of suitable high frequency analytical solutions do not permit critical testing of approximate numerical schemes. Simple, exact analytical solutions, on the other hand, have the advantage that the results depend explicitly on selected physical parameters so that relative importance of different characteristics of the problem can be evaluated directly.

One approach to analytical solutions, for example, is by the method of Green's functions. However, as pointed out by Anderson and Trifunac (1977), much work remains to be done to compute realistic Green's functions for use in strong motion seismology. The exact three-dimensional velocity structure of the earth is not known. It is, however, so complicated that the exact Green's function might not be of practical engineering use. Therefore, a typical procedure is to find a simplified model which approximates the earth structure. For some simple models, the Green's function is evaluated exactly. For more complicated ones, only approximate Green's functions can be

used. For the case of an infinite, homogeneous elastic space, the Green's function is simple so integration in time can be performed analytically (Haskell, 1969). The layered half-space model for the earth represents a better approximation. However, it is considerably more difficult to calculate the Green's function in this case (Apsel, et. al., 1977). Consequently, for integrating ground motions, only certain approximations have been studied to date (e.g., Helmberger, 1974 considers the low frequency approximations only). For additional references, the reader is referred to the paper by Anderson and Trifunac (1977).

At present, the functional form of attenuation of displacement (velocity, acceleration) amplitudes near the source remains unsolved. Correlation studies (Trifunac and Brady, 1976) indicate that most investigators agree on what should be, say, the amplitude of peak acceleration for distance range between 20 and 200 km from the source. For distances less than 20 km, there is significant disagreement, reflecting the lack of data there and uncertainties associated with extrapolation. At small distances, say 1 km, these differences are as large as one order of magnitude (Trifunac and Brady, 1976).

The precise nature of the attenuation of the ground displacement (velocity, acceleration) field versus distance depends upon numerous parameters such as, for example, geological properties of the model, fault dimension, wave frequency, acceleration (displacement) amplitude and the characteristics of the recording site. Thus, the attenuation will be possible to determine empirically only when many more strong

ground motion records become available. Until then, the only alternative is seen in developing models which could provide sufficient information about the nature of attenuation in the near-field.

The description of the near-field attenuation calls for a study of static and dynamic parts of the displacement field near the source. The waves in a multilayered half-space consist of body and surface waves, the latter being either progressive or locally standing ones (corresponding wave numbers being real or complex) (Achenbach, 1973; para. 6). The locally standing waves produce the so-called static part of the displacement field and decay exponentially with increasing distance from the source. However, in the immediate vicinity of the source, their contribution to strong shaking may be significant. Therefore, it is of interest to examine the nature of both static and dynamic fields as functions of distance from the source and frequency. The problem can be solved in multilayered half-space by solving the corresponding frequency equation (Haskell, 1953) for roots which are complex in general. Then, by using the orthogonality of modes (Alsop, 1966; McGarr, et. al., 1967; Herrera, 1964) the displacement field due to a dislocation, and corresponding frequency spectra, can be evaluated in closed form.

The purpose of this report is to analyze the nature of strong shaking near a long vertical strike-slip fault by means of an exact analytical solution. By emphasizing the nature of amplitude attenuation with distance and by analyzing the relationship of torsional motions to translational motions, it is possible to devise a number of

useful results for future estimation of strong earthquake shaking in the near field.

Recent advances in computational methods for structural response to strong shaking (Newmark and Rosenblueth, 1971) have emphasized the need for evaluation of rotational components of ground motion in the near-field and their relation to the displacement field as a function of distance from the source and frequency. At the present time, no rotation spectra in the near-field due to dislocation at a fault seems to be available in literature.

1.2 Statement of Problem

The model considered in this work (Figure 1) consists of n homogeneous isotropic layers which extend to infinity along the y-axis. The layers are bonded to a rigid half-space. A prescribed antisymmetric displacement field is applied at x=0 uniformly along the y-axis. The resulting displacement field is of the antiplane-strain type and is given by $u_x = u_z = 0$ and $u_y = v$. The displacement input can be expressed as

$$v^i = v(x=0^+,z,\omega) = g(z)F(\omega)e^{-i\omega t} \qquad (1.1)$$

where the functions $g(z)$ and $F(\omega)$ are known.

Steady state wave motions in the layered medium for $x \geq 0$ are then governed by

$$\left(\nabla^2 + \frac{\omega^2}{\beta^2}\right)v = 0 \quad , \qquad \nabla^2 \equiv \partial^2/\partial x + \partial^2/\partial z^2$$

$$x \in (0,\infty)$$

$$z \in [0,z_n] \qquad , \qquad (1.2)$$

where $\beta(z)$ represents the shear wave velocity, ω is the circular frequency, and $z_n = \sum_{m=1}^{n} h_m$, with h_m being the thickness of the mth layer. By symmetry of the model and antisymmetric excitation at $x=0^+$, the resulting wave motion becomes antisymmetric with regards to x=0. Hence, from this point and on, the motions for $x \geq 0$ are studied only.

Since the top surface of the layered medium is stress-free and the bottom is perfectly bonded to the half-space, the boundary conditions are

$$\frac{\partial v(x,0,\omega)}{\partial z} = 0 \qquad (1.3)$$
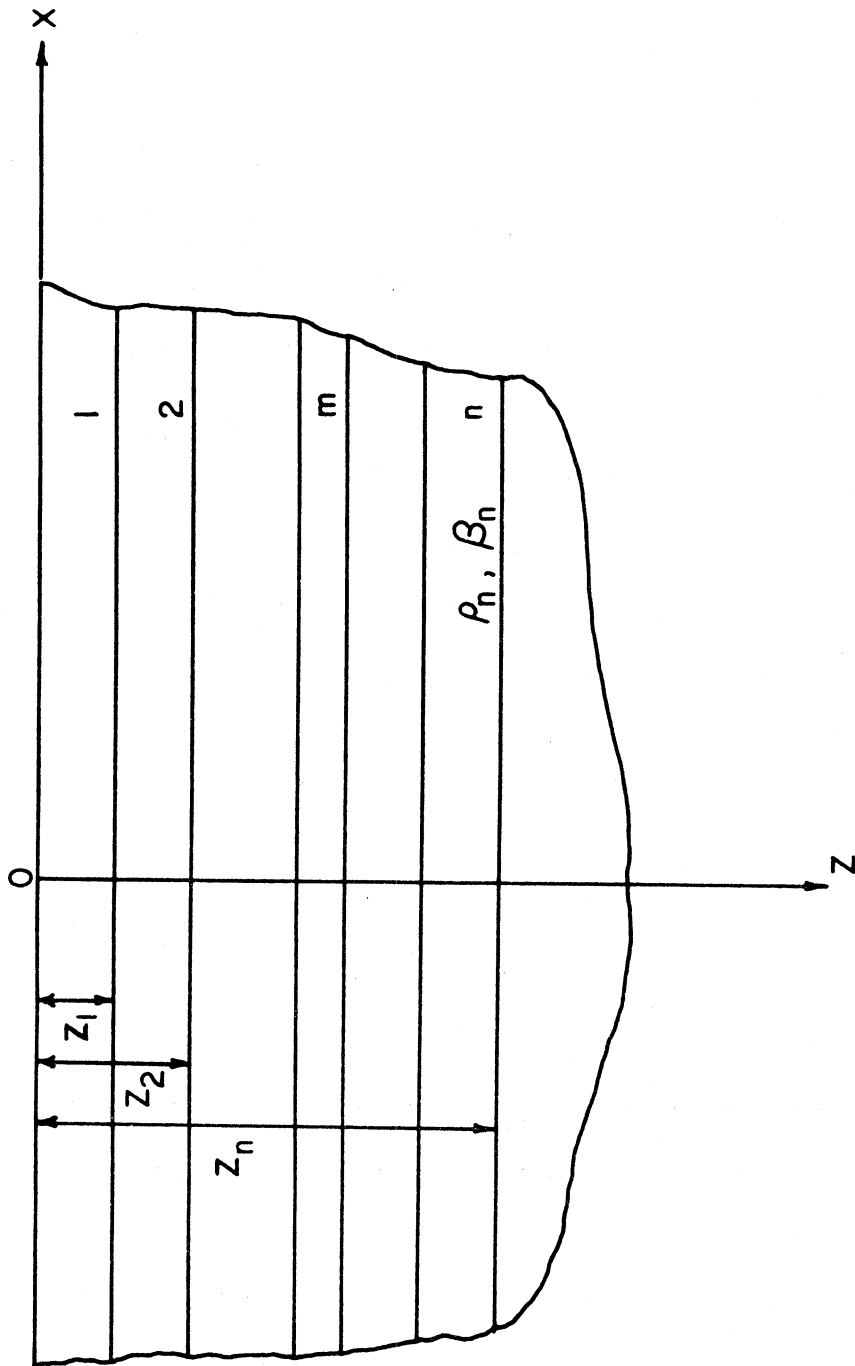
Figure 1. Model Geometry

$$v(x,z_n,\omega) = 0 \tag{1.4}$$

Along each interface between the layers, one requires perfect bonding, i.e.,

$$v(x,z_m^-,\omega) = v(x,z_m^+,\omega) \tag{1.5}$$

$$\mu_m \frac{\partial v(x,z_m^-,\omega)}{\partial z} = \mu_{m+1}\frac{\partial v(x,z_m^+,\omega)}{\partial z} \ , \tag{1.6}$$

$$\left.\begin{array}{c}\\\\\end{array}\right\} \quad m=1,2, \ldots, n-1$$

where the superscripts - and + denote that z_m is approached from below or above, respectively, and μ is the shear modulus.

1.3 Solution of Problem[1]

A solution of equation of motion is assumed to be of the form

$$v(x,z,\omega) = \phi(z)e^{ikx} \quad , \tag{1.7}$$

where k represents the wave number, function $\phi(z)$ is yet to be determined, and the factor $\exp(-i\omega t)$ is omitted for brevity. Substituting (1.7) into (1.2), there follows

$$\phi(x) = \begin{cases} a_1\cos q_1 z + b_1\sin q_1 z & , \ 0 \leq z \leq z_1 \\ a_2\cos q_2 z + b_2\sin q_2 z & , \ z_1 \leq z \leq z_2 \\ \ \vdots & \ \ \ \vdots \qquad \qquad \vdots \\ a_n\cos q_n z + b_n\sin q_n z & , \ z_{n-1} \leq z \leq z_n \quad , \end{cases} \tag{1.8}$$

where

$$q_m^2 \equiv \frac{\omega^2}{\beta_m^2} - k^2 \quad , \quad m=1,2,\ldots,n \quad . \tag{1.9}$$

The q_m can be either real and positive or pure imaginary and positive for m=1,2,3, ..., n. These assumptions are discussed in more detail later.

1.3.1 Frequency Equation

In view of (1.8) the displacement and stress in the mth layer are given by

$$v(x,z,\omega) = (a_m\cos q_m z + b_m\sin q_m z)e^{ikx}$$

$$z_{m-1} \leq z \leq z_m$$

$$m=1,2,\ldots,n \tag{1.10}$$

---

[1] The alternate approach is outlined in Appendix A.

$$\sigma_{yz}(x,z,\omega) = \mu_m q_m(-a_m \sin q_m z + b_m \cos q_m z)e^{ikx} \tag{1.11}$$

with μ being the shear modulus. The origin of the coordinate system (x,y,z) in the mth layer is next placed temporarily at $z = z_{m-1}$ (Haskell, 1963) and the elastodynamic state (Achenbach, 1973; para. 6) is denoted by

$$\underset{\sim}{V} = \begin{bmatrix} v \\ \sigma_{yz} \end{bmatrix} . \tag{1.12}$$

The elastodynamic states at the top and the bottom of the mth layer at $x=0$ are specified by

$$\underset{\sim}{V}_{m-1} = \begin{bmatrix} a_m \\ \mu_m q_m b_m \end{bmatrix} \tag{1.13}$$

$$\underset{\sim}{V}_m = \begin{bmatrix} a_m \cos q_m h_m + b_m \sin q_m h_m \\ \mu_m q_m(-a_m \sin q_m h_m + b_m \cos q_m h_m) \end{bmatrix} . \tag{1.14}$$

From the last two expressions, the relation between elastic states at the bottom and the top of the mth layer is given by

$$\underset{\sim}{V}_m = \underset{\sim}{A}_m \underset{\sim}{V}_{m-1} \quad , \qquad m=1,2, \ldots, n$$

$$\underset{\sim}{A}_m = \begin{bmatrix} \cos q_m h_m & \dfrac{\sin q_m h_m}{\mu_m q_m} \\ -\mu_m q_m \sin q_m h_m & \cos q_m h_m \end{bmatrix} \tag{1.15}$$

Similarly, for $(m-1)^{th}$ layer, it follows

$$\underset{\sim}{V}_{m-1} = \underset{\sim}{A}_{m-1} \underset{\sim}{V}_{m-2} \quad , \qquad m=2, \ldots, n \quad . \tag{1.16}$$

The continuity of elastodynamic states specified through (1.5) and (1.6) implies

$$\underset{\sim}{V}_m^+ = \underset{\sim}{V}_m^- \quad , \qquad\qquad m=1,2, \ldots, n-1 \quad , \qquad\qquad (1.17)$$

where the superscripts - and + denote that z_m is approached from below and above, respectively. Therefore, (1.15) and (1.16) give

$$\underset{\sim}{V}_m = \underset{\sim}{A}_m \underset{\sim}{A}_{m-1} \underset{\sim}{V}_{m-2} \quad , \qquad\qquad m-1,2, \ldots, n \quad . \qquad\qquad (1.18)$$

By applying the above procedure repeatedly, it follows that

$$\underset{\sim}{V}_n = \underset{\sim}{A} \underset{\sim}{V}_0 \quad , \qquad\qquad\qquad (1.19)$$

where $\underset{\sim}{A}$ is a 2×2 matrix defined by

$$\underset{\sim}{A} = \underset{\sim}{A}_n \underset{\sim}{A}_{n-1} \cdots \underset{\sim}{A}_1 \quad , \qquad\qquad\qquad (1.20)$$

And A_m is given by (1.15). The subscript "o" denotes surface x=0.

The use of boundary conditions (1.3) and (1.4) in (1.19) implies

$$A_{11} = 0 \quad , \qquad\qquad\qquad (1.21)$$

and this becomes the frequency equation for the problem under consideration. Therefore, for a given circular frequency ω, equation (1.21) provides a set of the wave numbers $\{k_j\}$, j=1,2, ... This set represents the eigenvalues of the equation of motion. The corresponding eigenfunctions are given by $\phi(z)$ in (1.7).

As an illustration, the frequency equations for the cases of one and two layers are studied in detail.

1.3.1.1 Single Layer

In this case, the frequency equation (1.21) reduces to

$$\cos q_1^j h_1 = 0 \quad , \qquad\qquad\qquad (1.22)$$

with

$$\left(q_1^j\right)^2 \equiv \frac{\omega^2}{\beta_1^2} - k_j^2 \qquad\qquad j=1,2, \ldots . \qquad\qquad (1.23)$$

In a normalized form, equation (1.22) becomes

$$\Omega^2 - \kappa_j^2 - \left[\frac{(2j-\pi)}{2}\right]^2 \quad , \qquad j=1,2,3, \ldots , \qquad (1.24)$$

where dimensionless circular frequency Ω and wave number κ_j are defined by

$$\Omega \equiv \frac{\omega h_1}{\beta_1} \quad ; \quad \kappa_j \equiv k_j h_1 \quad . \qquad (1.25)$$

Throughout the analysis, the circular frequency ω is assumed to be real. Therefore, for the wave number positive real or pure imaginary, the frequency equation reduces to a family of hyperbolae or circles, respectively. The positive real wave numbers represent surface Love waves while the positive pure imaginary wave numbers represent locally standing waves (Achenbach, 1973; para. 6) which rapidly diminish with x.

The cut-off frequencies where the wave number changes from real to imaginary are given by $\Omega = (2j-1)/2$, j=1,2, ... It is seen from Figure 2 that for $\Omega < \pi/2$ no progressive wave exists and only a localized standing wave motion can take place. It can also be seen that at a frequency greater than the first cut-off frequency only a finite number of progressive modes will propagate through the elastic medium $x \geq 0$. At the same frequency, there will be infinitely many solutions of the frequency equation that correspond to locally standing waves.

1.3.1.2 Two Layers

In the case of two layers, the frequency equation (1.21) becomes

$$\cos q_1^j h_1 \cdot \cos q_2^j h_2 - \frac{\mu_1 q_1^j}{\mu_2 q_2^j} \sin q_1^j h_1 \cdot \sin q_2^j h_2 = 0 \qquad (1.26)$$
$$j=1,2, \ldots ,$$
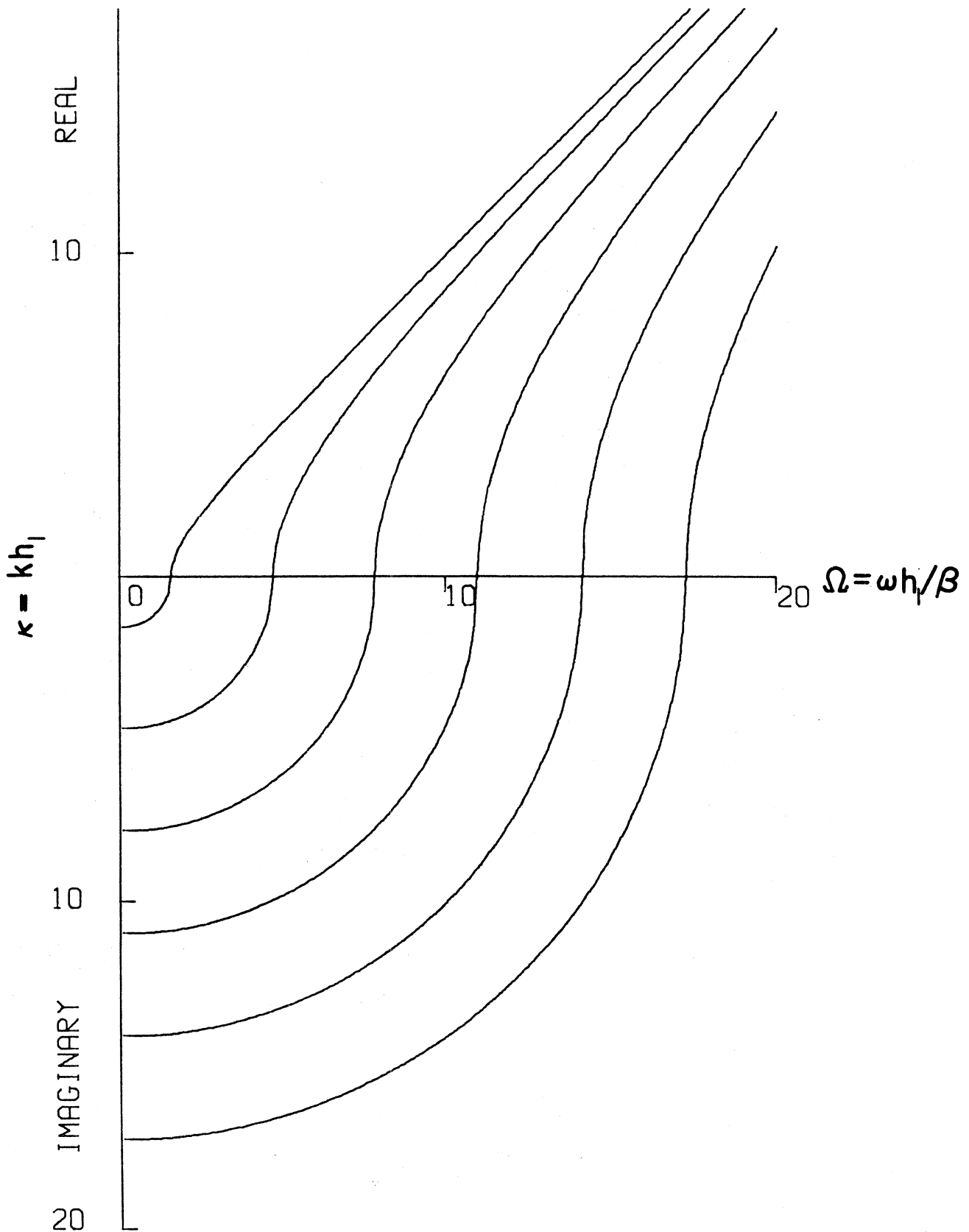
Figure 2. Dispersion Curves for Single Layer ($\beta_1 = \rho_1 = h_1 = 1$)

$$\left(q_m^j\right)^2 \equiv \frac{\omega^2}{\beta_m^2} - k_j^2 \quad , \qquad \begin{array}{l} m=1,2, \\ j=1,2, \ldots, \end{array} \tag{1.27}$$

Furthermore, it is assumed that $\beta_1 < \beta_2$. It is easy to show that for $0 < k_j < \omega/\beta_1$ the frequency equation is satisfied with real k_j. For $k_j = \omega/\beta_1$, the frequency equation becomes

$$\cosh \sqrt{k_j^2 - \omega^2/\beta_2^2}\, h_2 = 0 \quad . \tag{1.28}$$

The last equation can be satisfied only if $\sqrt{k_j^2 - \omega^2/\beta_2^2}$ is pure imaginary. For k_j real this can be true only if $k_j < \omega/\beta_2$ which is contradictory to the assumption $k_j = \omega/\beta_1 > \omega/\beta_2$. However, for k_j pure imaginary (1.28) holds. Similar arguments can be applied for $k_j > \omega/\beta_1$. Therefore, the real roots of the frequency equation are obtained for the range of the wave numbers $0 < k_j < \omega/\beta_1$.

Using dimensionless frequency $\Omega \equiv \omega h_1/\beta_1$ and wave number $\kappa_j \equiv k_j h_1$, the dispersion curves for the case of the two layers are presented in Figures 3 and 4. Examples of the dispersion curves for three and four layers are presented in Figures 5 through 8.

For progressing waves in each model, the wave motion at the top layer consists of plane waves reflecting from the faces of the layer and constructively interferring with each other. The resulting dependence of the wave field in the top layer is expressed in terms of sines and cosines. For the two layer model, this is depicted by Figure 9. The apparent phase velocity in the x direction, c, and the wave velocity along a ray in the top layer, β_1, are related through $c = \beta_1/\sin\theta$, where θ is as defined in Figure 9. For θ greater than the critical angle,
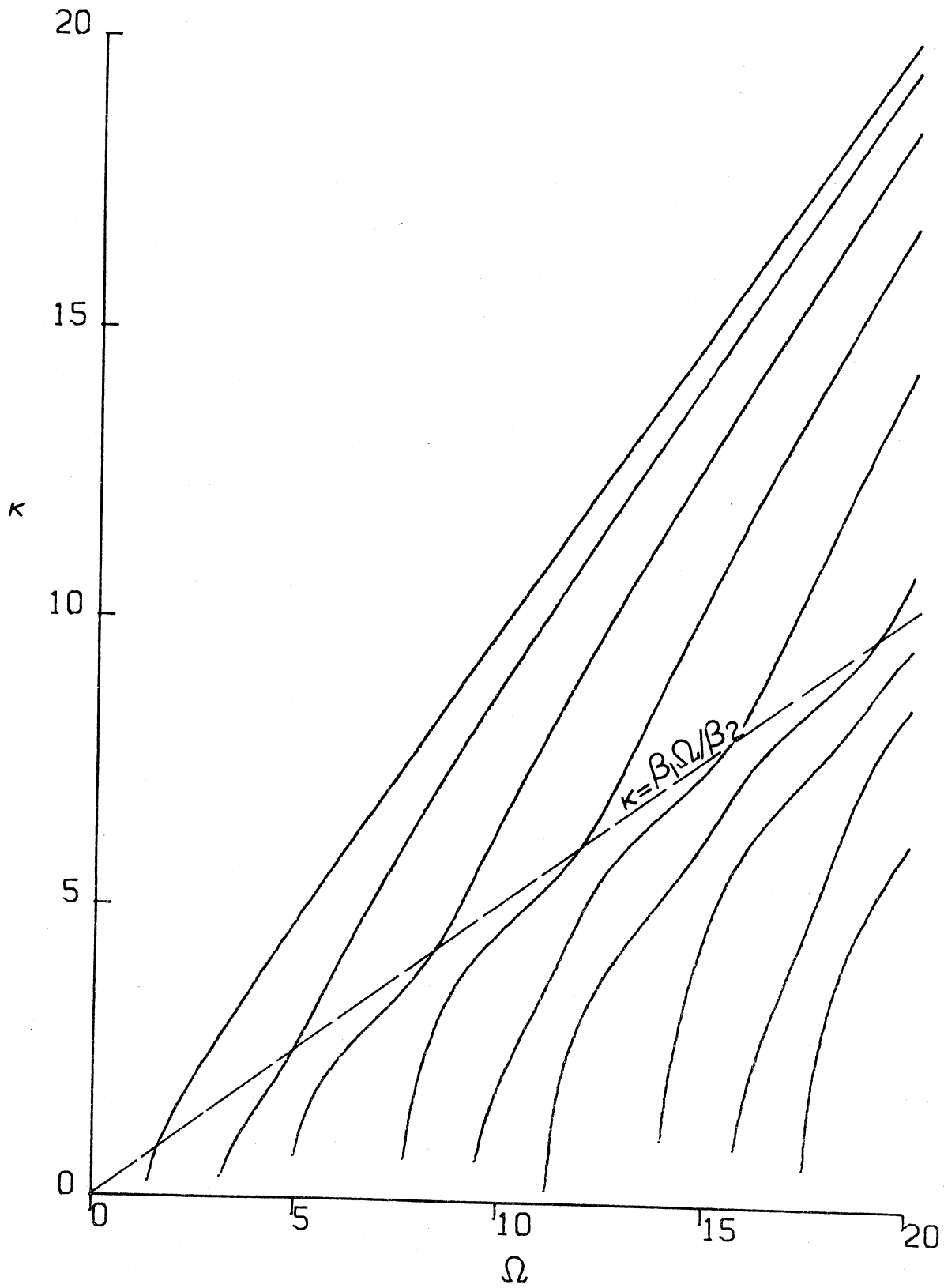
Figure 3. Progressing Waves -- Dispersion Curves for Two Layers
($\beta_1 = \rho_1 = h_1 = h_2 = 1$, $\beta_2 = \rho_2 = 2$)
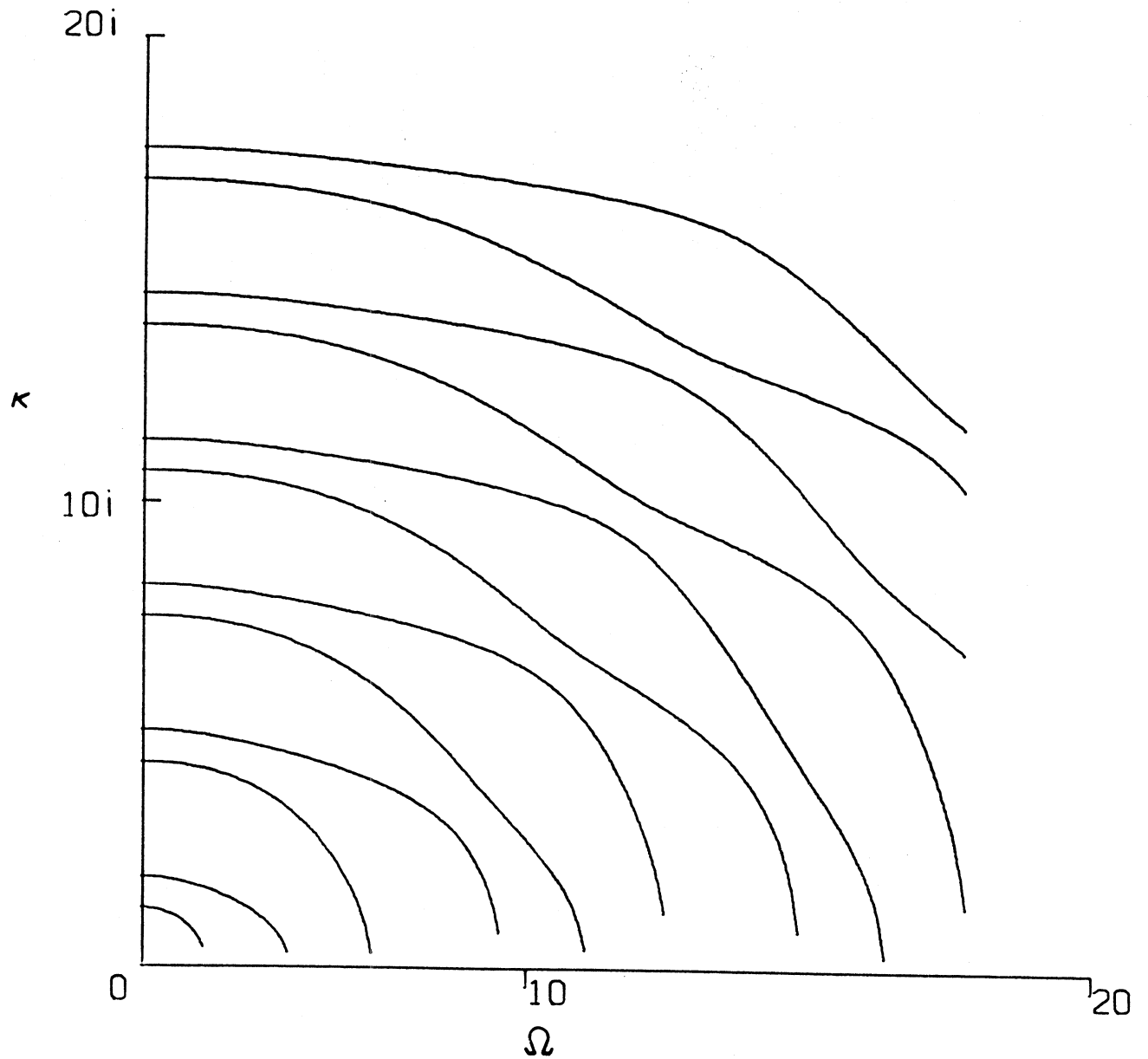
Figure 4. Locally Standing Waves -- Dispersion Curves for Three Layers ($\beta_1 = \rho_1 = h_1 = h_2 = h_3 = 1$, $\beta_2 = \rho_2 = 2$, $\beta_3 = \rho_3 = 3$)
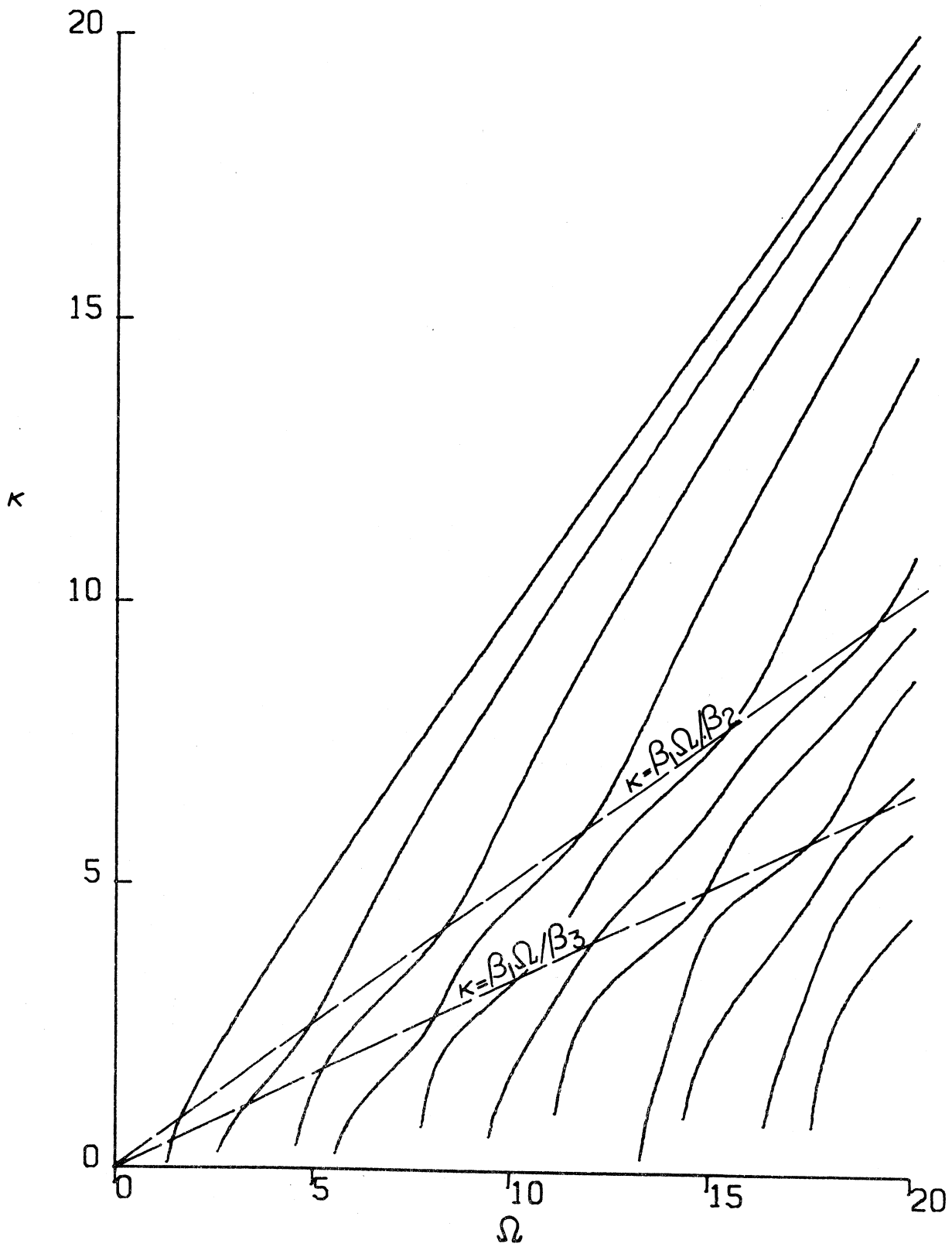
Figure 5. Progressing Waves -- Dispersion Curves for Three Layers
($\beta_1 = \rho_1 = h_1 = h_2 = h_3 = 1$, $\beta_2 = \rho_2 = 2$, $\beta_3 = \rho_3 = 3$)
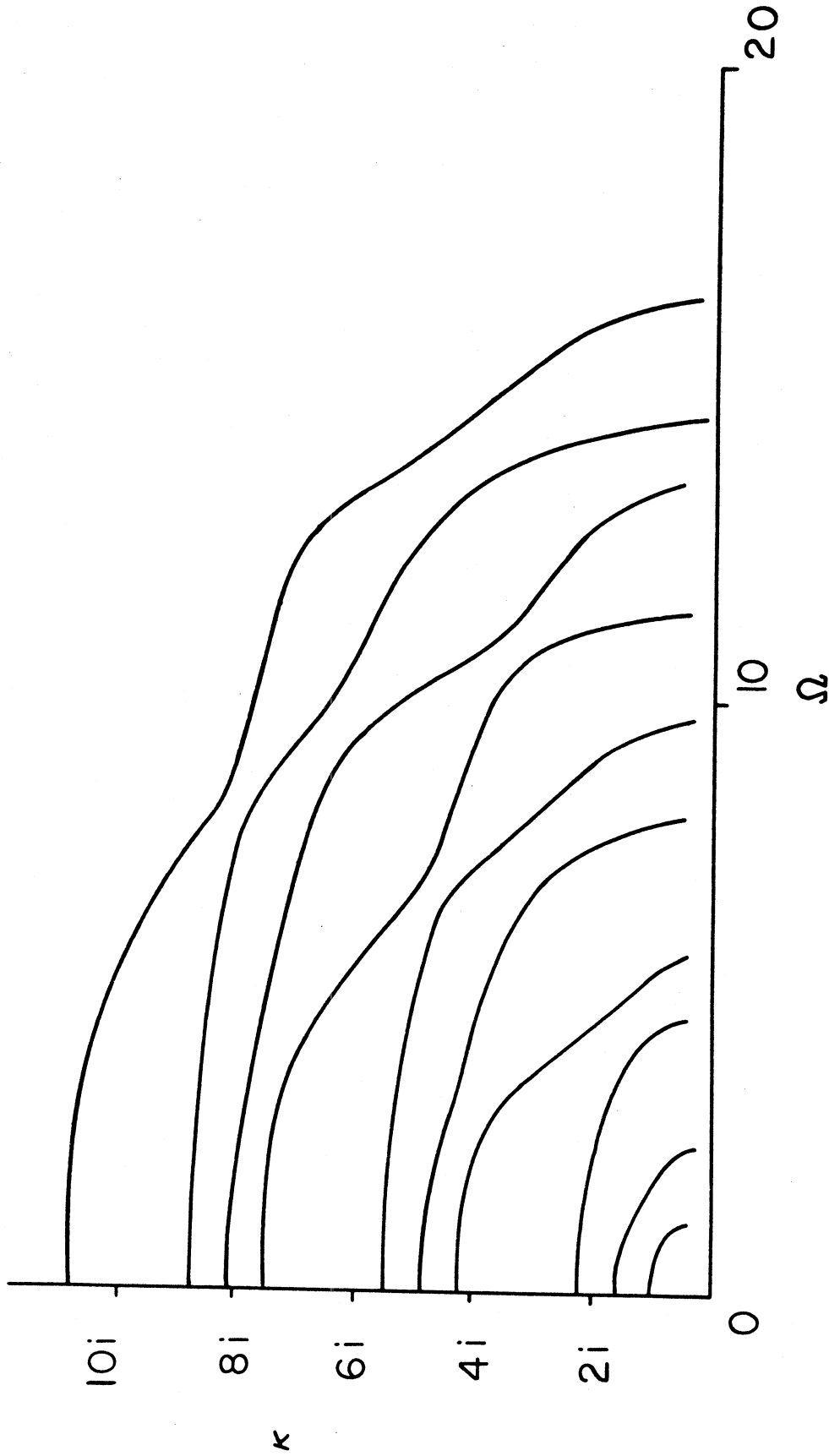
Figure 6.   Locally Standing Waves -- Dispersion Curves for Three Layers
($\beta_1 = \rho_1 = h_1 = h_2 = h_3 = h_4 = 1$, $\beta_2 = \rho_2 = 2$, $\beta_3 = \rho_3 = 3$, $\beta_4 = \rho_4 = 4$)
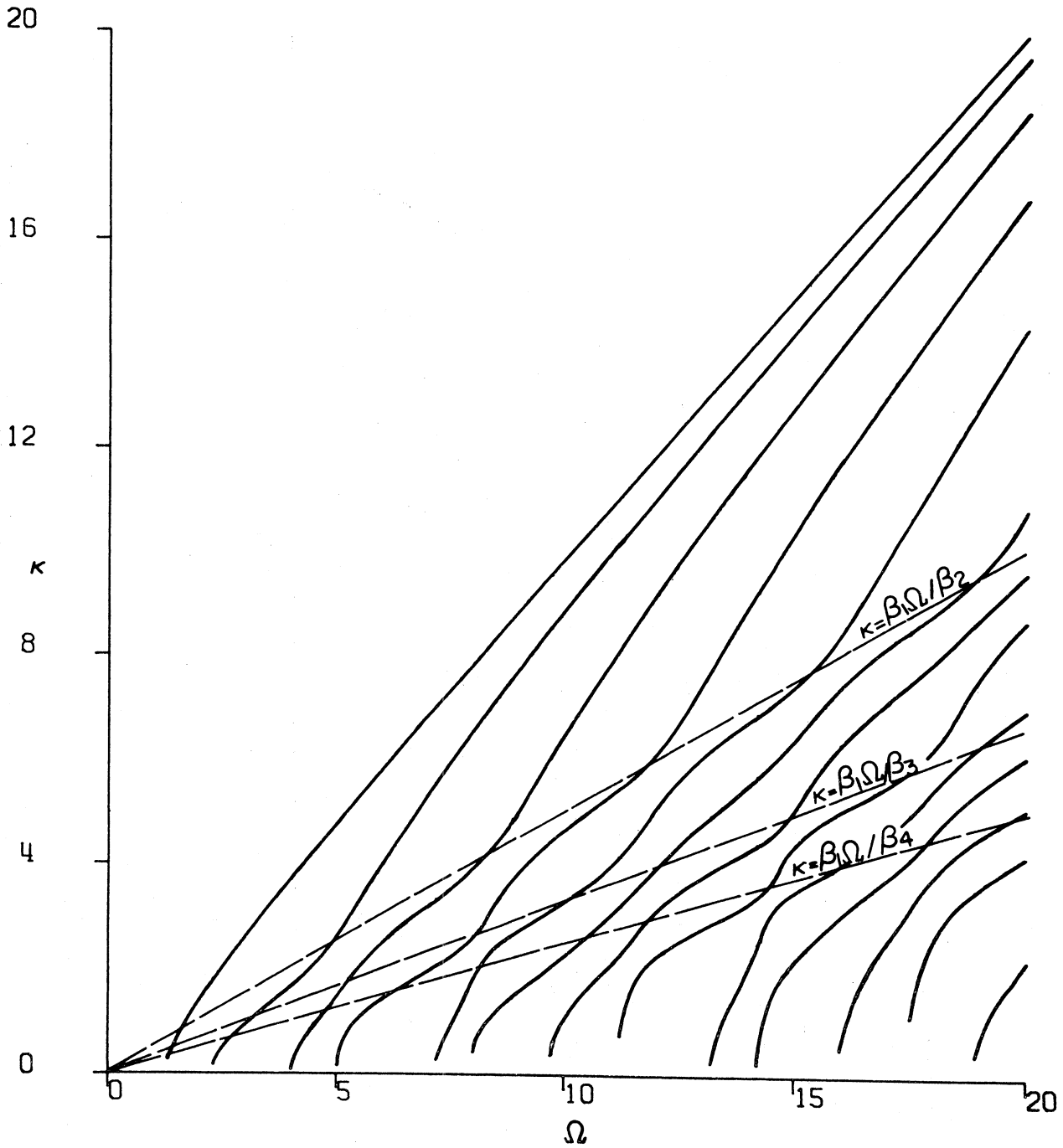
Figure 7. Progressing Waves -- Dispersion Curves for Four Layers
($\beta_1 = \rho_1 = h_1 = h_2 = h_3 = h_4 = 1$, $\beta_2 = \rho_2 = 2$, $\beta_3 = \rho_3 = 3$, $\beta_4 = \rho_4 = 4$)
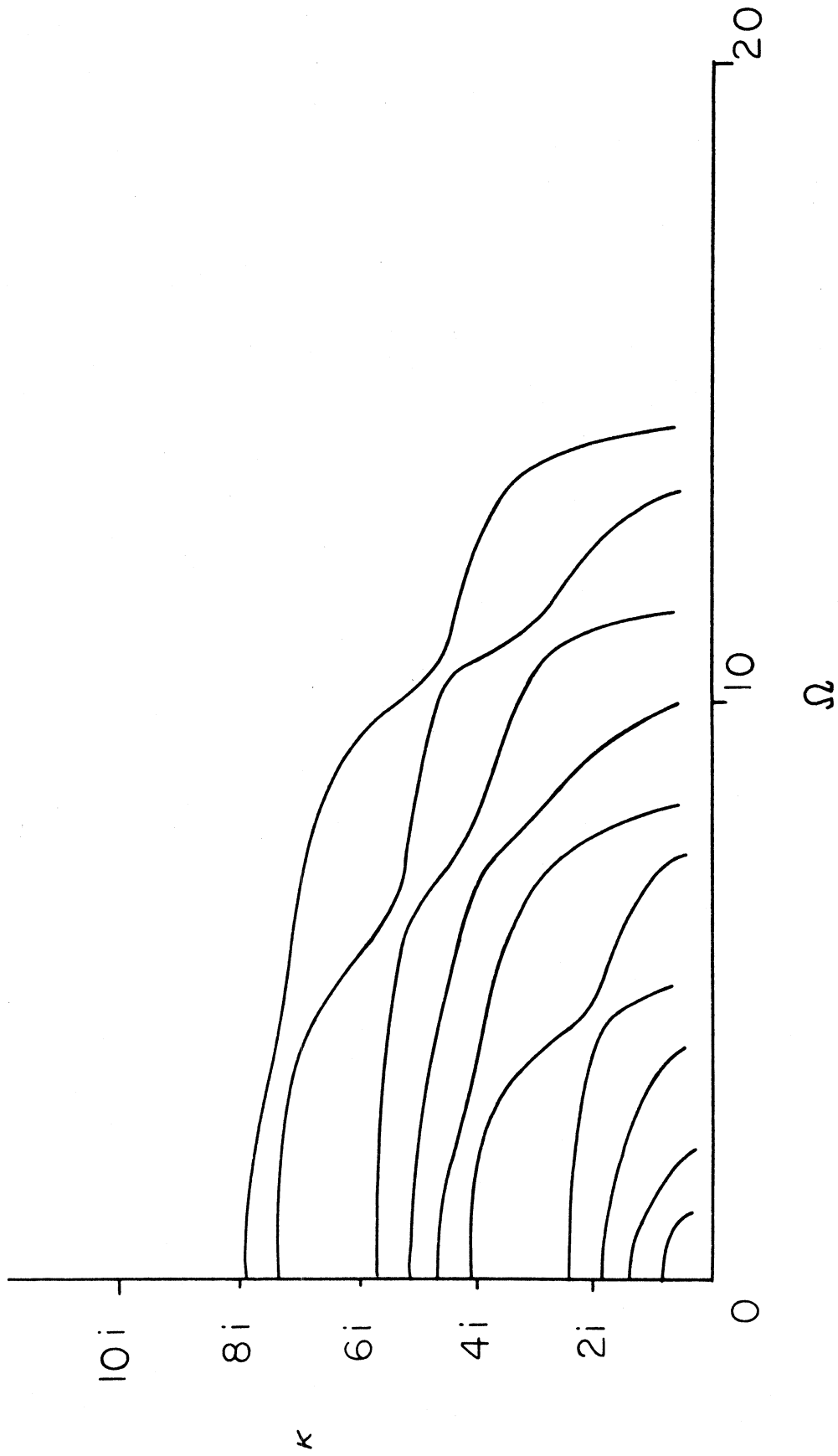
Figure 8. Locally Standing Waves -- Dispersion Curves for Four Layers
$(\beta_1 = \rho_1 = h_1 = h_2 = h_3 = h_4 = 1, \ \beta_2 = \rho_2 = 2, \ \beta_3 = \rho_3 = 3, \ \beta_4 = \rho_4 = 4)$
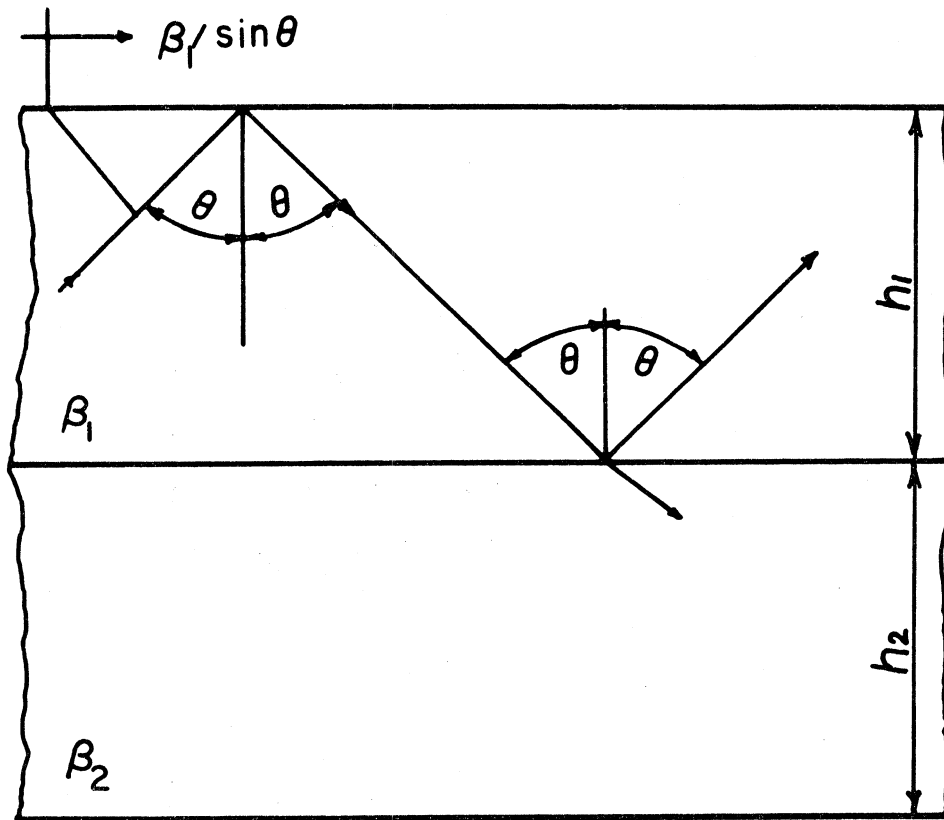
Figure 9. Two Layer Model -- Reflection and
Transmission of Waves from Top Layer

$\theta_{cr} = \sin^{-1}(\beta_1/\beta_2)$, the motion transmitted into the bottom layer is of the exponential character with increasing distance from the interface between the two layers (Achenbach, 1973). However, for subcritical angles $(\theta < \theta_{cr})$ the z dependence of the transmitted motion is of the same sinusoidal nature. The lines $\kappa = \Omega$ and $\kappa = \beta_1/\beta_2$ $(= \kappa_{cr} = \sin\theta_{cr} \cdot \Omega)$ separate the dispersion curves in the κ-Ω space into two physically different regions

1) $\dfrac{\beta_1}{\beta_2} \Omega < \kappa < \Omega$

2) $\kappa < \dfrac{\beta_1}{\beta_2} \Omega$, $\beta_1 < \beta_2$.

For the values κ and Ω in region 1 $(\beta_1/\beta_2 \Omega < \kappa < \Omega)$ waves transmitted from the top into the bottom layer depend exponentially upon the distance from the interface. For the pairs (κ, Ω) in region 2 $(\kappa < \beta_1/\beta_2 \Omega)$ the wave motion in the bottom layer is of the same character as one in the top layer. It is seen that as β_2 increases the region 2 decreases. For progressing waves in the three layer model (Figure 5) there are three regions

1) $\dfrac{\beta_1}{\beta_2} \Omega < \kappa < \Omega$

2) $\dfrac{\beta_1}{\beta_2} \Omega < \kappa < \beta_1/\beta_2 \Omega$

3) $\Omega < \kappa < \beta_1/\beta_3 \Omega$, $\beta_1 < \beta_2 < \beta_3$.

For (κ, Ω) in region 1, harmonic dependence of the wave motion with respect

to z is taking place in the top layer only. The middle and the bottom layer sustain the motions exponentially dependent upon the depth z. For (κ, Ω) in region 2, the exponentially dependent motion with depth z is present in the bottom layer only. Finally, for (κ, Ω) in the region 3, both bottom layers undergo the motions of sinusoidal character in z.

Similarly, for progressing waves in four layer model (Figure 7) the four regions are specified by

1) $\dfrac{\beta_1}{\beta_2} \Omega < \kappa < \Omega$

2) $\dfrac{\beta_1}{\beta_3} \Omega < \kappa < \beta_1/\beta_2 \ \Omega$

3) $\dfrac{\beta_1}{\beta_4} \Omega < \kappa < \beta_1/\beta_3 \ \Omega$

4) $\quad \Omega < \kappa < \beta_1/\beta_4 \ \Omega \quad , \quad \beta_1 < \beta_2 < \beta_3 < \beta_4 \quad .$

Comparison of Figures 3, 5 and 7 shows that the region $\beta_1/\beta_2 < \kappa < \Omega$ is common for all three models. Similarly, the region $\beta_1/\beta_3 < \kappa < \beta_1/\beta_2 \ \Omega$ in the three layer case (Figure 5) is preserved in the four layer model (Figure 7), etc.

Once the frequency equation has been solved, one can proceed with analysis of the eigenfunctions. This is the topic of the next section.

1.3.2 <u>Eigenfunctions</u>

The eigenfunctions are given by

$$v_j(x,z,\omega) = \phi_j(z)e^{ik_j x} \quad , \quad j=1,2, \ldots, \tag{1.29}$$

where $\phi_j(z)$, defined by (1.8) are called reduced eigenfunctions. Using the boundary conditions (1.3) it follows

$$b_1 = 0 \quad . \tag{1.30}$$

The continuity of stress and displacement fields (1.5) and (1.6) provides the following relations (superscript j being omitted)

$$a_2 = a_1 B_2 \qquad\qquad b_2 = a_1 D_2 \tag{1.31}$$

$$a_m = a_{m-1} B_m + b_{m-1} C_m$$

$$b_m = a_{m-1} D_m + b_{m-1} E_m \quad , \qquad m=3,4, \ldots, n \, , \tag{1.32}$$

where B_m, C_m, D_m and E_m are defined by

$$B_m = \cos q_{m-1} z_{m-1} \cdot \cos q_m z_{m-1} + \frac{\mu_{m-1} q_{m-1}}{\mu_m q_m} \sin q_{m-1} z_{m-1} \cdot \sin q_m z_{m-1}$$

$$C_m = \sin q_{m-1} z_{m-1} \cdot \cos q_m z_{m-1} - \frac{\mu_{m-1} q_{m-1}}{\mu_m q_m} \cos q_{m-1} z_{m-1} \cdot \sin q_m z_{m-1}$$

$$D_m = \cos q_{m-1} z_{m-1} \cdot \sin q_m z_{m-1} - \frac{\mu_{m-1} q_{m-1}}{\mu_m q_m} \sin q_{m-1} z_{m-1} \cdot \cos q_m z_{m-1}$$

$$E_m = \sin q_{m-1} z_{m-1} \cdot \sin q_m z_{m-1} + \frac{\mu_{m-1} q_{m-1}}{\mu_m q_m} \cos q_{m-1} z_{m-1} \cdot \cos q_m z_{m-1}$$

$$\tag{1.33}$$

The coefficients a_m and b_m, $m=2,3, \ldots, n$ can be expressed in terms of a_1, which is taken to be unity. Then, the eigenfunctions are

$$v_j(x,z,\omega) = \phi_j(z)e^{ik_j x} \quad , \qquad j=1,2,3, \ldots \, ,$$

where

$$\phi_j(z) = \begin{cases} a_2^j \cos q_2^j z \ , & 0 \leq z \leq z_1 \\ a_2^j \cos q_2^j z + b_2^j \sin q_2^j z \ , & z_1 \leq z \leq z_2 \\ \qquad\qquad \vdots \\ a_n^j \cos q_n^j z + b_n^j \sin q_n^j z \ , & z_{n-1} \leq z \leq z_n \end{cases}$$

$$a_2^j = B_2^j \qquad\qquad b_2^j = D_2^j$$

$$a_m^j = B_2^j B_3^j \ \cdots \ B_m^j + D_2^j C_3^j C_4^j \ \cdots \ C_m^j$$

$$b_m^j = B_2^j D_3^j \ \cdots \ D_m^j + D_2^j E_3^j E_4^j \ \cdots \ E_m^j$$

$$m = 3, 4, \ldots, n \ . \qquad\qquad (1.34)$$

The coefficients B_m^j, C_m^j, D_m^j and E_m^j are given by (1.33).

1.3.2.1. Orthogonality of Eigenfunctions

In testing for orthogonality of eigenfunctions, a procedure suggested by Alsop (1966) is followed.

Substituting eigenfunction (1.34) into equation (1.2), the following wave equation is derived

$$\frac{d^2 \phi_j}{dz^2} + \left(\frac{\omega^2}{\beta^2} - k_j^2 \right) \phi_j = 0 \ , \qquad j = 1, 2, \ldots \ . \qquad (1.35)$$

Then one can write that

$$\frac{d}{dz} \left(\phi_j \frac{d\phi_i}{dz} - \phi_i \frac{d\phi_j}{dz} \right) = \left(k_i^2 - k_j^2 \right) \phi_i \phi_j \ , \ i \neq j \ . \qquad (1.36)$$

Before proceeding with integration of the last equation, it is necessary to show that the term $(\phi_j \, d\phi_i/dz - \phi_i \, d\phi_j/dz)$ is continuous. Along the interfaces $z = z_m$, $m = 1, 2, \ldots, n-1$, due to the continuity of the displacement and stress fields (1.5) and (1.6) it follows that

$$\phi_j(z_m^-)\frac{d\phi_i(z_m^-)}{dz} - \phi_i(z_m^-)\frac{d\phi_j(z_m^-)}{dz} = \frac{\mu_{m+1}}{\mu_m}\left[\phi_j(z_m^+)\frac{d\phi_i(z_m^+)}{dz}\right.$$

$$\left. - \phi_i(z_m^+)\frac{d\phi_j(z_m^+)}{dz}\right] \quad . \tag{1.37}$$

The last result suggests introduction of a weighting function μ. Then (1.36) becomes

$$\frac{d}{dz}\left[\mu\left(\phi_j\frac{d\phi_i}{dz} - \phi_i\frac{d\phi_j}{dz}\right)\right] = \left(k_i^2 - k_j^2\right)\mu\phi_i\phi_j \quad . \tag{1.38}$$

In view of (1.37), the left hand side of the last equation is continuous across each interface. Integrating (1.38) there results the orthogonality relation

$$\int_0^{2n} \mu(z)\phi_i(z)\phi_j(z)dz = 0 \quad , \quad i \neq j \quad , \tag{1.39}$$

where $\mu(z)$ is assumed to be constant within each layer.

Since k_i are either real or pure imaginary non-zero constants, $(k_i^2 - k_j^2) \neq 0$ for $i \neq j$ and (1.39) holds for all members of $\phi_i(z)$ family even when members corresponding to real and pure imaginary k_i's are considered.

1.3.2.2 Expansion in Terms of Eigenfunctions

In this section, the expansion of an input function $g(z)$ (section 1.1) in terms of the reduced eigenfunctions $\phi_j(z)$ is considered. For a single layer problem, the reduced eigenfunctions are given by

$$\phi_j(z) = \cos\frac{(2j-1)\pi}{2h_1}z \quad ; \qquad 0 \leq z \leq z_1 \quad , j=1,2, \ldots \quad . \tag{1.40}$$

Without loss of generality the input function (1.1) can be chosen to

satisfy

$$\frac{dg(0)}{dz} = 0 \quad \text{and} \quad g(z_1) = 0 \quad . \tag{1.41}$$

To expand $g(z)$ in terms of $\phi_j(z)$ the input function $g(z)$ is extended as an even function with period $4z_1$ as shown in Figure 10a. Similarly, for the case of n layers, $g(z)$ can be extended as an even function with period $4z_n$.

Using the orthogonality relation (1.39) the input function $g(z)$ can be expanded in terms of reduced eigenfunctions

$$g(z) = \sum_{j=1}^{\infty} \alpha_j \phi_j(z) \quad , \tag{1.42}$$

where

$$\alpha_j = \frac{(\phi_j, g)}{(\phi_j, \phi_j)} \quad \text{and} \tag{1.43}$$

$$(\phi_j, g) \equiv \int_{-2z_n}^{2z_n} \mu(z)\phi_j(z)g(z)dz \quad ; \quad (\phi_j, \phi_j) \equiv \int_{-2z_n}^{2z_n} \mu(z)\phi_j^2(z)dz \quad . \tag{1.44}$$

Therefore, the input displacement field (1.1) can be written as

$$v^i = v(0,z,\omega) = F(\omega) \sum_j \alpha_j \phi_j(z) \quad . \tag{1.45}$$

At a given frequency ω, only a finite number of progressive modes (eigenfunctions corresponding to real k_j's) and infinitely many locally standing modes (eigenfunctions which correspond to pure imaginary k_j's) are present. Therefore, (1.45) represents expression of the input field v^i in terms of all modes which exist at the particular frequency ω.
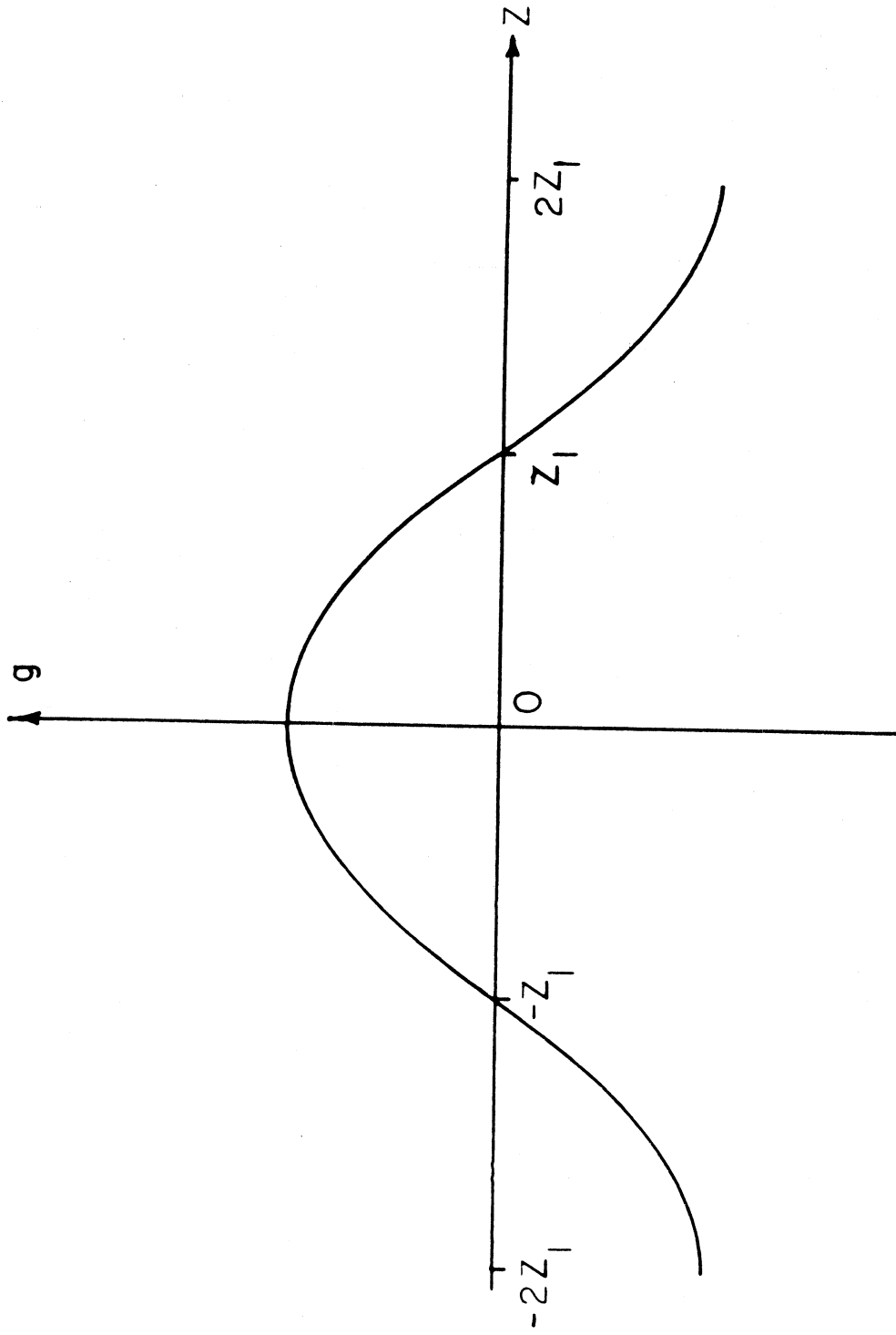
Figure 10a. Extension of Input Function for
Single Layer Model

The displacement field $v(x,z,\omega)$ can be expressed in terms of the eigenfunctions as

$$v(x,z,\omega) = F(\omega) \sum_j \alpha_j \phi_j(z) e^{ik_j x} \quad . \tag{1.46}$$

with α_j specified by (1.43). Therefore, at fixed x and z, the displacement field in layered media can be represented in the following form

$$v(x,z,\omega) = D(\omega) e^{i\theta(\omega)} \quad . \tag{1.47}$$

The frequency spectra $D(\omega)$ and the phase shift $\theta(\omega)$ are defined by

$$|D(\omega)| \equiv \sqrt{(Re\{v\}^2 + Im\{v\}^2} \tag{1.49}$$

and

$$\theta = \tan^{-1} \frac{Im\{v\}}{Re\{v\}} \quad .$$

In the above expression $Re\{\cdot\}$ and $Im\{\cdot\}$ denote real and imaginary parts of $\{\cdot\}$ respectively.

1.3.3 Energy Density

The frequency response $v(x,z,\omega)$ at any station (x,z) has been specified by (1.47). Therefore, for delta function temporal input (i.e., $F(\omega) = 1$), the displacement field $v(x,z,\omega)$ is given by

$$v(x,z,\omega) = \sum_j \alpha_j \phi_j(z) e^{ik_j x} \quad . \tag{1.51}$$

The velocity field for the jth mode (progressive or locally standing) can be written as

$$\dot{v}_j(x,z,\omega) = -i\omega\alpha_j \phi_j(z) e^{ik_j x} \quad . \tag{1.52}$$

Taking into account only the geometry of the model and input field, a

measure of energy density for the jth mode at station (x,z) and at frequency ω can be defined in the following manner

$$e_j(x,z,\omega) = \frac{1}{2} \rho(z)|\alpha_j\phi_j(z)e^{ik_jx}|^2 \quad , \quad j=1,2,3, \ldots \quad , \tag{1.53}$$

with ρ being the density of elastic material. At each frequency ω the total energy density is a sum of energy densities of all modes present at that frequency, or

$$e(x,z,\omega) = \sum_j e_j(x,z,\omega) \quad , \tag{1.54}$$

where e_j has been defined by (1.53).

It is evident from (1.53) that energy density for a propagating mode is independent of x, while for locally standing modes, the energy density exponentially decays with increasing x (distance from the source).

One of the aims of this investigation is to determine the ratio of the energy density of progressive waves versus energy density of locally standing waves at stations $(x,z=0)$ for different values of x. This is done to establish how far from the source (input) the energy density of standing waves is significant compared to the energy density of progressive waves.

1.3.4 Rotation

Torsional and rocking excitation of structures are specified by rotational field of strong ground motion. For problems under investigation, the rotational field is determined by application of the curl operator to the displacement field, i.e.,

$$\underset{\sim}{r}(x,z,\omega) = \nabla\times \begin{bmatrix} 0 \\ v(x,z,\omega) \\ 0 \end{bmatrix} \quad , \tag{1.55}$$

the displacement field $v(x,z,\omega)$ is given by (1.47). It follows then from (1.55) that

$$\underset{\sim}{r}(x,z,\omega) = \begin{bmatrix} -\dfrac{\partial v}{\partial z} \\[2mm] 0 \\[2mm] \dfrac{\partial v}{\partial x} \end{bmatrix} \quad , \tag{1.56}$$

For antiplane strain model, we seek the z-component of rotation vector r_z which represents the torsional excitation for structure near a fault.

Introduction of (1.47) into (1.56) yields

$$r_z(x,z,\omega) = iF(\omega) \sum_j k_j \alpha_j \phi_j(z) e^{ik_j x} \quad , \tag{1.57}$$

with factor $\exp(-i\omega t)$ being omitted. The corresponding amplitude spectrum is then

$$R(x,z,\omega) = \sqrt{Re^2\{r_z\} + Im^2\{r_z\}} \quad , \tag{1.58}$$

where Re and Im stand for real and imaginary parts of { }, respectively.

2. Evaluation of Results

2.1 Input Functions

The steady state displacement input (1.1) is described by two functions: its temporal part is specified by $f(t)$ and spatial part by $g(z)$. For the purpose of this analysis, the temporal function is assumed to be given by superposition of a ramp function and a ripple of finite duration, i.e.,

$$f(t) = f_1(t) + f_2(t) \quad , \qquad -\infty < t < \infty \quad , \tag{2.1}$$

where

$$f_1(t) = \begin{cases} 0 & , & t < 0 \\[2mm] \dfrac{a}{t_0}\, t & , & 0 \le t \le t_0 \\[2mm] a & , & t > t_0 \end{cases} \tag{2.2}$$

$$f_2(t) = \begin{cases} \zeta a \, \sin \dfrac{2\pi}{t_0}\, t & , & 0 \le t \le t_0 \\[4mm] 0 & , & t < 0 \ \text{ and } \ t > t_0 \end{cases} \tag{2.3}$$

The parameters ζ, a and t_0 can be specified in each problem. Examples of the functions $f_1(t)$ and $f_2(t)$ are shown in Figure 10b.

Function $F(\omega)$ in (1.1) represents the Fourier transform of $f(t)$

$$F(\omega) = \int_{-\infty}^{\infty} f(t) e^{i\omega t}\, dt \quad . \tag{2.4}$$

By applying the Fourier transform to (2.2) and (2.3), it follows

$$F(\omega) = F_1(\omega) + F_2(\omega) \quad , \tag{2.5}$$
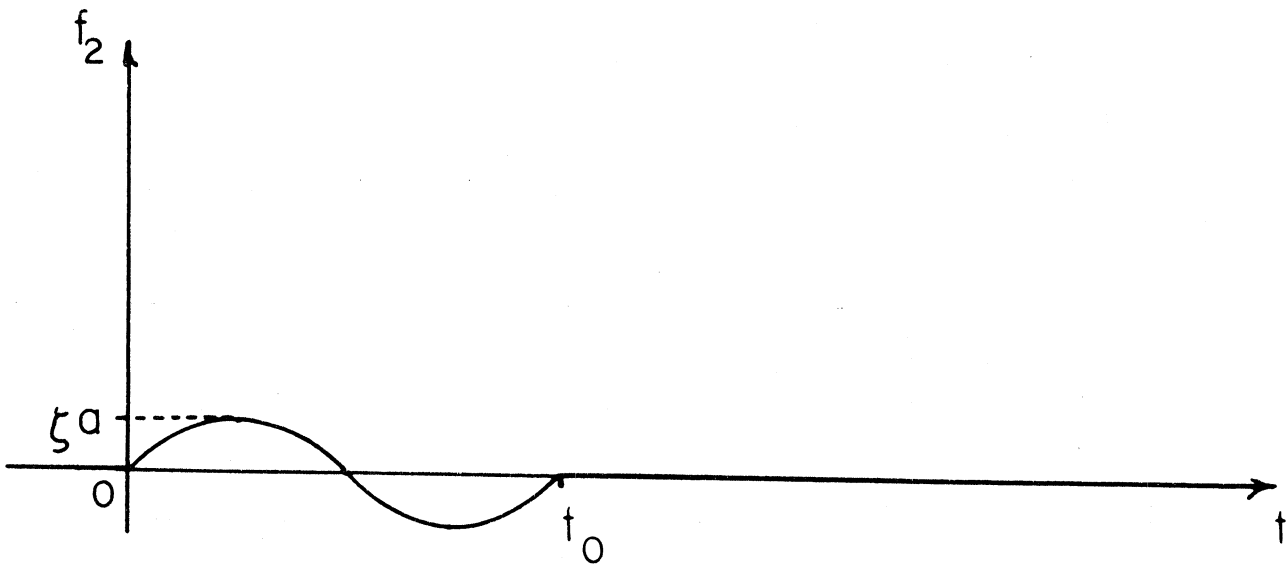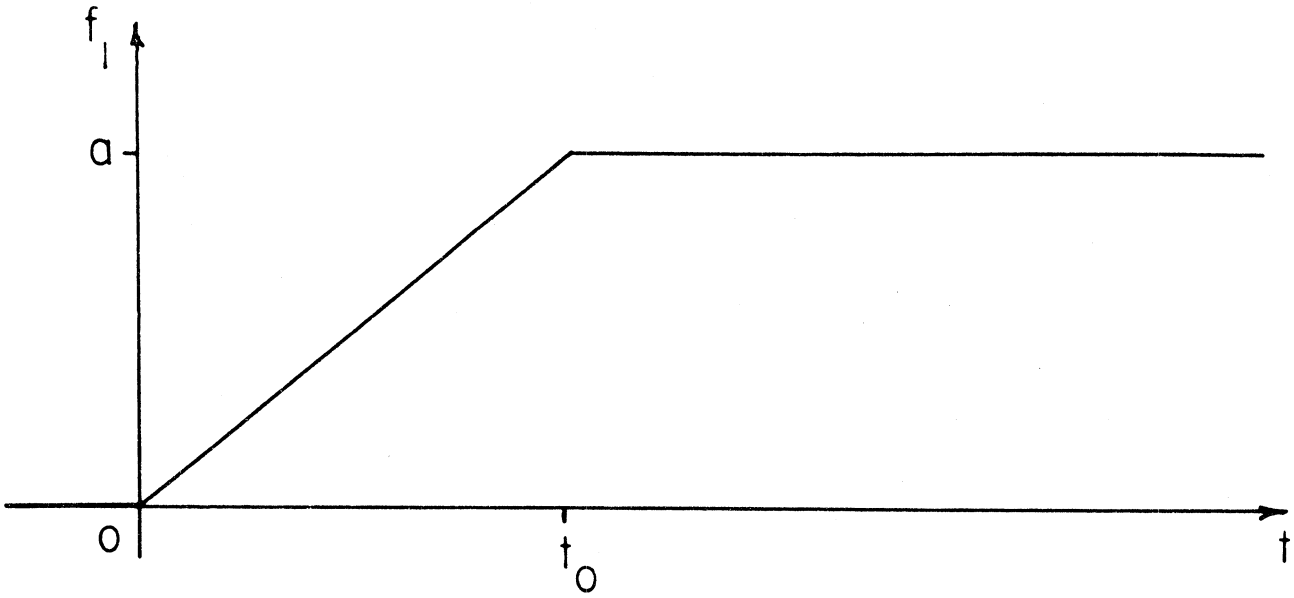
Figure 10b. Input Functions

where the principal part of $F_1(\omega)$ is

$$F_1(\omega) = \frac{a}{t_o} \frac{e^{i\omega t_o} - 1}{\omega^2} \qquad (2.6)$$

and

$$F_2(\omega) = \zeta a \frac{2\pi}{t_o} \frac{e^{i\omega t_o} - 1}{\omega^2 - \left(\frac{2\pi}{t_o}\right)^2} \qquad (2.7)$$

The spatial function $g(z)$ is chosen to be of the following form

$$g(z) = \begin{cases} v_o & , \quad \xi z_m \le z \le \eta z_n \, , \quad m < n \\ 0 & , \quad \text{otherwise} \, , \end{cases} \qquad (2.8)$$

with v_o being arbitrary amplitude and $0 < \xi, \eta < 1$.

Physically, (2.8) implies that the plane x=0 of the quarter space layered medium is subjected to a constant displacement v_o uniformly along the y-axis in a vertical region between ξz_m and ηz_n and acts according to time function specified by (2.1).

In the present work, the shear wave velocity, density and the thickness of the top layer are assumed to be of unit magnitude, i.e., $\beta_1 = 1\text{m/s}$, $\rho = 1\text{kg/m}^3$, and $h_1 = 1\text{m}$. Furthermore, the parameters of the input field (2.1 - 2.8) are assumed to be a = 1m, t_o = 1s, ζ = 0.2, v_o = 1m. Consequently, all the results are presented in dimensionless form. Indeed, all spatial variables are normalized with respect to h_1 = 1m, all temporal variables are normalized with respect to t_o = 1s, all velocities are normalized with respect to the velocity of the shear wave in the top layer β_1 = 1m/s, etc. (To simplify the notation, the physical quantities are denoted by the same symbol after being normalized, since the normalizing factor is always of unit magnitude. For example, by the displacement field $v(x,z,\omega)$ it is understood

$v(x,z,\omega)/h_1 = v(x,z,\omega)/1$, etc. The only exception to this rule will be dimensionless frequency Ω and the wave number κ which are frequently written explicitly as $\Omega = \omega h_1/\beta_1$, and $\kappa = k h_1$.)

2.2 Dispersion and Distribution of Shear-Wave Velocity

In the analysis of the layered model (Figure 1), its dispersion properties are examined first by considering the influence of shear wave velocity distribution upon dispersion of progressive waves. In particular, for the two-layer model, the dispersion curves for different velocity distributions are evaluated. Assuming the properties of the top layer (without loss of generality, the shear wave velocity, shear modulus, and thickness for all calculations are equal to 1), the shear wave velocity and density of the bottom layer are varied. The results of four examples are shown in Figures 11 through 14. Since for a single layer progressing modes are represented by hyperbolae (Figure 2), one can view progressing modes in the two-layer model as distorted hyperbolae in the Ω-κ space. For example, by increasing the acoustic stiffness of the second layer such that $\beta_2 = 4\beta_1$, Figure 11 shows that the first two modes essentially reduce to those of the single layer model in Figure 2. Further increasing the shear wave velocity of the bottom layer to $\beta_2 = 6\beta_1$ (Figure 12) makes the first three modes resemble those in a single layer (Figure 2). The fourth mode is the first to "detect" the presence of the second layer. In Figures 13 and 14, the dispersion curves are shown for β_2 being $8\beta_1$ and $10\beta_1$, respectively. For $\beta_2 = 10\beta_1$, the dispersion curves for two layers reduce almost to the dispersion curves of a single layer model in Figure 2. Thus, for the
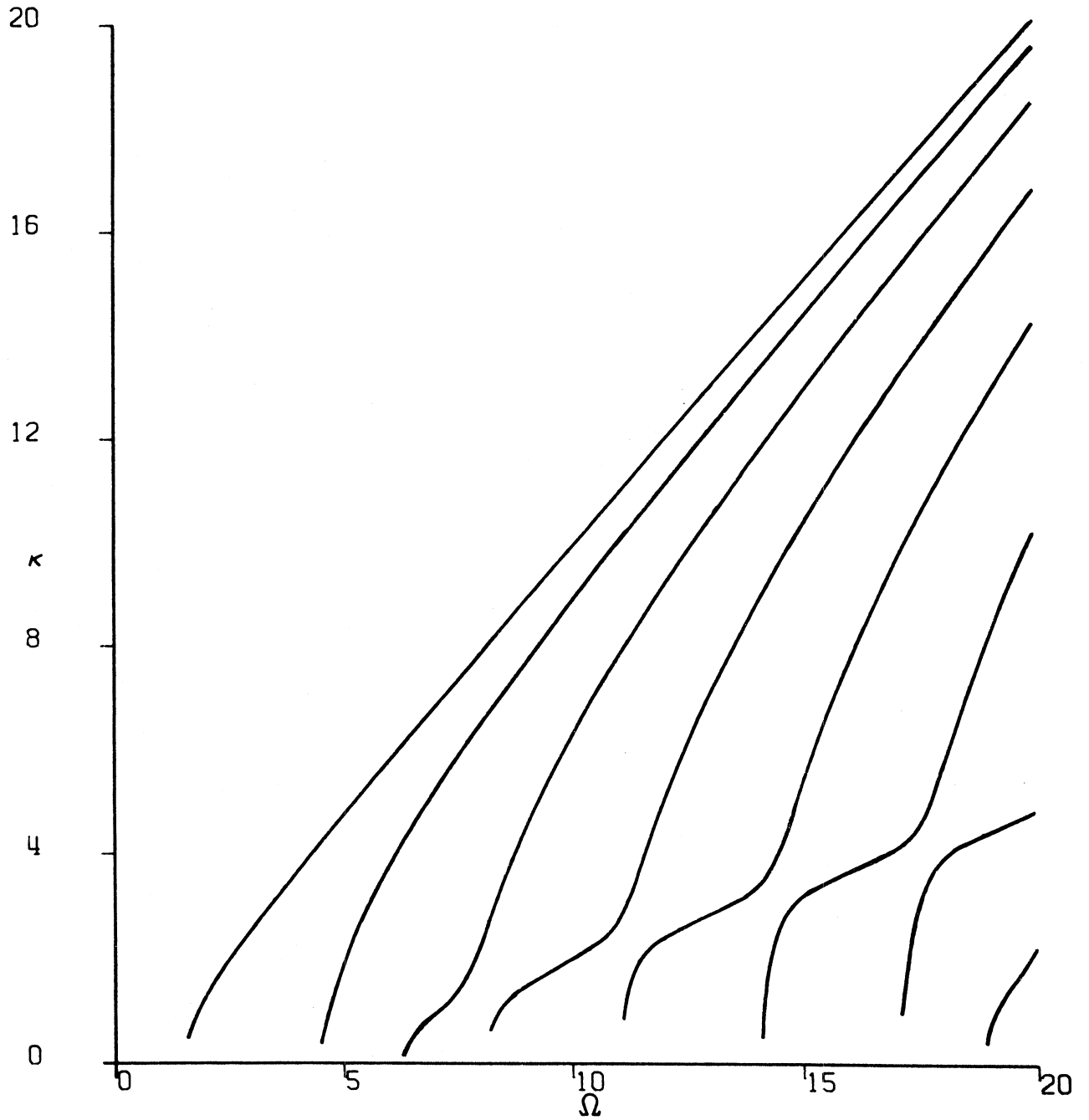
Figure 11. Dispersion Curves for Progressing Waves in Two Layers ($\beta_1 = \rho_1 = h_1 = h_2 = 1$, $\beta_2 = 4$, $\rho_2 = 2$)
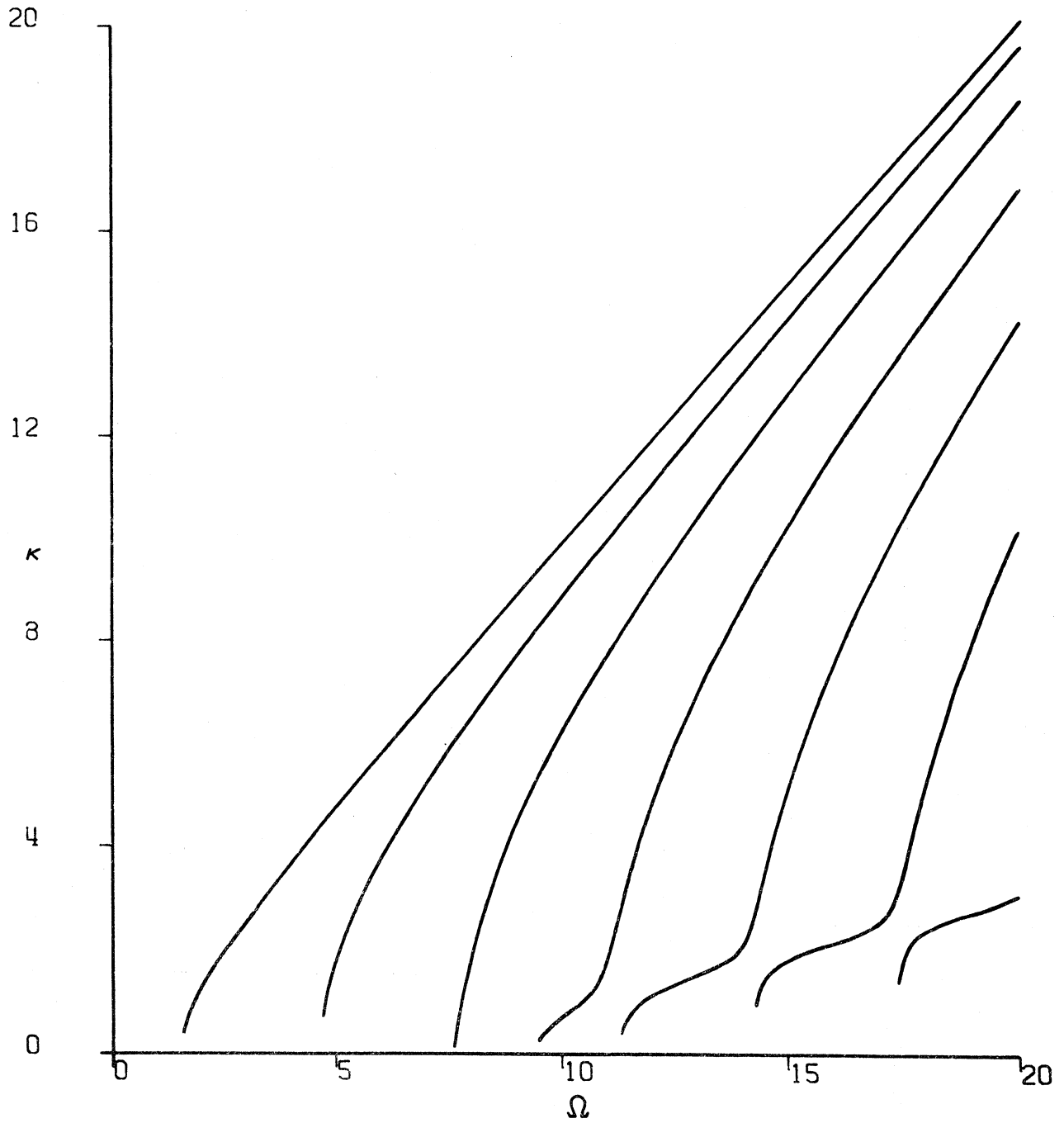
Figure 12. Progressing Waves -- Dispersion Curves for Two Layers ($\beta_1 = \rho_1 = h_1 = h_2 = 1$, $\beta_2 = 6$, $\rho_2 = 2$)
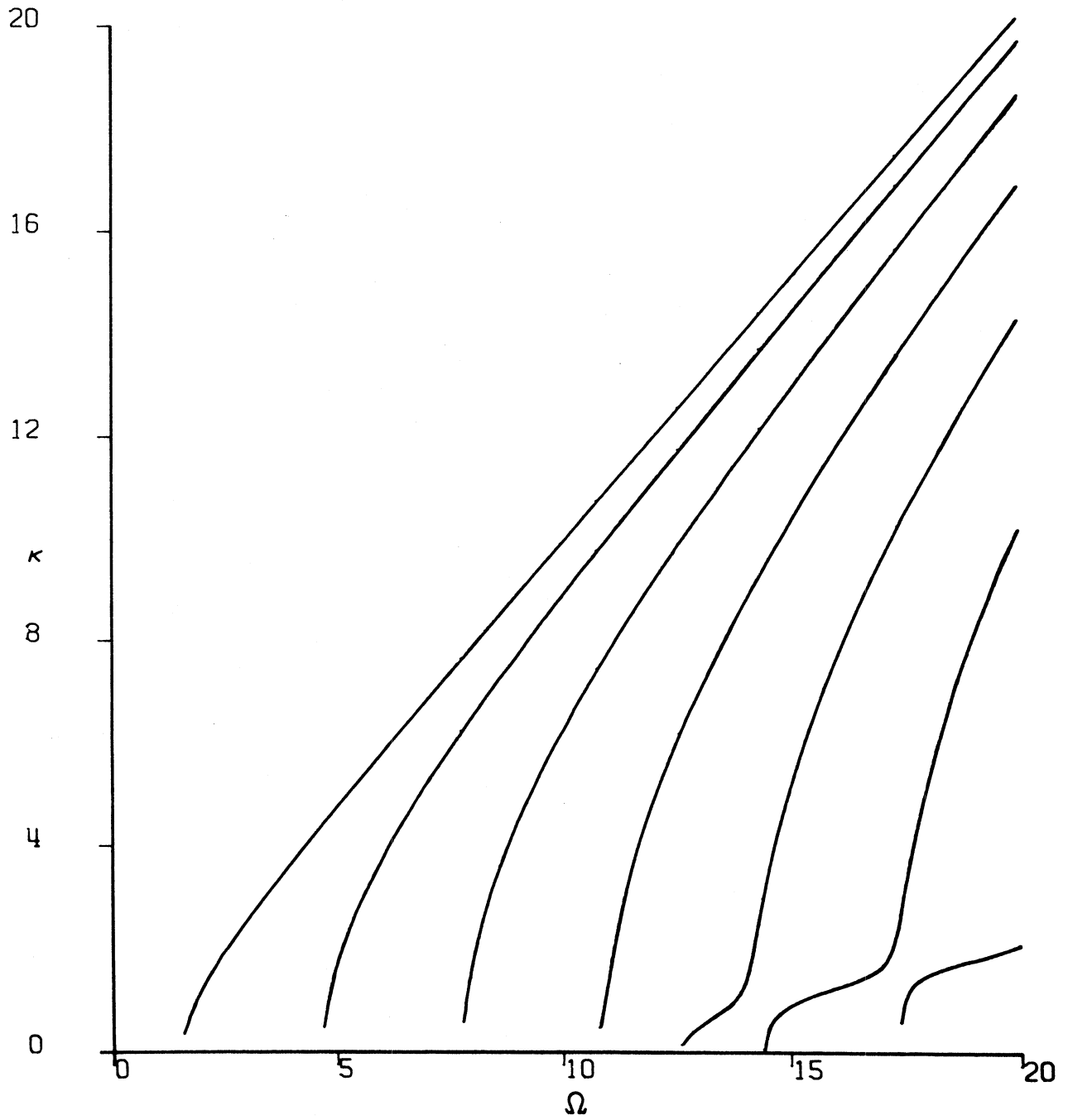
Figure 13.   Progressing Waves -- Dispersion Curves for Two
Layers ($\beta_1 = \rho_1 = h_1 = h_2 = 1$, $\beta_2 = 8$, $\rho_2 = 2$)
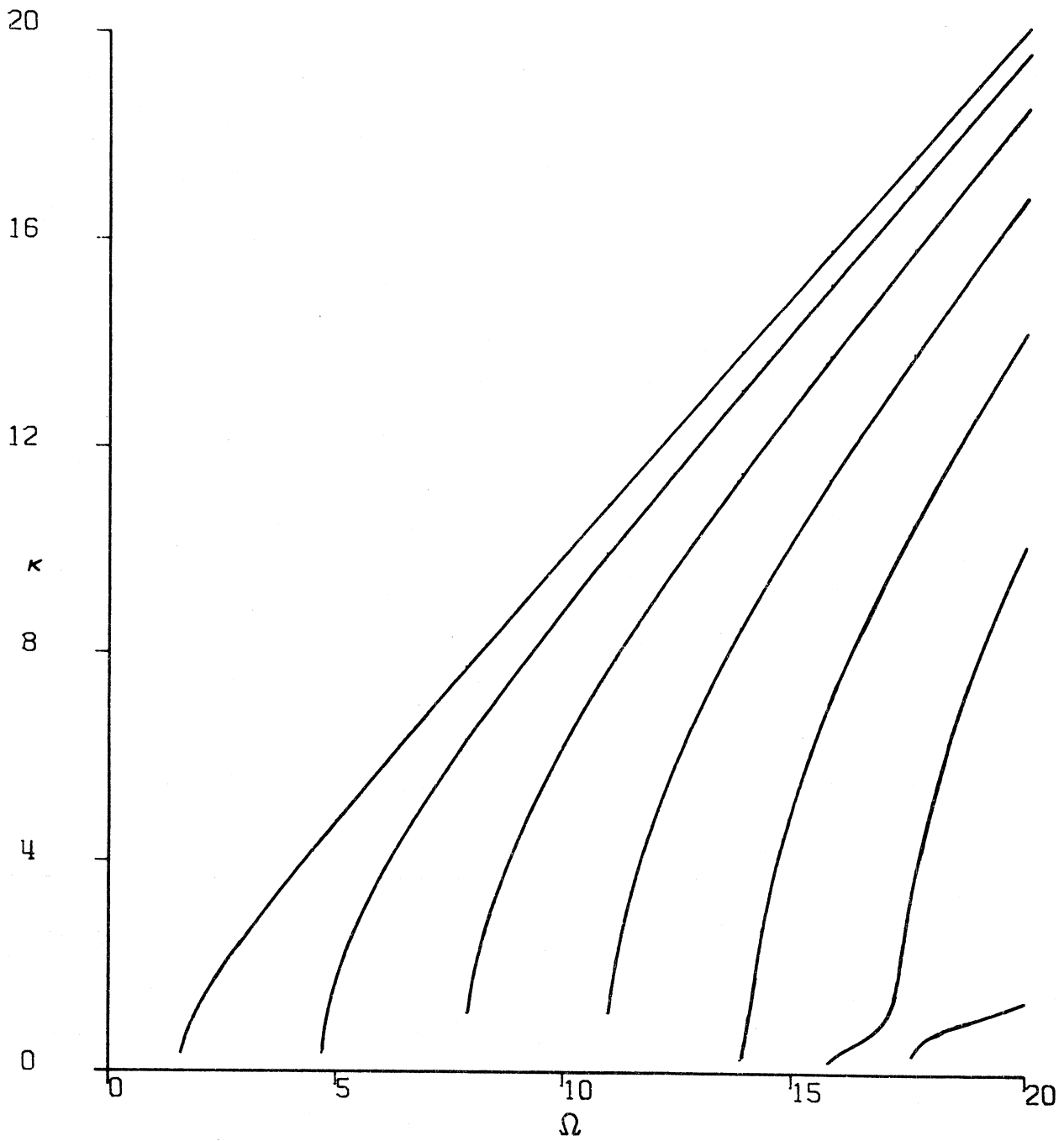
Figure 14. Progressing Waves -- Dispersion Curves for Two
Layers ($\beta_1 = \rho_1 = h_1 = h_2 = 1$, $\beta_2 = 10$, $\rho_2 = 2$)

shear wave velocity in the bottom layer being one order of magnitude greater than the shear wave velocity in the top layer, the lowest dispersion modes reduce the the ones established in a single layer model (Figure 2). In view of the discussion in Section 1.3.3, the results of dispersion curves presented in Figures 11 through 14 clearly indicate that as the acoustic stiffness of the bottom layer increases, the motion transmitted into this layer becomes predominantly of the type which depends exponentially upon increasing depth. The line of "critical wave number" is given by $\kappa_{cr} = \beta_1/\beta_2 \, \Omega$. For all (κ, Ω) above this line the motion in the bottom layer is of exponential character in z. For (κ, Ω) below the κ_{cr}=line, the motion in the bottom layer is of the same type as the motion in the top layer which consists of plane waves with sinusoidal dependence upon the depth z (Figure 9). The slope of the critical line κ_{cr} is inversely proportional to the velocity of the shear waves in the bottom layer β_2 (β_1 is assumed a pirori to be equal to unity). Thus, for $\beta_2 = 10\beta_1$, Figure 14 illustrates that the motion in the bottom layer is predominantly exponential. For perfectly rigid bottom layer ($\beta_2 \to \infty$) the "critical line" becomes $\kappa_{cr} = 0$ and the dispersion curves reduce to one in the case of a single layer upon a rigid half-space. This indicates that the assumption of a rigid half-space for $z > z_n$ is acceptable if the acoustic stiffness of layers for $z > z_n$ is much greater compared to the stiffness of the top layers $(z < z_n)$.

2.3 Displacement Frequency Spectra

2.3.1 Progressing Waves

We begin by considering the single layer model. The corresponding frequency equation has been discussed in Section 1.3.1 and the reduced eigenfunctions are given by (1.40). Using (1.43) and (1.44), the expansion coefficients α_j are calculated as

$$\alpha_j = \frac{\mu_1}{h_1} \int_0^{2h_1} g(z) \cdot \cos \frac{(2j-1)\pi z}{2h_1} \, dz \, , \quad j=1,2, \ldots, N \, . \tag{2.9}$$

The frequency response (1.47) is then

$$v(x,z,\omega) = F(\omega) \sum_{j=1}^{N} \alpha_j \cos \frac{(2j-1)\pi z}{2h_1} e^{ik_j x} \, , \tag{2.10}$$

with $e^{-i\omega t}$ being omitted. For input functions $F(\omega)$ and $g(z)$ defined by (2.5) and (2.8), the Fourier amplitude spectrum of progressive waves $D(\Omega)$ is shown in Figure 15. The numbers along the spectral amplitudes in Figure 15 denote the frequencies where the corresponding progressive modes begin to contribute. For example, 4 denotes the frequency point where the fourth progressive mode begins to propagate. From the frequency on the spectrum is represented by the first four progressive modes. After point 5, the first five progressive modes contribute to the frequency spectrum and so on.

For the range of dimensionless frequencies considered in Figure 15 the first six modes of progressive waves are present in the system. To illustrate the amplitude contribution of each mode to the overall amplitudes, the higher modes are omitted in succession. This is shown in Figures 16 through 20.
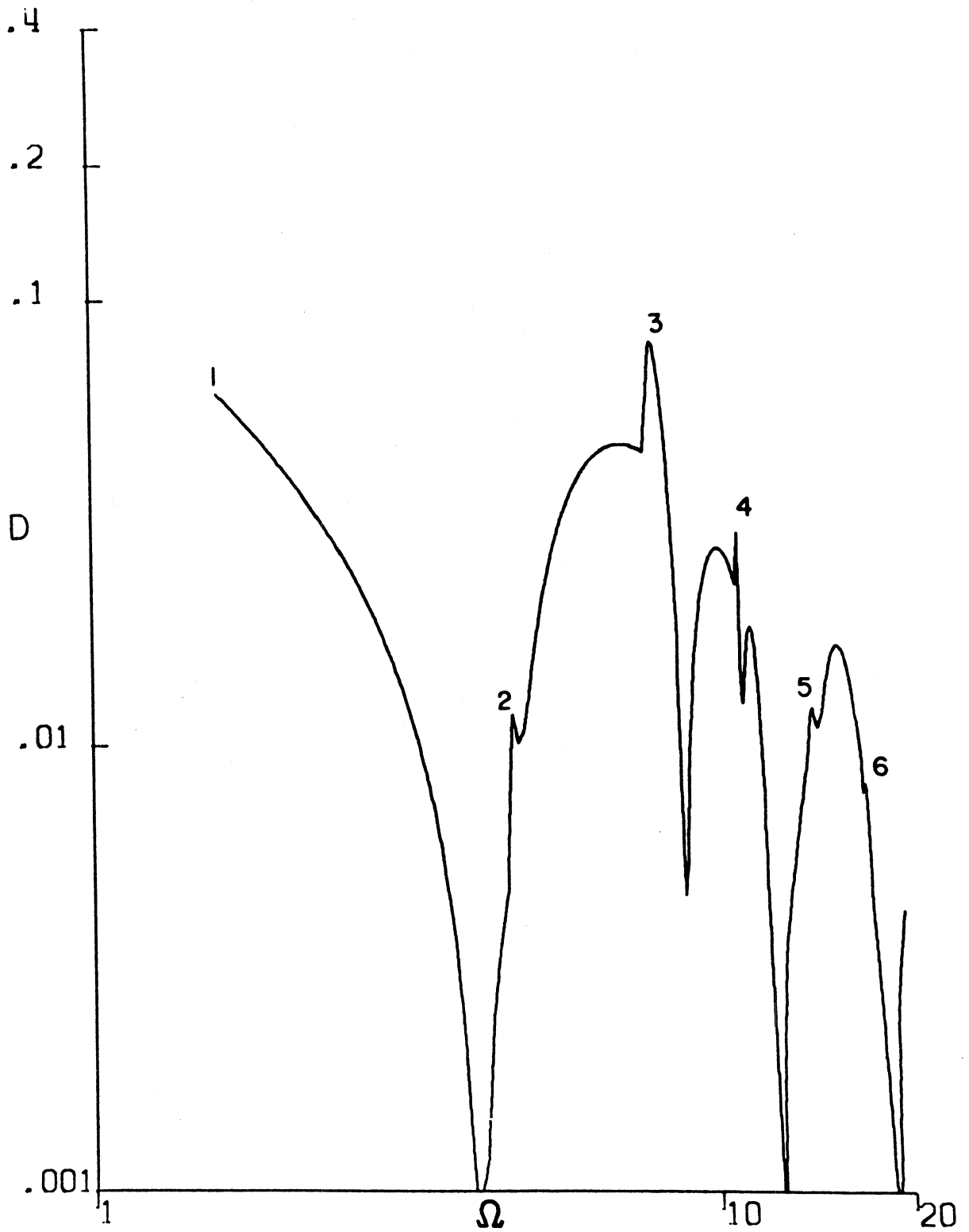
Figure 15. Progressing Waves -- Displacement Spectrum for Single
Layer and Deep Source: All Modes Included ($\beta_1 = \rho_1 = h_1$
$= 1$, $x = 2$, $z = 0$, $\xi = 0.7$, $\eta = 0.9$)
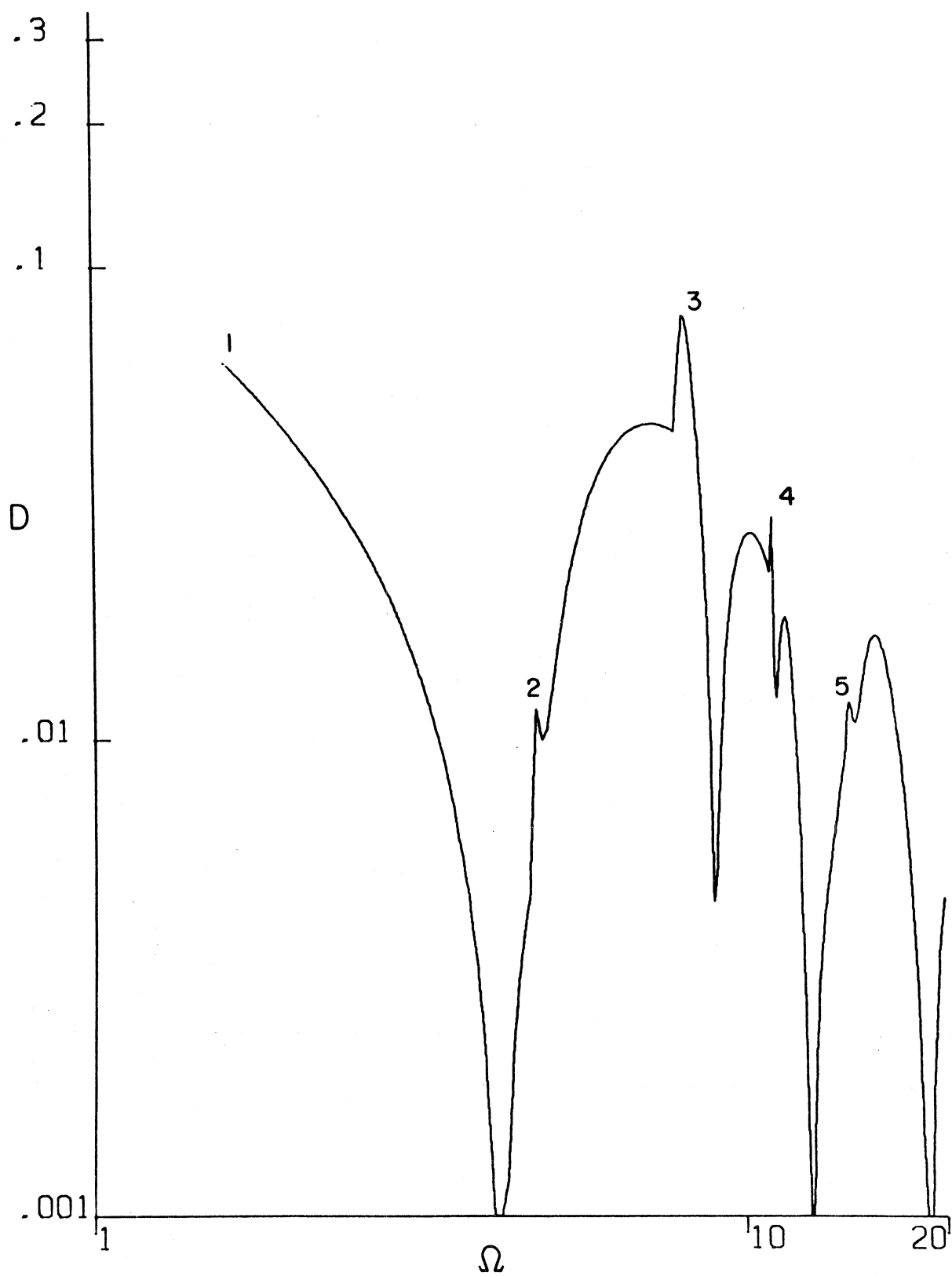
Figure 16. Progressing Waves -- Displacement Spectra for Single Layer and Deep Source: Sixth Mode Neglected ($\beta_1 = \rho_1 = h_1 = 1$, $x = 2$, $z = 0$, $\xi = 0.7$, $\eta = 0.9$)
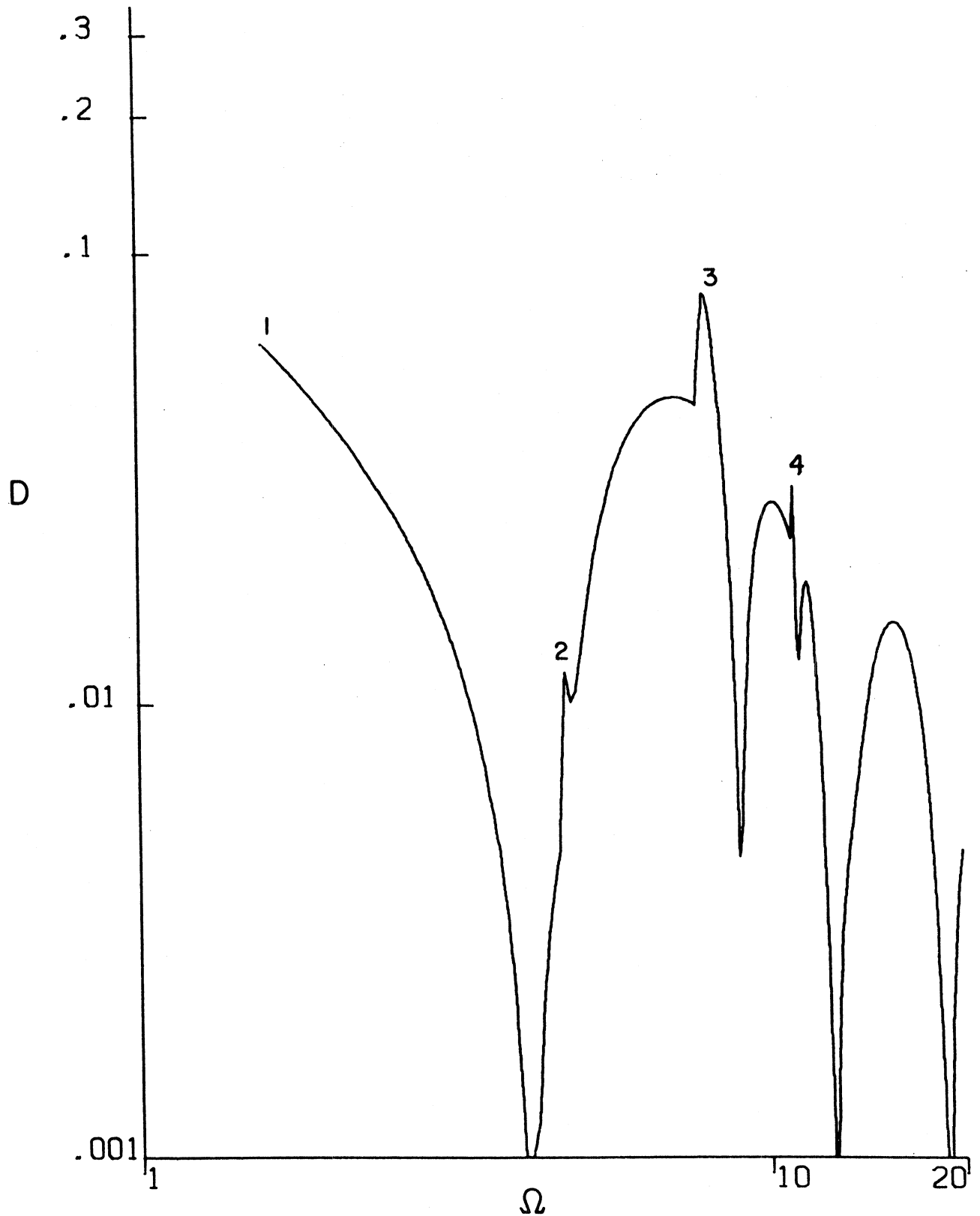
Figure 17.   Progressing Waves -- Displacement Spectra for Single Layer
and Deep Source: Fifth and Sixth Modes Neglected ($\beta_1 = \rho_1 =$
$h_1 = 1$, $x = 2$, $z = 0$, $\xi = 0.7$, $\eta = 0.9$)
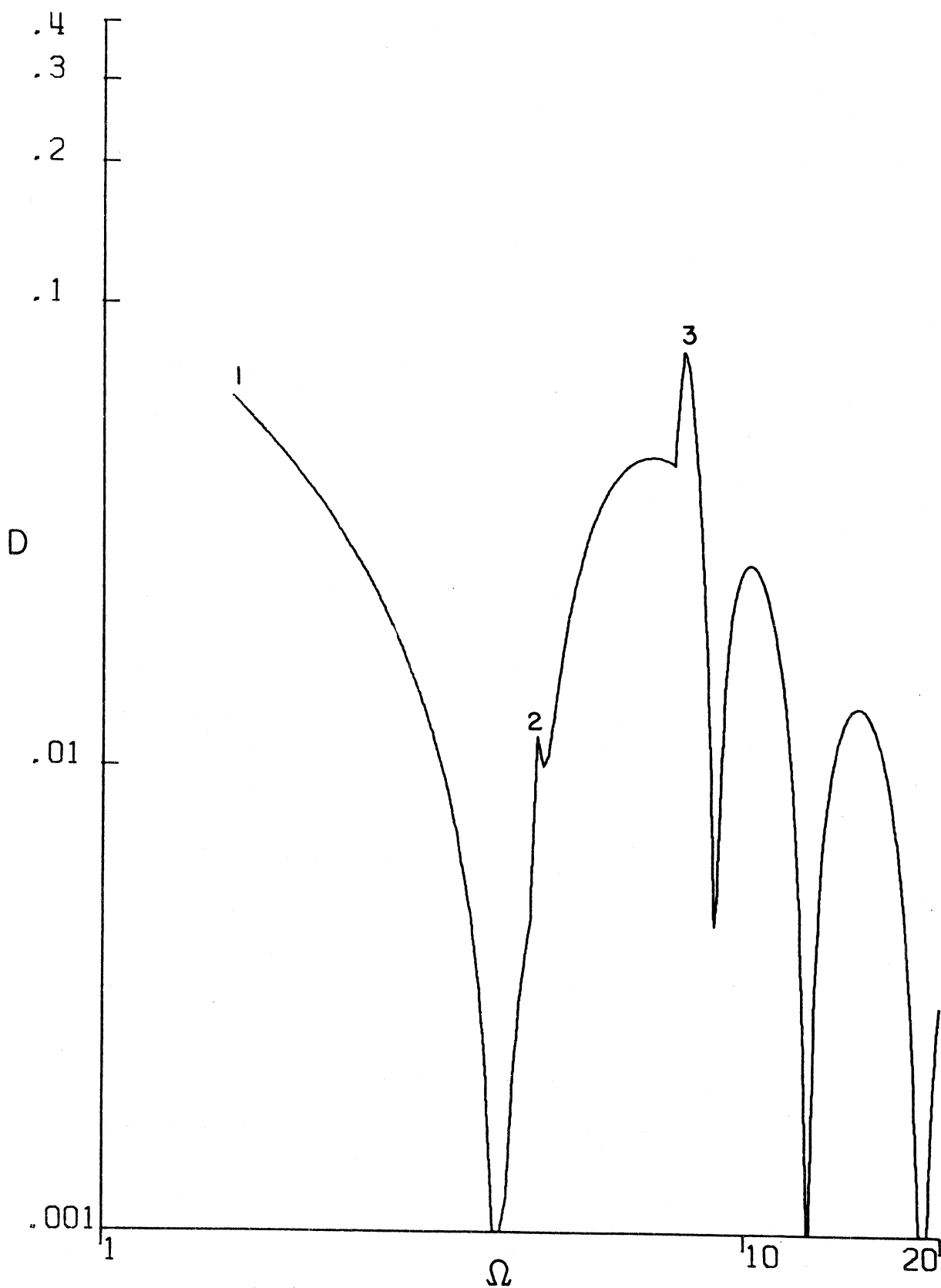
Figure 18. Progressing Waves -- Displacement Spectra for Single Layer and Deep Source: Only the First Three Modes Included ($\beta_1 = \rho_1 = h_1 = 1$, $x = 2$, $z = 0$, $\xi = 0.7$, $\eta = 0.9$)
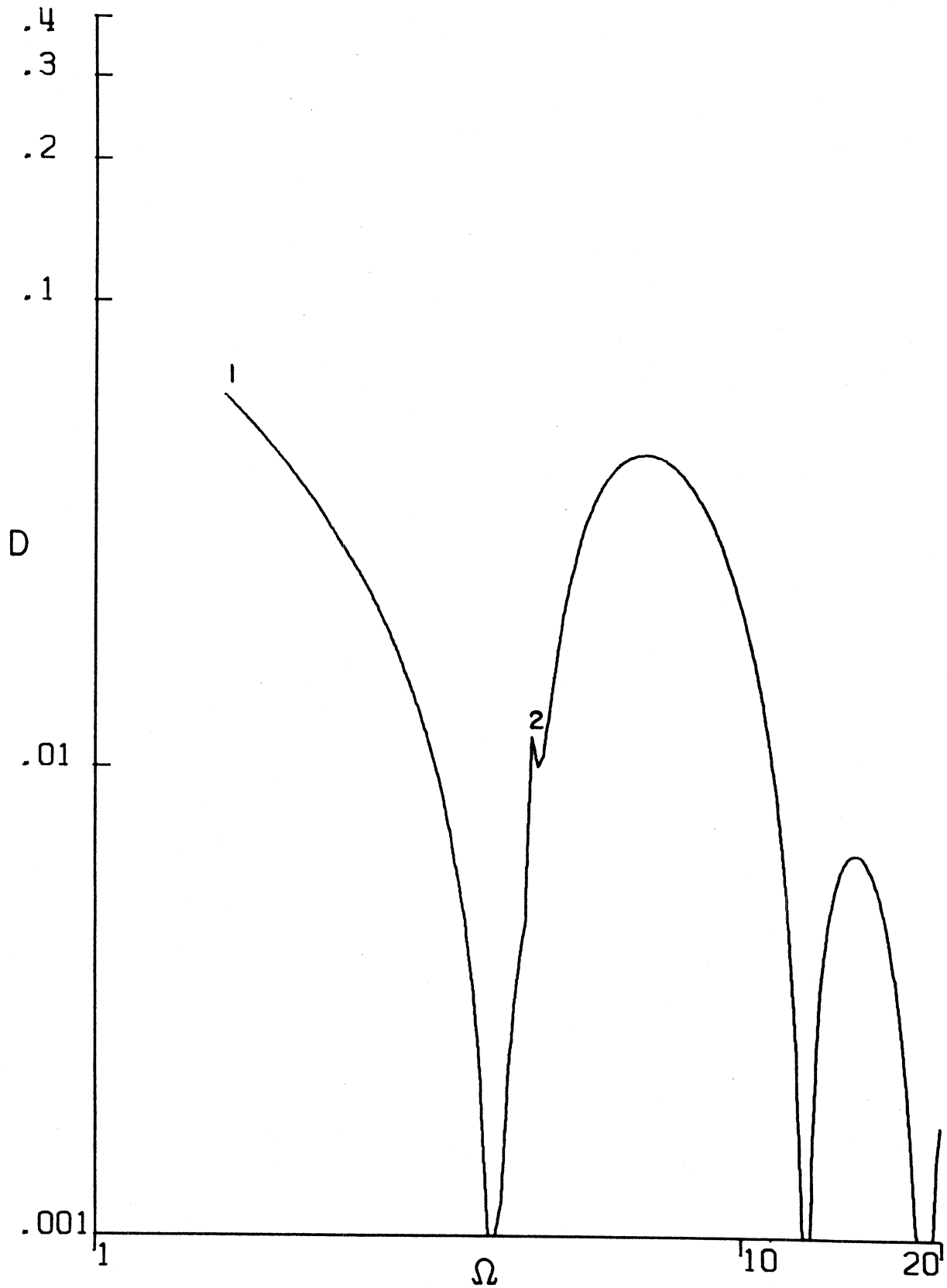
Figure 19. Progressing Waves -- Displacement Spectra for Single Layer and Deep Source: The First Two Modes Included ($\beta_1 = \rho_1 = h_1 = 1$, $x = 2$, $z = 0$, $\xi = 0.7$, $\eta = 0.9$)
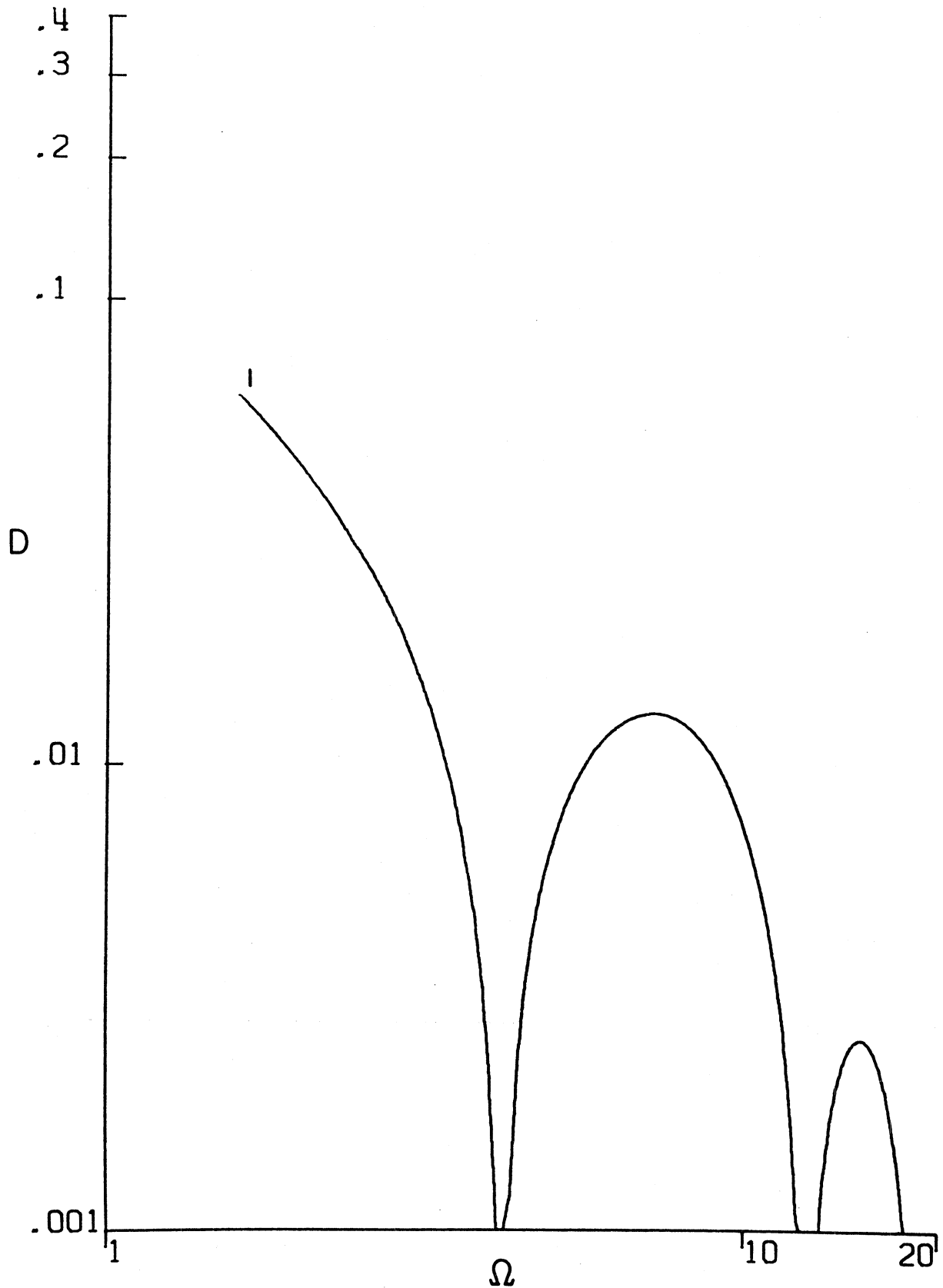
Figure 20. Progressing Waves -- Displacement Spectra for Single Layer and Deep Source: Only the First Mode Included ($\beta_1 = \rho_1 = h_1 = h_2 = 1$, $x = 2$, $z = 0$, $\xi = 0.7$, $\eta = 0.9$)

Examination of Figures 16 through 20 indicates that the relative contribution of the higher modes to the final Fourier amplitude spectra is small compared to the contribution of lower modes. Furthermore, the frequency spectrum decreases with increasing frequency. Study of (2.10) reveals that this decrease is proportional to $1/\omega$.

In source mechanism studies (e.g., Trifunac, 1972) the amplitudes of the Fourier amplitude spectra of far-field displacements are frequently related to seismic moment M_0 which represents the product of the near source rigidity μ, source area A and the average source dislocation $\bar{v}$. By computing α_1 from (2.9) and for sufficiently small ξ and η in (2.8) so that the contribution from second and higher modes can be neglected, one obtains $\alpha_1 = 2\mu_1 v_0(\eta-\xi)h_1$. Since $2v_0 \equiv \bar{v}$ it is seen that α_1 represents the seismic moment amplitude per unit length (along the y-axis) normalized with respect to the thickness of the layer as would be expected in this two-dimensional problem. As can be seen from Figure 15, the cut-off frequencies are easily detected through jumps in the spectrum amplitudes. From the frequency equation (1.24), it follows that the cut-off frequencies are given by

$$\Omega_{co} = (2j-1)\pi/2, \quad j=1,2, \ldots .$$

For the model with two layers, the frequency equation is specified by (1.26) and the dispersion curves are shown in Figure 3. The set of reduced eigenfunctions can be deduced from (1.34) to be

$$\phi_j(z) = \begin{cases} \cos q_1^j z & , \quad 0 \le z \le z_1 \\ a_2^j \cos q_2^j + b_2^j \sin q_1^j z & , \quad z_1 \le z \le z_2 \quad ; j=1,2, \ldots, N \end{cases} \tag{2.11}$$

with q_1^j, q_2^j defined by (1.27).

To find the frequency response (1.45) one calculates first the expansion coefficients α_j. In the case of two layers, the expansion coefficients (1.43) are

$$\alpha_j = \frac{(\phi_j, g)}{(\phi_j, \phi_j)} \tag{2.12}$$

$$(\phi_j, g) = 2\left\{ \mu_1 \left[\int_0^{z_1} + \int_{2z_2 - z_1}^{2z_2} \cos q_1^j z \cdot g(z) dz \right] \right.$$

$$\left. + \mu_2 a_2 \left[\int_{z_1}^{z_2} + \int_{z_2}^{2z_2 - z_1} \cos q_2^j z \cdot g(z) dz \right] \right\} \tag{2.13}$$

$$(\phi_j, \phi_j) = \mu_1 \left[G_1^j(1,z) \Big|_0^{z_1} + G_1^j(1,z) \Big|_{2z_2 - z_1}^{2z_2} \right] + \mu_2 \left\{ \left[a_2^j G_1^j(2,z) \right.\right.$$

$$\left. + b_2^j G_2^j(2,z) \right]_{z_1}^{z_2} + \left[a_2^j G_1^j(2,z) + b_2^j G_2^j(2,z) \right]_{z_2}^{2z_2 - z_1} \right\} \tag{2.14}$$

$$G_{1,2}^j(m,z) \equiv z \pm \frac{\sin 2q_m^j z}{2q_m^j} \quad , \quad m=1,2,\ldots, \tag{2.15}$$

The function $G_{1,2}(m,z)$ being introduced to simplify notation and $f(z)\Big|_a^b \equiv f(b) - f(a)$.

For dispersion relations shown in Figure 3, the corresponding Fourier amplitude spectra of displacements are shown in Figure 21. As indicated earlier, all spatial and temporal variables are normalized with respect to the thickness of the top layer h_1 and t_0, respectively. It is further assumed that $h_1 = 1$ and $t_0 = 1$.
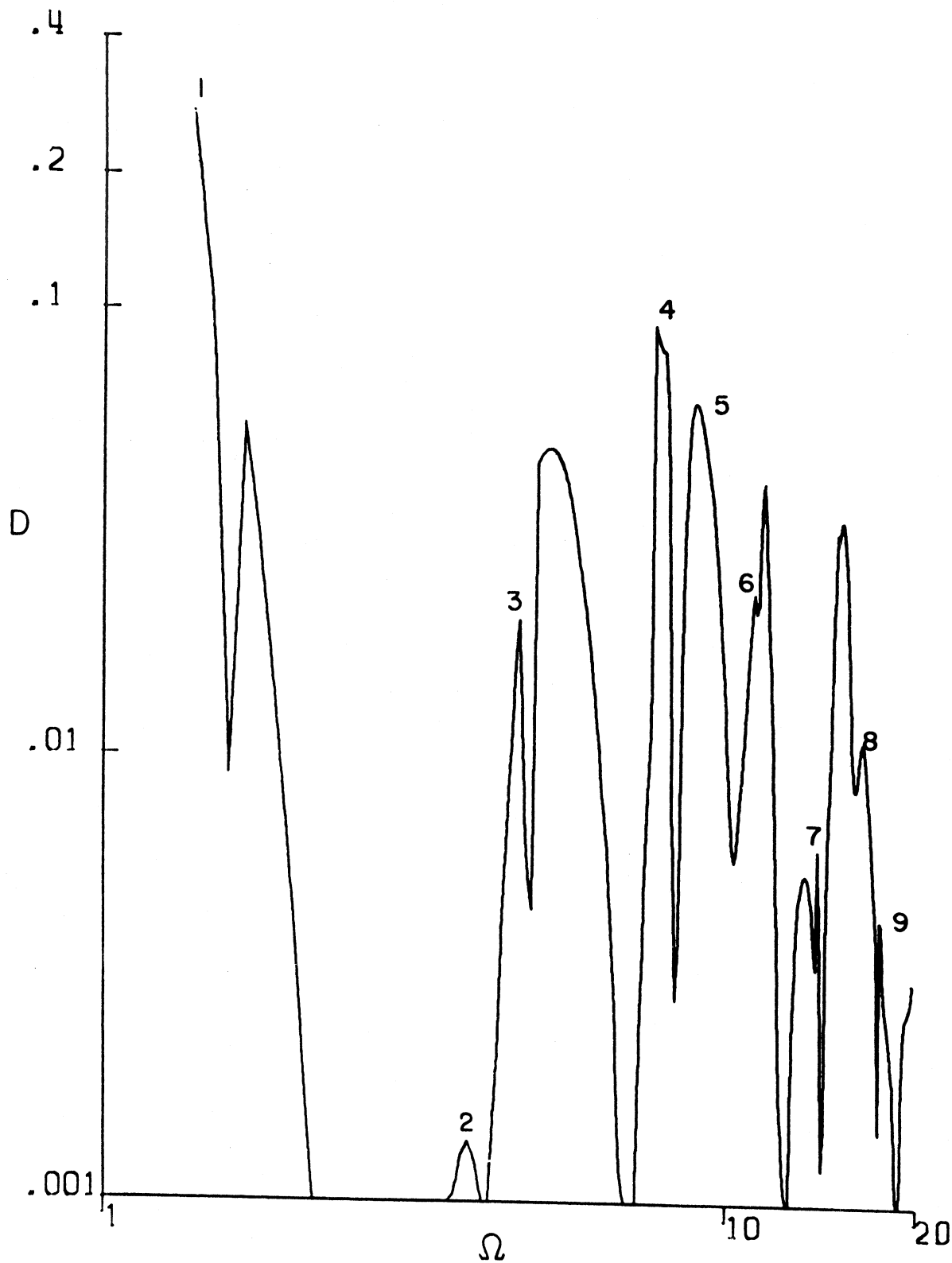
Figure 21.   Progressing Waves -- Displacement Spectra for Two Layers and Deep Source: All Modes Included ($\beta_1 = \rho_1 = h_1 = h_2 = 1$, $\beta_1 = \rho_1 = 2$, $\xi = 0.7$, $\eta = 0.9$, $x = 2$, $z = 0$)

For the frequency range under consideration and the set of parameters specified, there are nine modes of progressive waves present in the model. To demonstrate dependence of the spectral amplitudes on the progressive modes, the spectra are evaluated by consecutively neglecting higher modes one by one. The results are shown in Figures 21 through 29.

An example of the frequency spectra for progressive waves and for three-layer model ($h_1 = h_2 = h_3 = 1$, $\rho_1 = 1$, $\rho_2 = 2$, $\rho_3 = 3$, $\beta_1 = 1$, $\beta_2 = 2$, $\beta_3 = 3$) is shown in Figure 30. There exist eleven progressive modes in the frequency range considered.

2.3.2 Locally Standing Waves

The cut-off frequencies in the case of a single layer are given by $\Omega_{co}^j = (2j-1)\pi/2$, $j=1,2, \ldots$. The frequency equation (1.24) implies that for $\Omega < \Omega_{co}^j$ corresponding wave number is purely imaginary. This can be used in the frequency equation which reduces to a family of circles in the Ω-κ space

$$\Omega^2 + \kappa_j^2 = [(2j-1)\pi/2]^2 , \qquad j=1,2,3, \ldots . \qquad (2.16)$$

Dimensionless frequency Ω and wave number κ have been defined by (1.25). The family of circles is shown in Figure 2. It is seen that at each frequency, there exist infinitely many wave numbers, which satisfy the frequency equation (2.16). However, due to exponential decay of the frequency response in x (see 2.10), only the first few roots will contribute significantly to motions at any station ($x > 0, z$). In particular, the total of six modes are included in Figure 2.

An example of the frequency spectra for a single layer due to
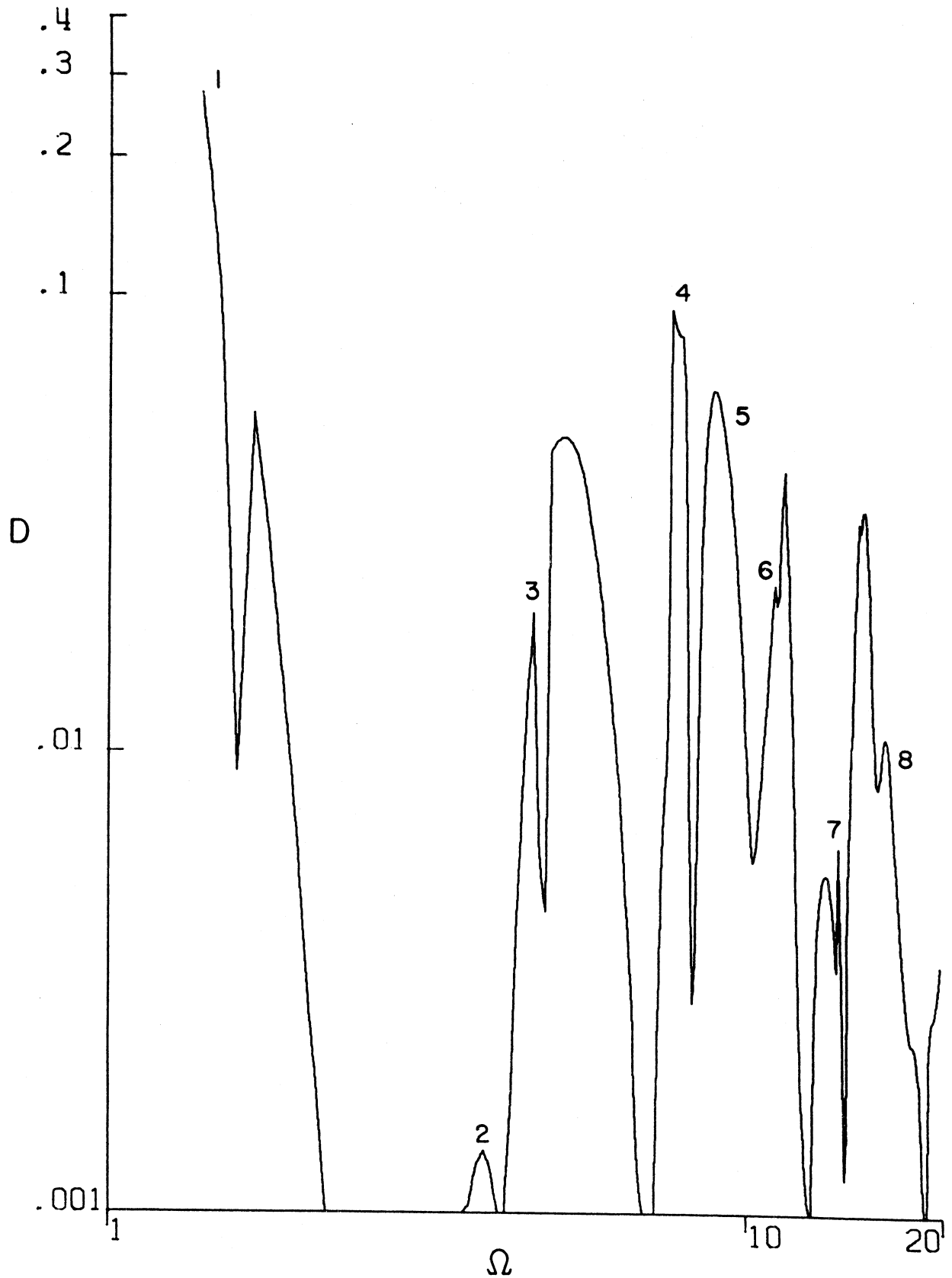
Figure 22. Progressing Waves -- Displacement Spectra for Two Layers and Deep Source: Ninth Mode Neglected ($\beta_1 = \rho_1 = h_1 = h_2 = 1$, $\beta_2 = \rho_2 = 2$, $\xi = 0.7$, $\eta = 0.9$, $x = 2$, $z = 0$)
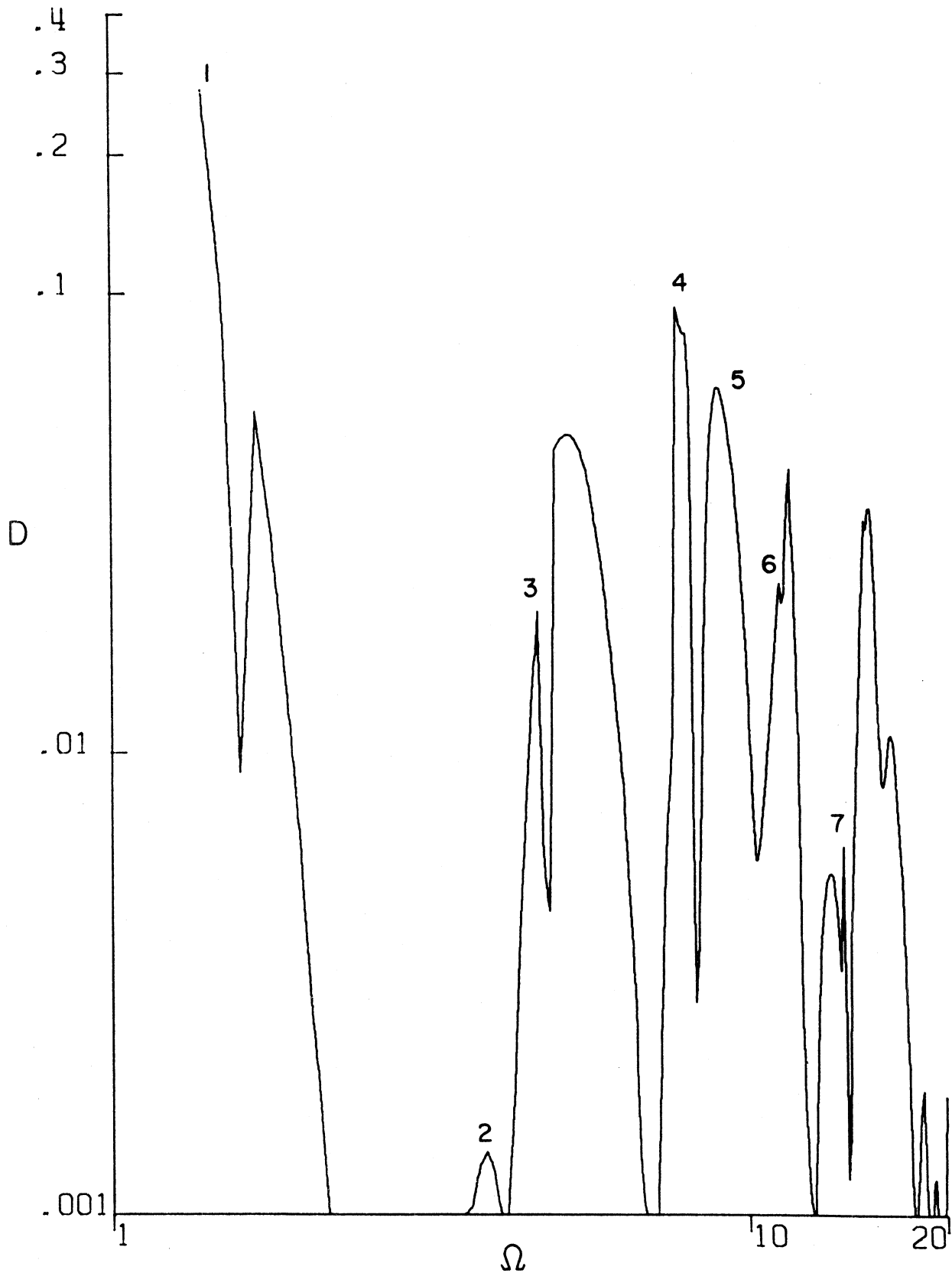
Figure 23. Progressing Waves -- Displacement Spectra for Two Layers and Deep Source: First Seven Modes Included ($\beta_1 = \rho_1 = h_1 = h_2 = 1$, $\beta_2 = \rho_2 = 2$, $\xi = 0.7$, $\eta = 0.9$, $x = 2$, $z = 0$)
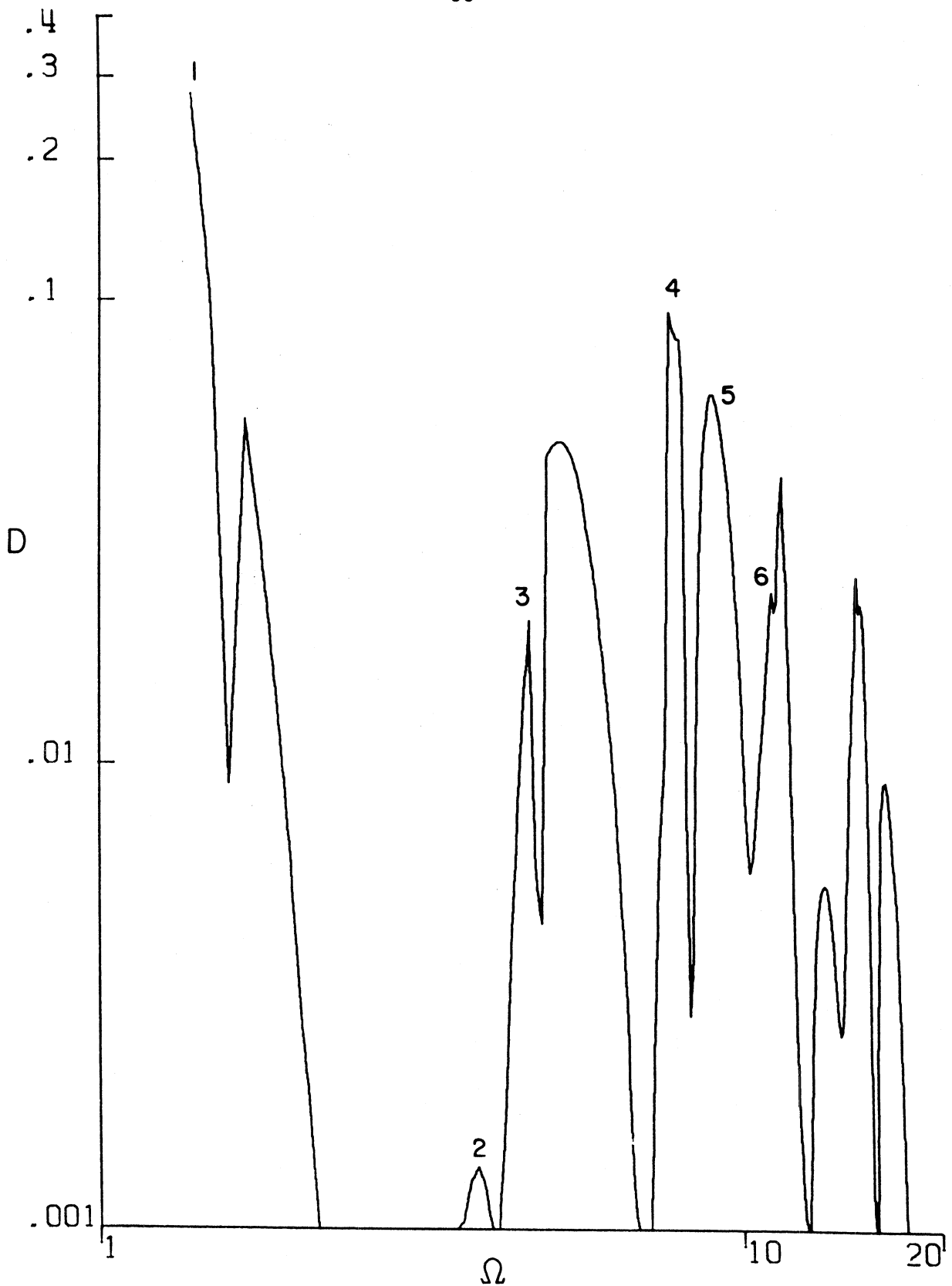
Figure 24. Progressing Waves -- Displacement Spectra for Two Layers and Deep Source: First Six Modes Included ($\beta_1 = \rho_1 = h_1 = h_2 = 1$, $\beta_2 = \rho_2 = 2$, $\xi = 0.7$, $\eta = 0.9$, $x = 2$, $z = 0$)
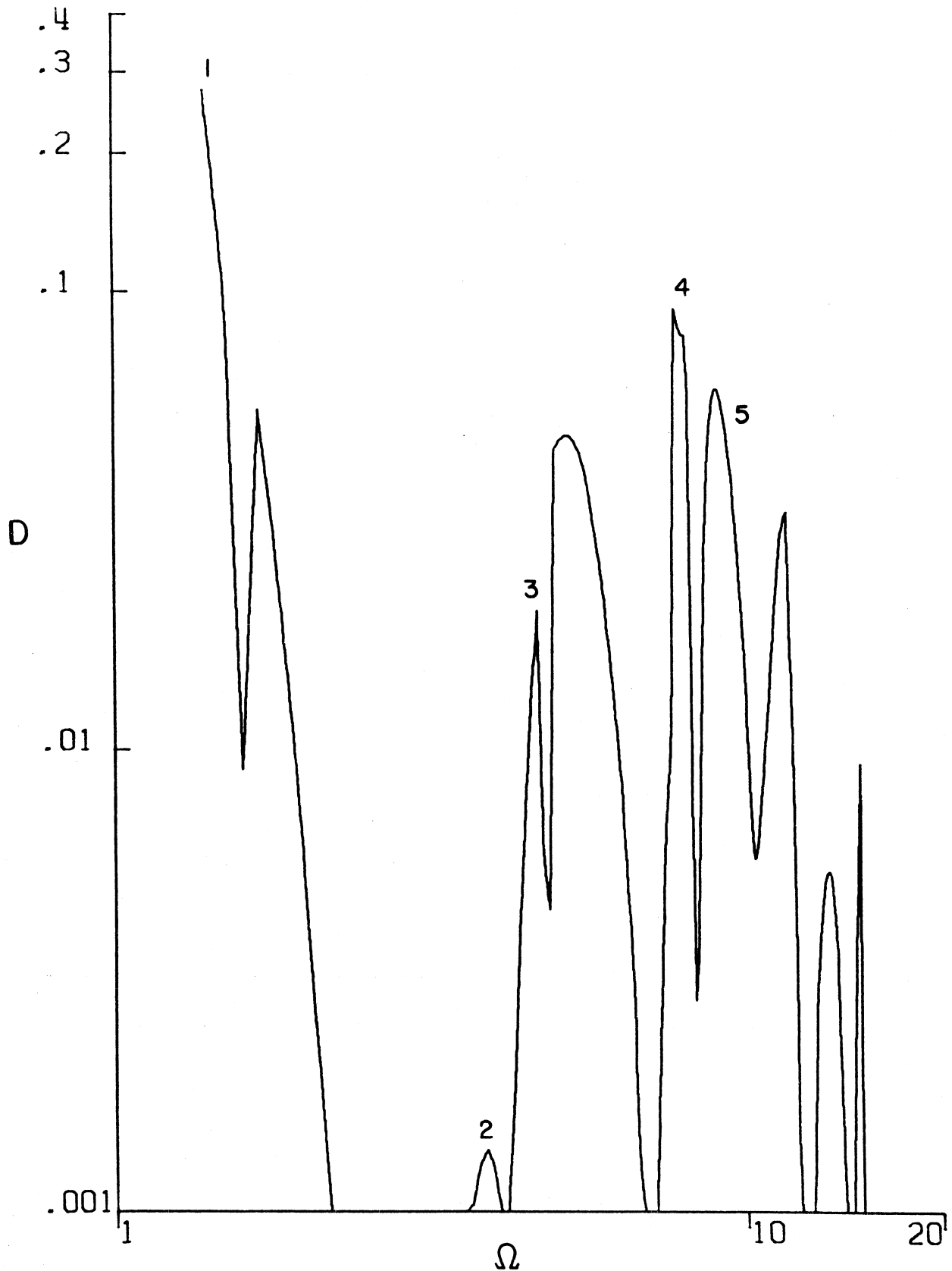
Figure 25. Progressing Waves -- Displacement Spectra for Two Layers and Deep Source: First Five Modes Includes ($\beta_1 = \rho_1 = h_1 = h_2 = 1$, $\beta_2 = \rho_2 = 2$, $\xi = 0.7$, $\eta = 0.9$, $x = 2$, $z = 0$)
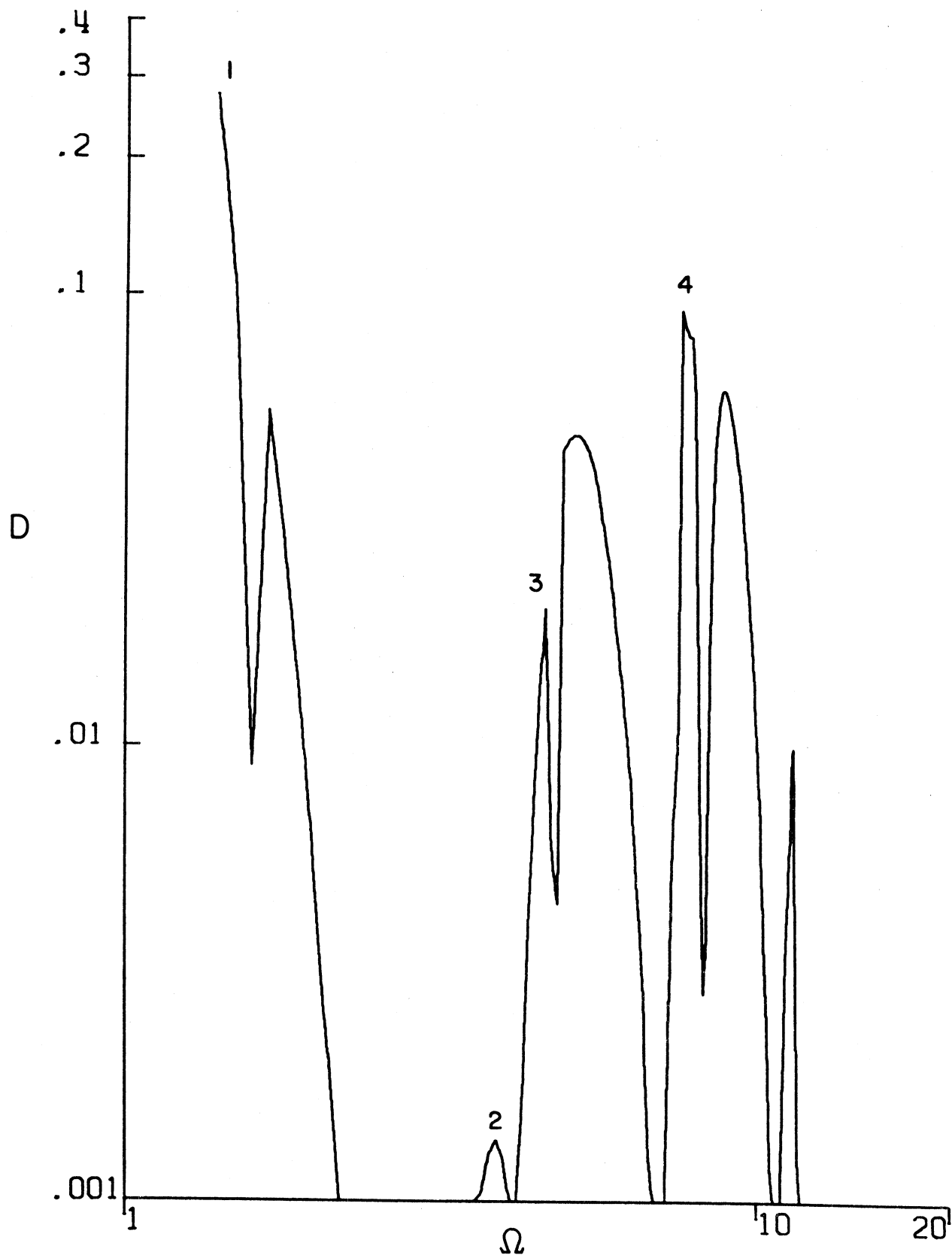
Figure 26. Progressing Waves -- Displacement Spectra for Two Layers and Deep Source: First Four Modes Included ($\beta_1 = \rho_1 = h_1 = h_2 = 1$, $\beta_2 = \rho_2 = 2$, $\xi = 0.7$, $\eta = 0.9$, $x = 2$, $z = 0$)
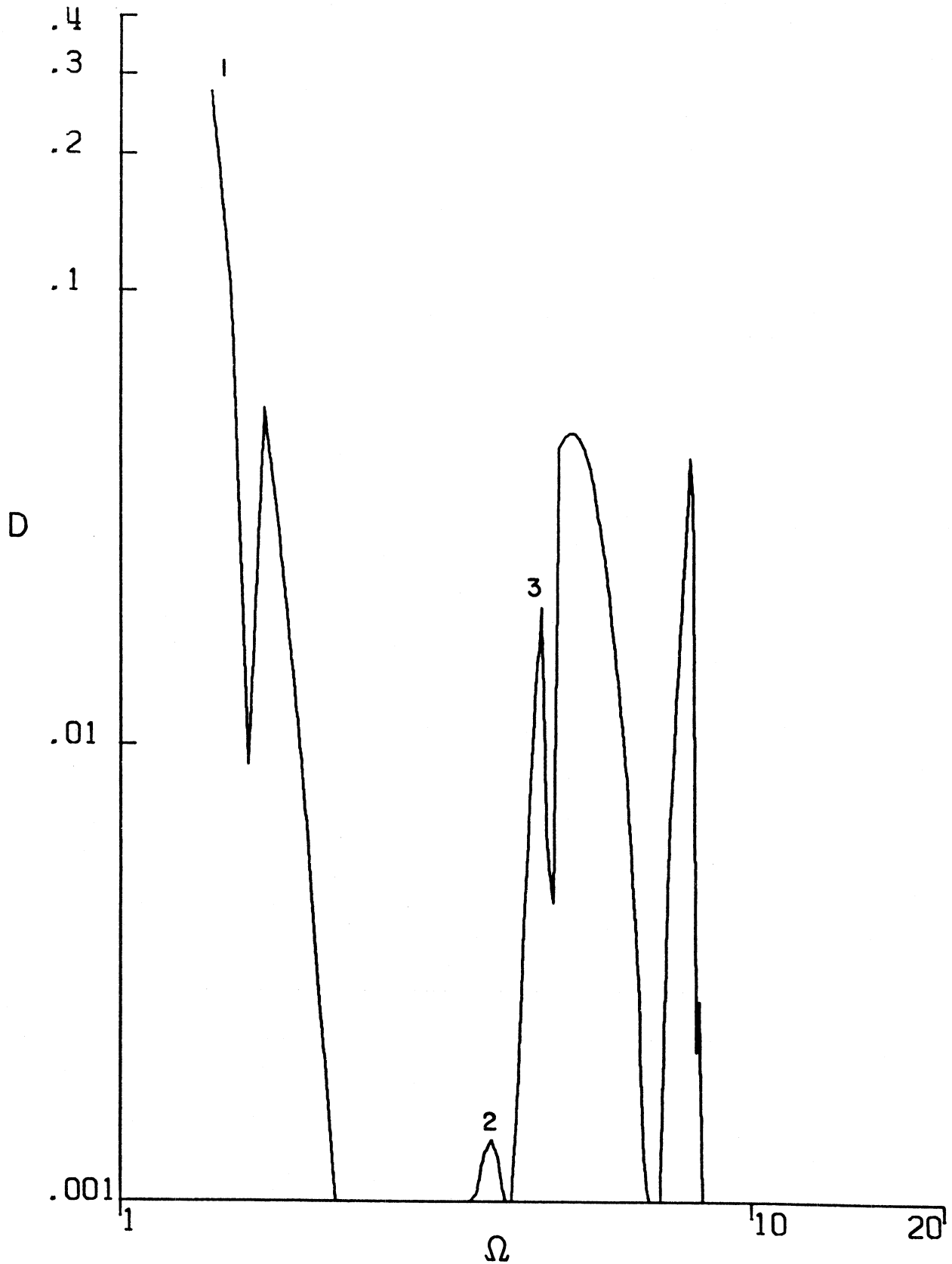
Figure 27. Progressing Waves -- Displacement Spectra for Two Layers and Deep Source: First Three Modes Included ($\beta_1 = \rho_1 = h_1 = h_2 = 1$, $\beta_2 = \rho_2 = 2$, $\xi = 0.7$, $\eta = 0.9$, $x = 2$, $z = 0$)
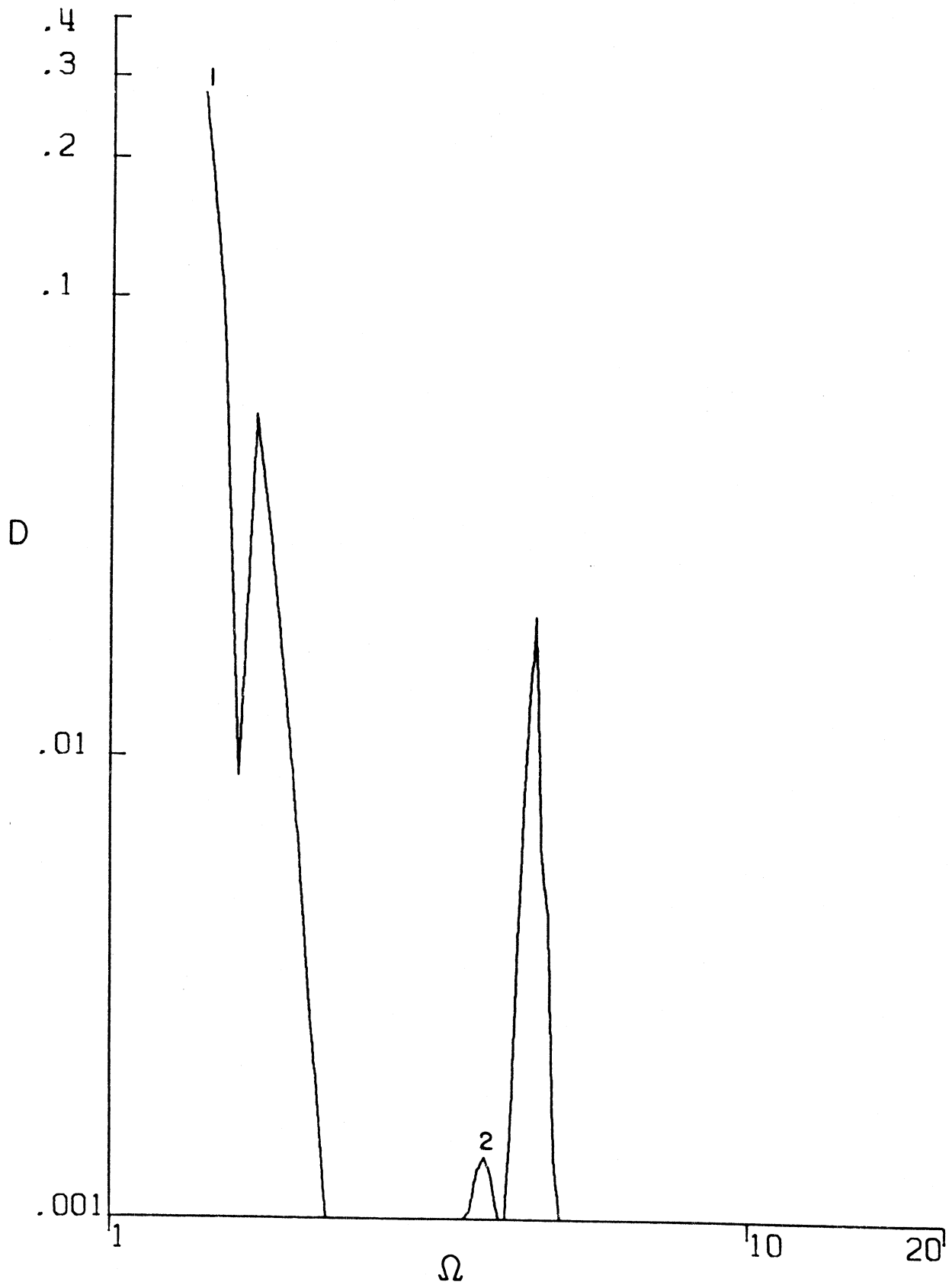
Figure 28. Progressing Waves -- Displacement Spectra for Two Layers and Deep Source: First Two Modes Included ($\beta_1 = \rho_1 = h_1 = h_2 = 1$, $\beta_2 = \rho_2 = 2$, $\xi = 0.7$, $\eta = 0.9$, $x = 2$, $z = 0$)
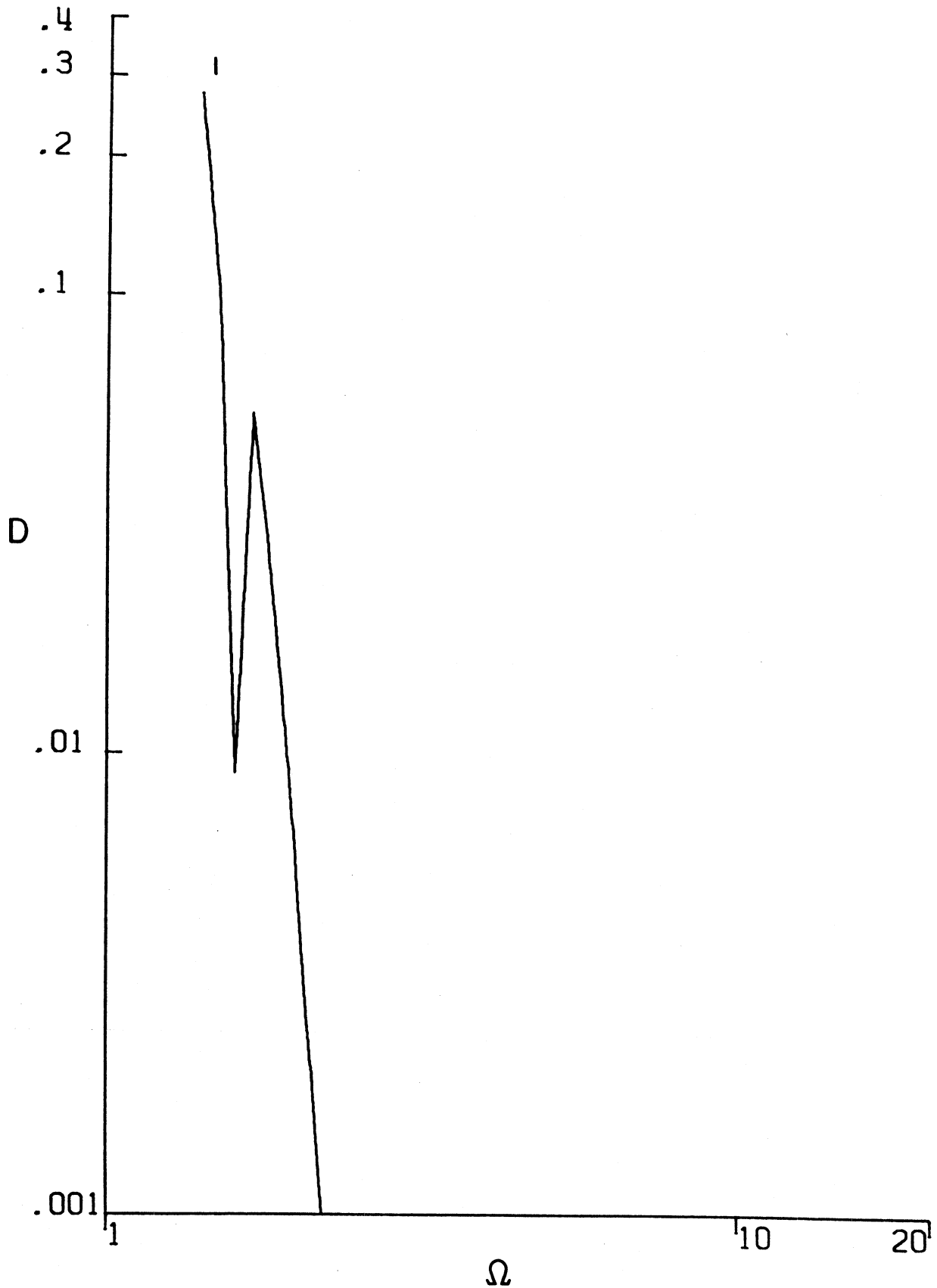
Figure 29. Progressing Waves -- Displacement Spectra for Two Layers and Deep Source: First Mode Only ($\beta_1 = \rho_1 = h_1 = h_2 = 1$, $\beta_2 = \rho_2 = 2$, $\xi = 0.7$, $\eta = 0.9$, $x = 2$, $z = 0$)
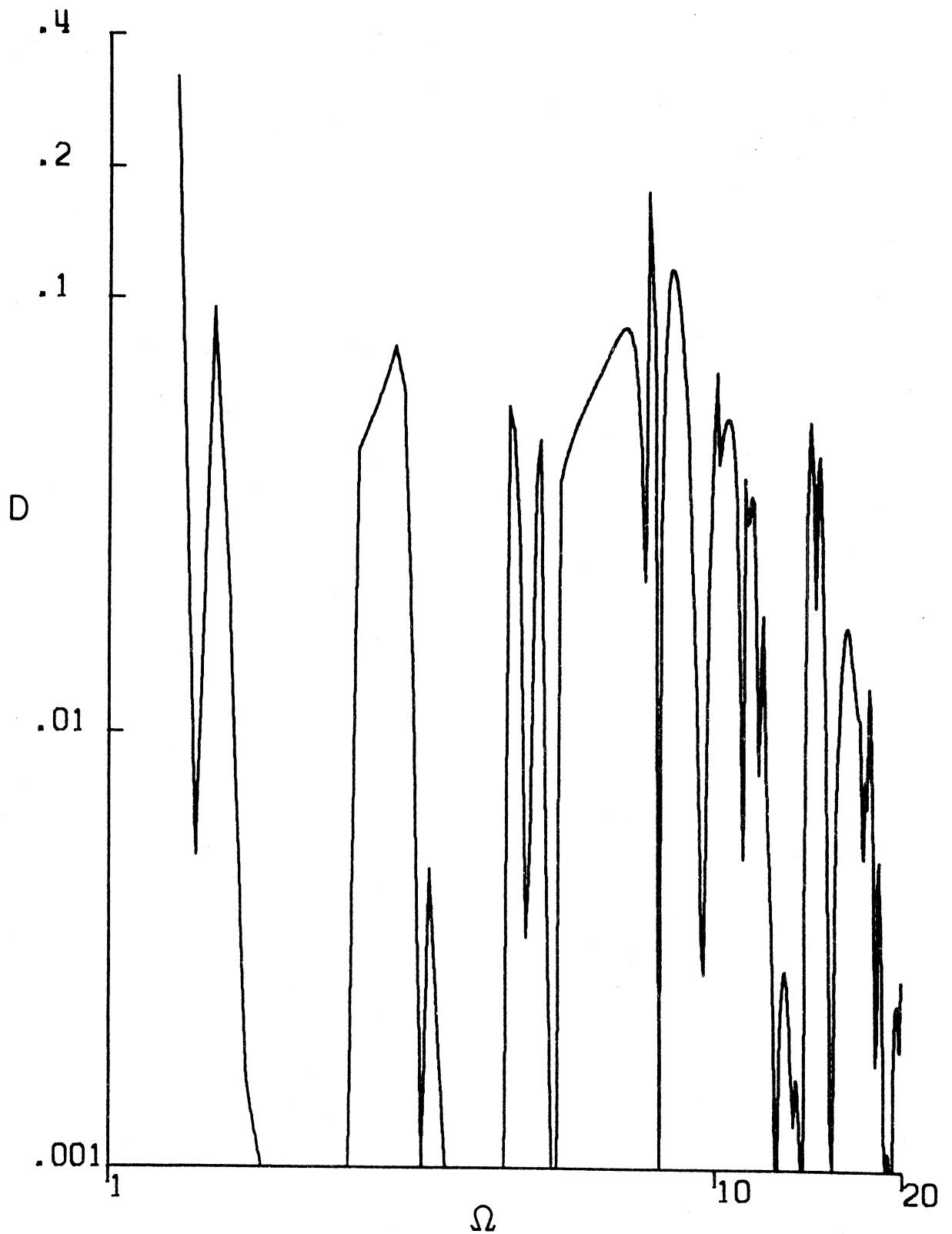
Figure 30. Progressing Waves -- Displacement Spectra for Three Layers and Deep Source ($\beta_1 = \rho_1 = h_1 = h_2 = h_3 = 1$, $\beta_2 = \rho_2 = 2$, $\beta_3 = \rho_3 = 3$, $\xi = 0.7$, $\eta = 0.9$, $x = 2$, $z = 0$)

progressing waves is shown in Figure 15. For the dimensionless frequency
between zero and the first cut-off frequency, only locally standing
waves are excited in the system. For the frequencies greater than the
first cut-off frequency in addition to locally standing waves (e.g., Fig-
ure 31) the progressive waves are induced as well.

The exponential term exp(-kx) for the locally standing waves causes
their amplitudes to diminish with increase of distance x. However, at
cut-off frequencies, the wave number becomes zero and it follows that
the corresponding waves are constant along x. The apparent wave num-
ber being zero is equivalent to the vertical ray incidence upon the
stress-free surface, and consequently corresponds to pure standing
wave contribution to the frequency spectra. This corresponds to peaks
in the frequency spectra in Figure 31.

An example of locally standing waves in two layers is shown in
Figure 32. As in the case of a single layer, at each frequency, there
exist infinitely many wave numbers which satisfy the frequency equa-
tion (1.26). Due to exponential term $exp(-k_j x)$ only several modes are
needed in evaluation of spectral amplitudes at a station $(x > 0, z)$. The
parameters for this example are the same as in the case of the progres-
sive wave shown in Figure 5.

An example for locally standing waves in the case of three layers
is shown in Figure 33.
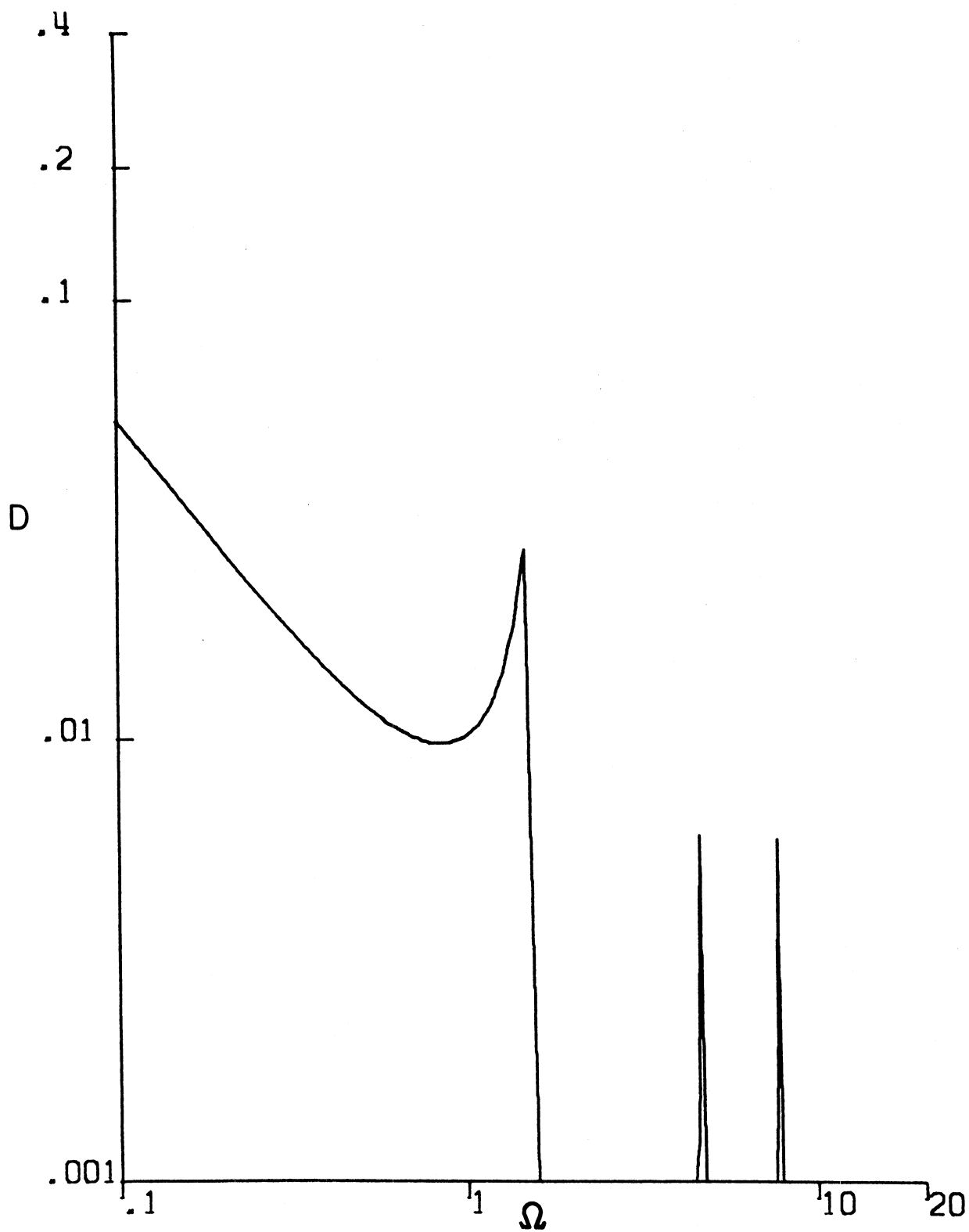
Figure 31. Locally Standing Waves -- Displacement Spectra for One
Layer and Deep Source ($\beta_1 = \rho_1 = h_1 = 1$, $\xi = 0.7$, $\eta = 0.9$,
$\zeta = 0.2$, $x = 2$, $z = 0$)
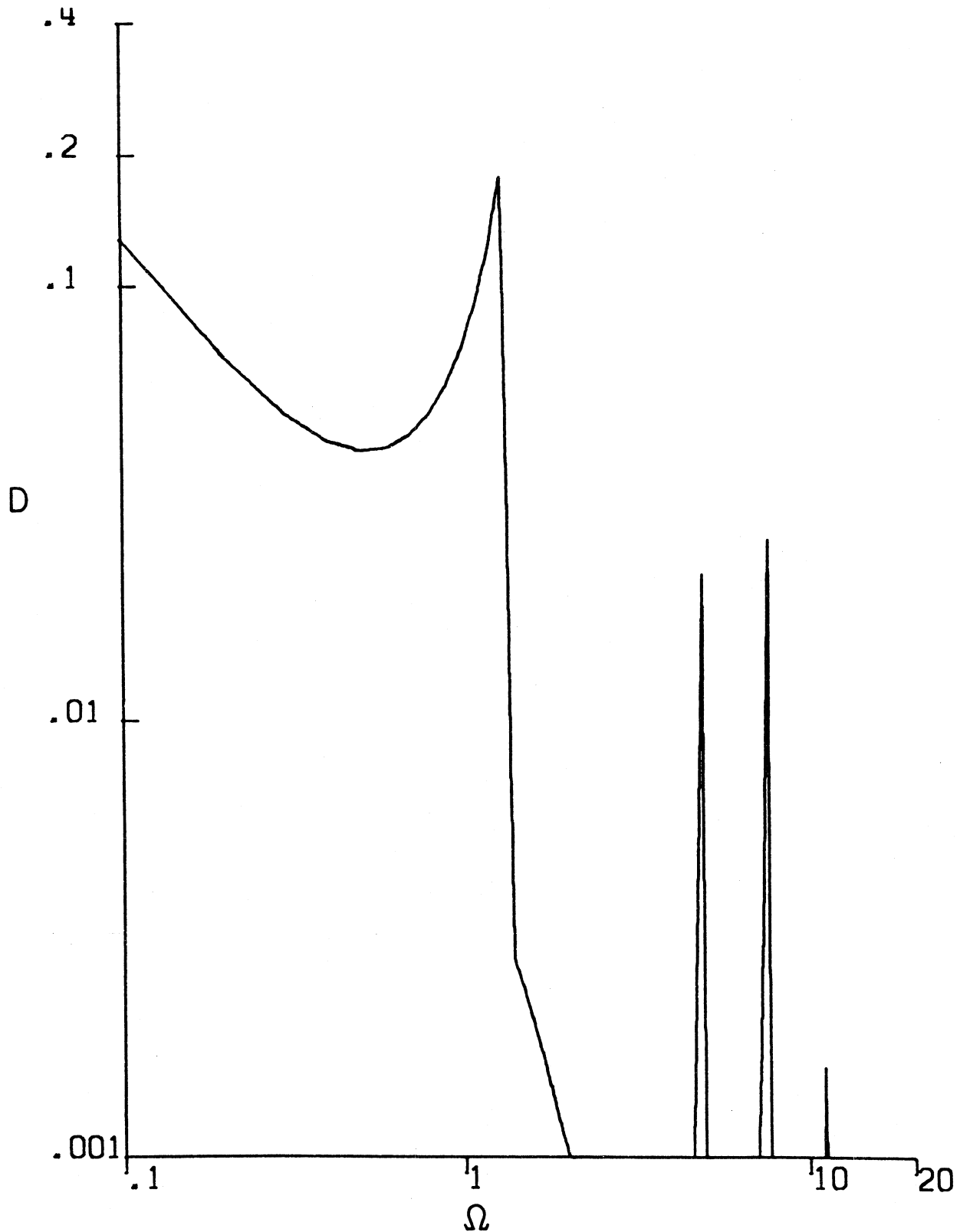
Figure 32. Locally Standing Waves -- Displacement Spectra for Two
Layers and Deep Source ($\beta_1 = \rho_1 = h_1 = h_2 = 1$, $\beta_2 = \rho_2 = 2$,
$\xi = 0.7$, $\eta = 0.9$, $x = 2$, $z = 0$)
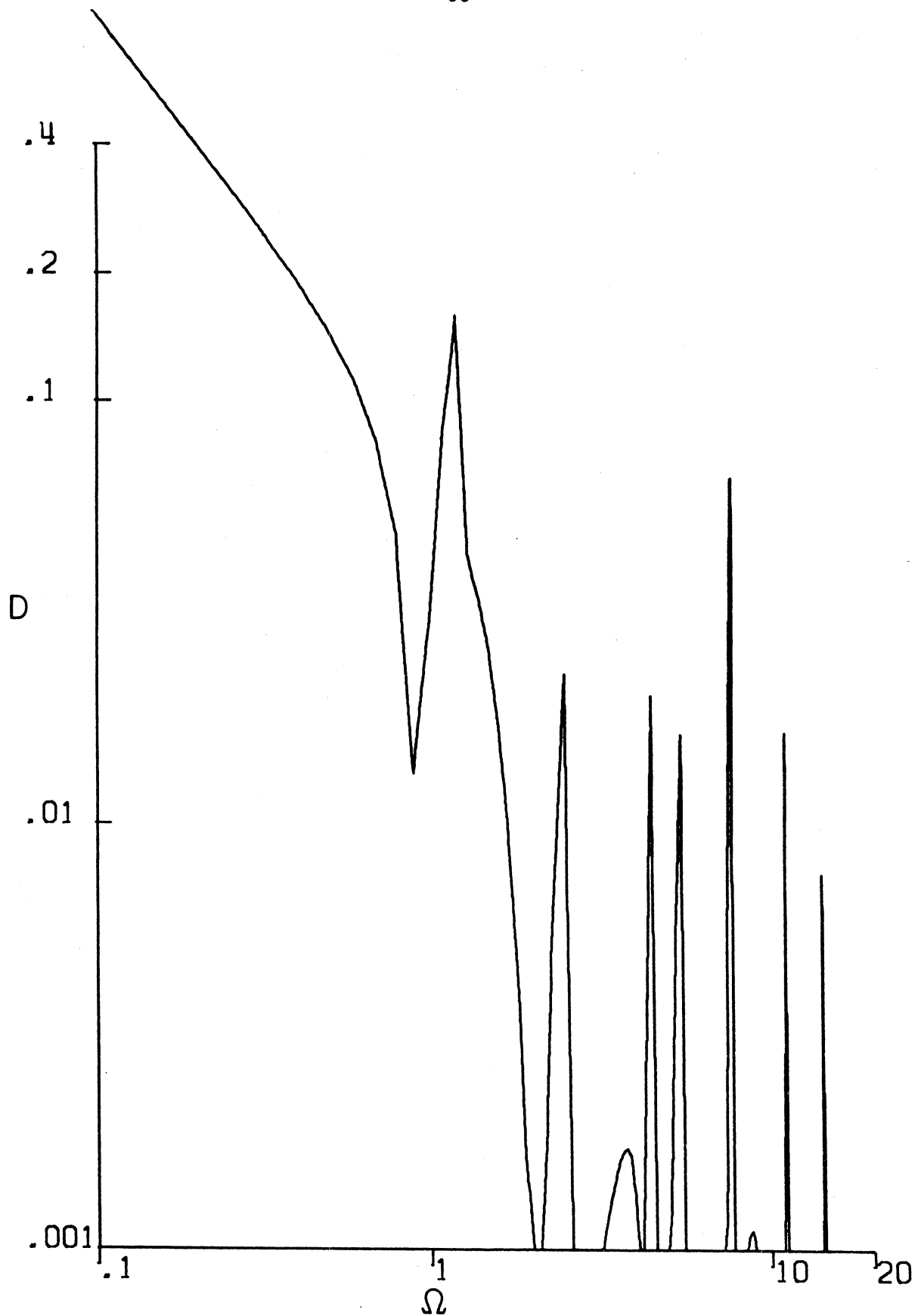
Figure 33. Locally Standing Waves -- Displacement Spectra for Three
Layers and Deep Source ($\beta_1 = \rho_1 = h_1 = h_2 = h_3 = 1$, $\beta_2 = \rho_2 = 2$,
$\beta_3 = \rho_3 = 3$, $x = 2$, $z = 0$, $\xi = 0.7$, $\eta = 0.9$)

64

2.4 Comparison of Shallow versus Deep Source

2.4.1 Single Layer: Progressive Waves

The amplitude spectrum for progressive waves shown in Figure 15 is evaluated for relatively deep source ($\xi = 0.70$, $\eta = 0.9$; see (2.2) for definition of the depth of the source). To evaluate the effect of source depth, we next consider a source to be near the surface, z=0. In particular, the coefficients ξ and η are chosen to be zero and 0.20, respectively. The temporal part of the input field f(t) is assumed to be the same as in the case of deep source (Figure 10).

The spectral amplitudes for shallow source are presented in Figure 34. It is seen that the spectra at lower frequencies are greater for the shallow source compared to the deep source. At higher frequencies, the opposite is true. This is to be expected on the physical grounds. Indeed, for deep source, one expects higher frequency modes to contribute more to the spectral amplitudes compared to the lower frequency modes. In the case of shallow source, one expects the opposite; i.e., the contribution of lower frequency modes to be more pronounced in relation to the contribution of the higher frequencies.

2.4.2 Two Layers: Progressive Waves

The spectrum shown in Figure 21 is evaluated for "deep source," while the one presented in Figure 35 is for the shallow source. Comparison of these results implies the same conclusion as in the case of a single layer. With increase of source depth the higher frequency modes are excited more compared to the lower frequency modes. However, in the case of two layers, this is much more pronounced compared to the single layer problem. Even greater
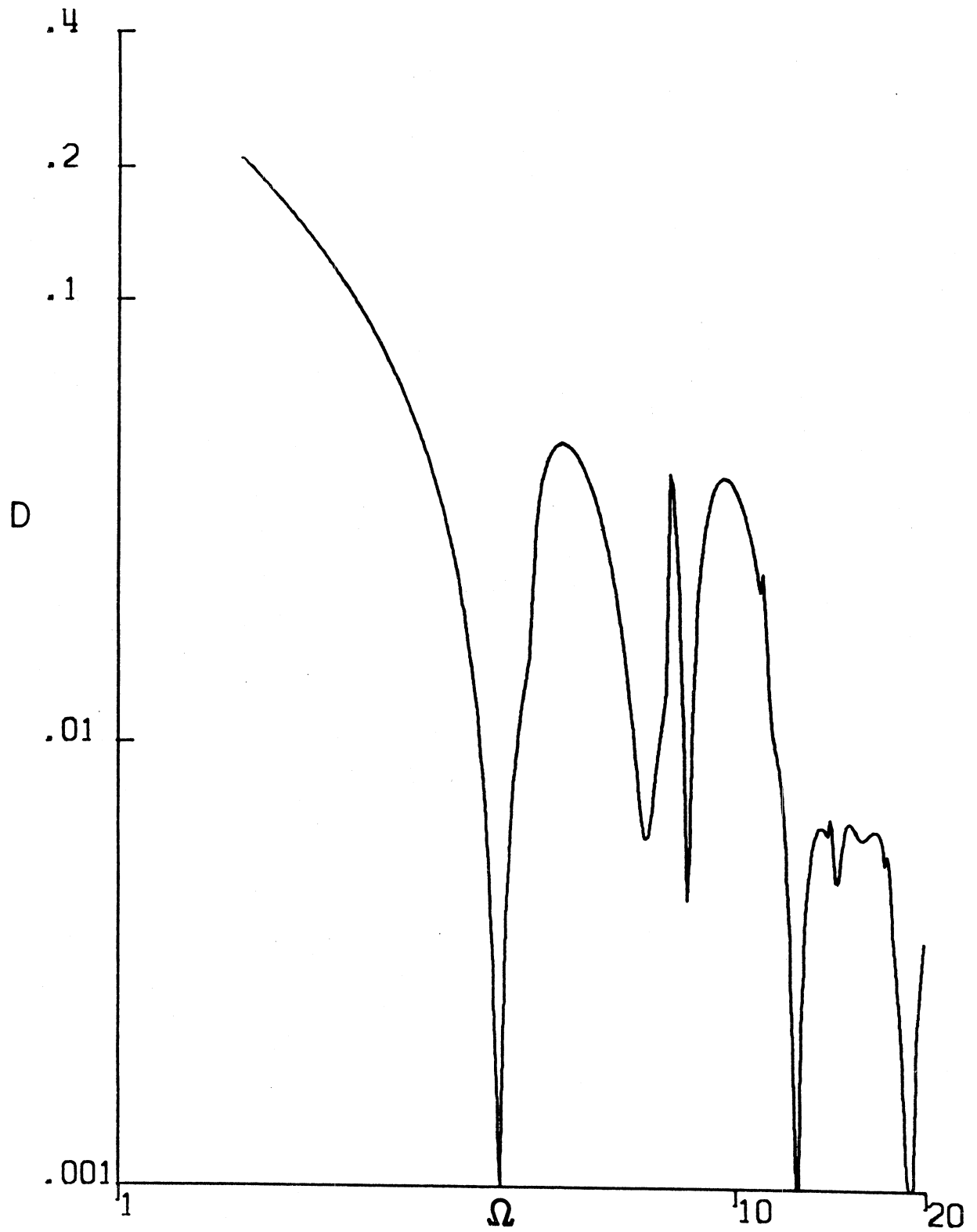
Figure 34. Progressing Waves -- Displacement Spectra for Single Layer and Shallow Source ($\beta_1 = \rho_1 = h_1 = 1$, $\xi = 0$, $\eta = 0.2$, $x = 2$, $z = 0$)
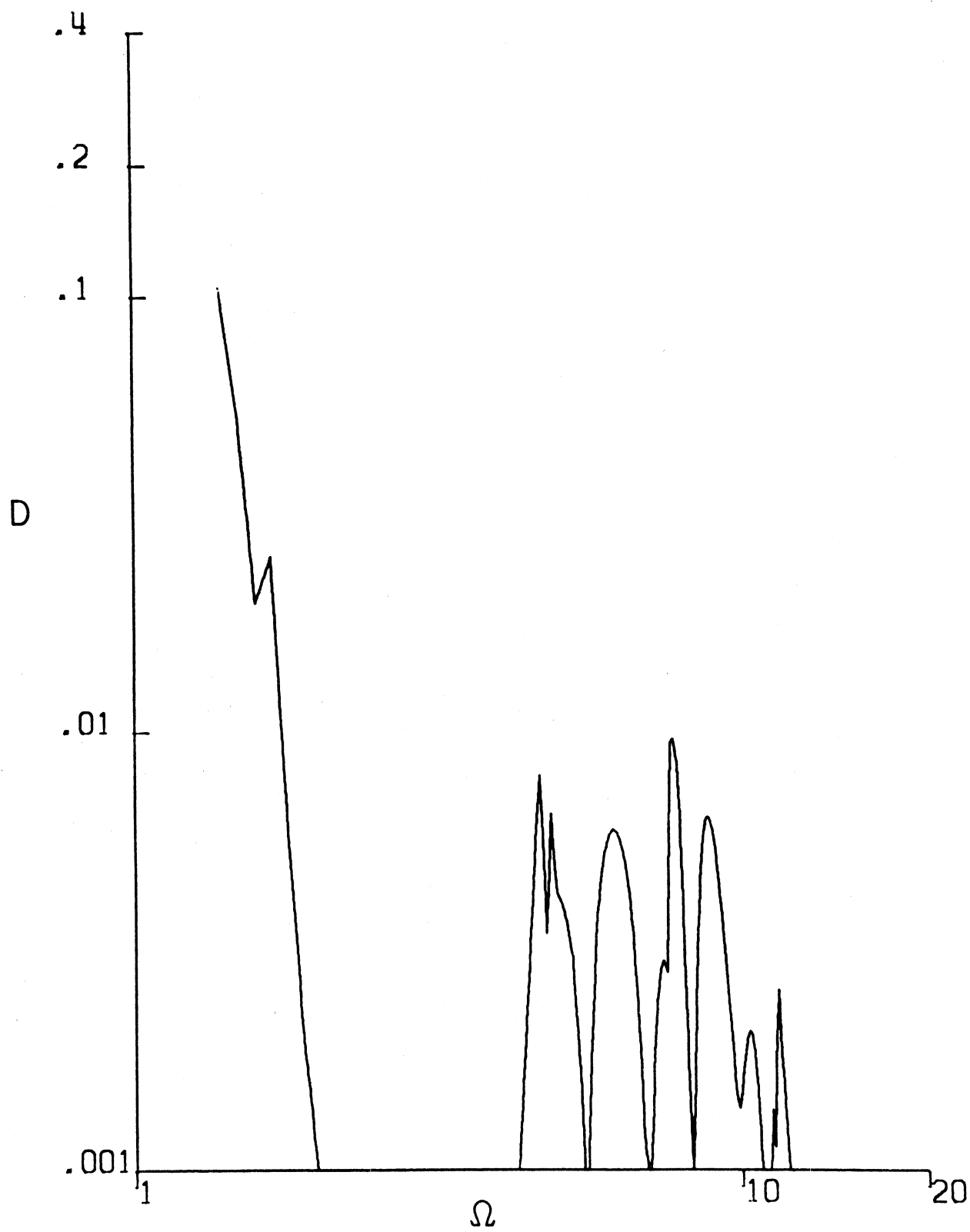
Figure 35. Progressing Waves -- Displacement Spectra for Two Layers and Shallow Source ($\beta_1 = \rho_1 = h_1 = h_2 = 1$, $\beta_2 = \rho_2 = 2$, $\xi = 0$, $\eta = 0.2$, $x = 2$, $z = 0$)

influence of source depth is demonstrated in the three layer problem. The corresponding spectrum for shallow source is given in Figure 36. The model parameters ($\rho_1 = 1$, $h_1 = 1$, $\beta_1 = 1$, $\rho_2 = 2$, $h_2 = 2$, $\beta_2 = 2$, $\rho_3 = 3$, $h_3 = 3$, $\beta_3 = 3$, $a = 1$, $v_0 = 1$, $\xi = 0.2$) are the same in both cases. Comparison with one and two layer examples shows the similar influence of the depth of the source on the observed Fourier amplitude spectra of displacements.

2.4.3 Locally Standing Waves

Examination of the displacement spectral amplitudes for deep source (Figures 32 and 33) and shallow source (Figures 37 and 38) reveal the similar characteristics as in the case of progressive waves: the deeper the source, the more high frequency modes are excited in the system; this sensitivity increases with the number of layers.

Analysis of Figures 31, 32, 33, 37 and 38 will show that as the dimensionless frequency approaches zero, the Fourier spectrum amplitudes of standing waves behave like $1/\omega$. This is as one would expect since as $\omega \to 0$, $f_1(t)$ in (2.2) approaches $aH(t)$ and its Fourier amplitude spectrum is a/ω. After all transient motions are over for $\omega \to 0$, $\sum_j \alpha_j \phi_j e^{ik_j}$ represents contribution of locally standing waves to $v(x,z,t)$ and physically reduces to a static amplitude representing permanent ground deformation at (x,z).

2.5 Energy Density

2.5.1 Single Layer

Energy density e (see (1.54)) is next evaluated on the surface $z=0$ for various x and ω. Analysis of expression (2.9) for expansion
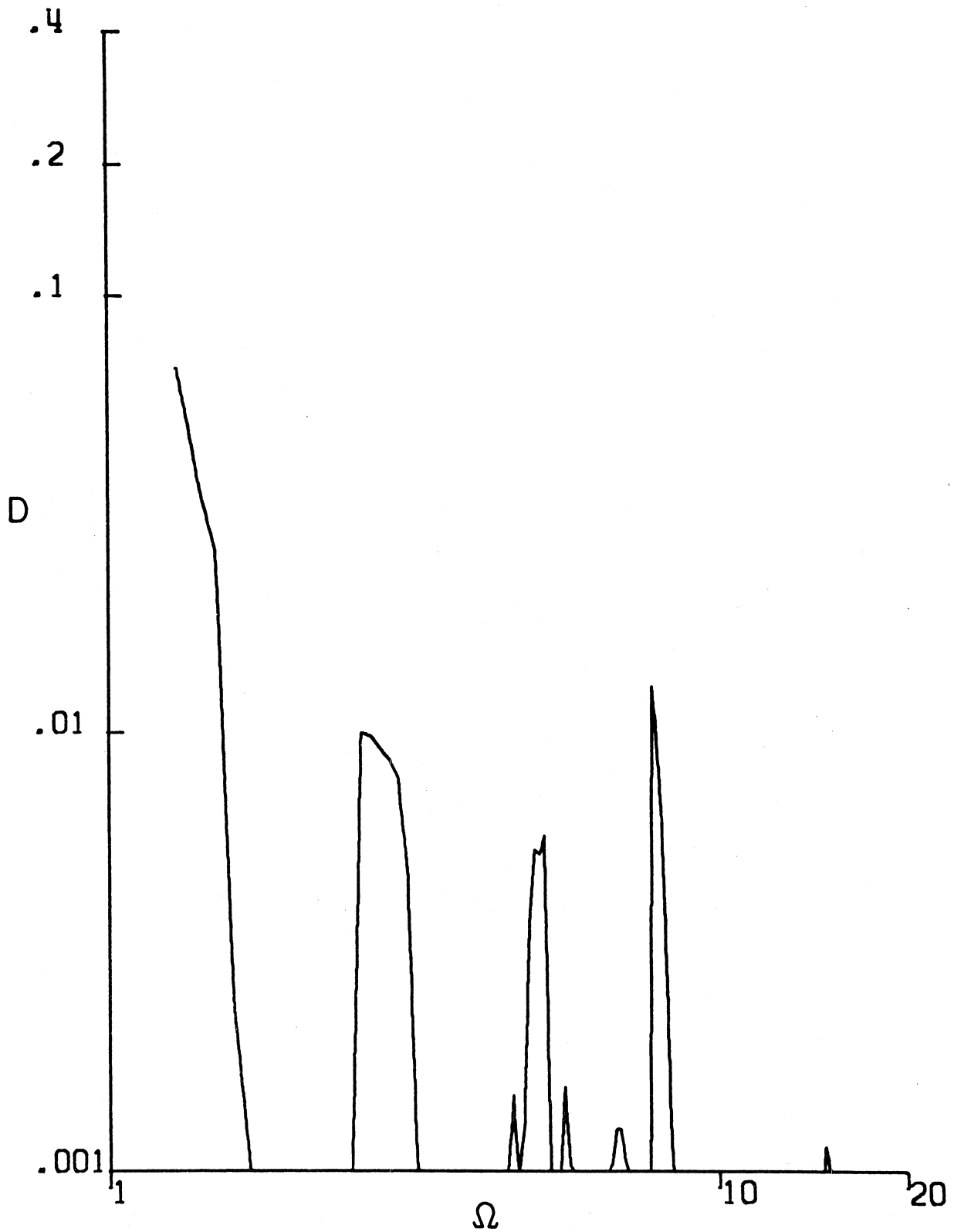
Figure 36. Progressing Waves -- Displacement Spectra for Three Layers and Shallow Source ($\beta_1 = \rho_1 = h_1 = h_2 = h_3 = 1$, $\beta_2 = \rho_2 = 2$, $\beta_3 = \rho_3 = 3$, $\xi = 0$, $\eta = 0.2$, $x = 2$, $z = 0$)
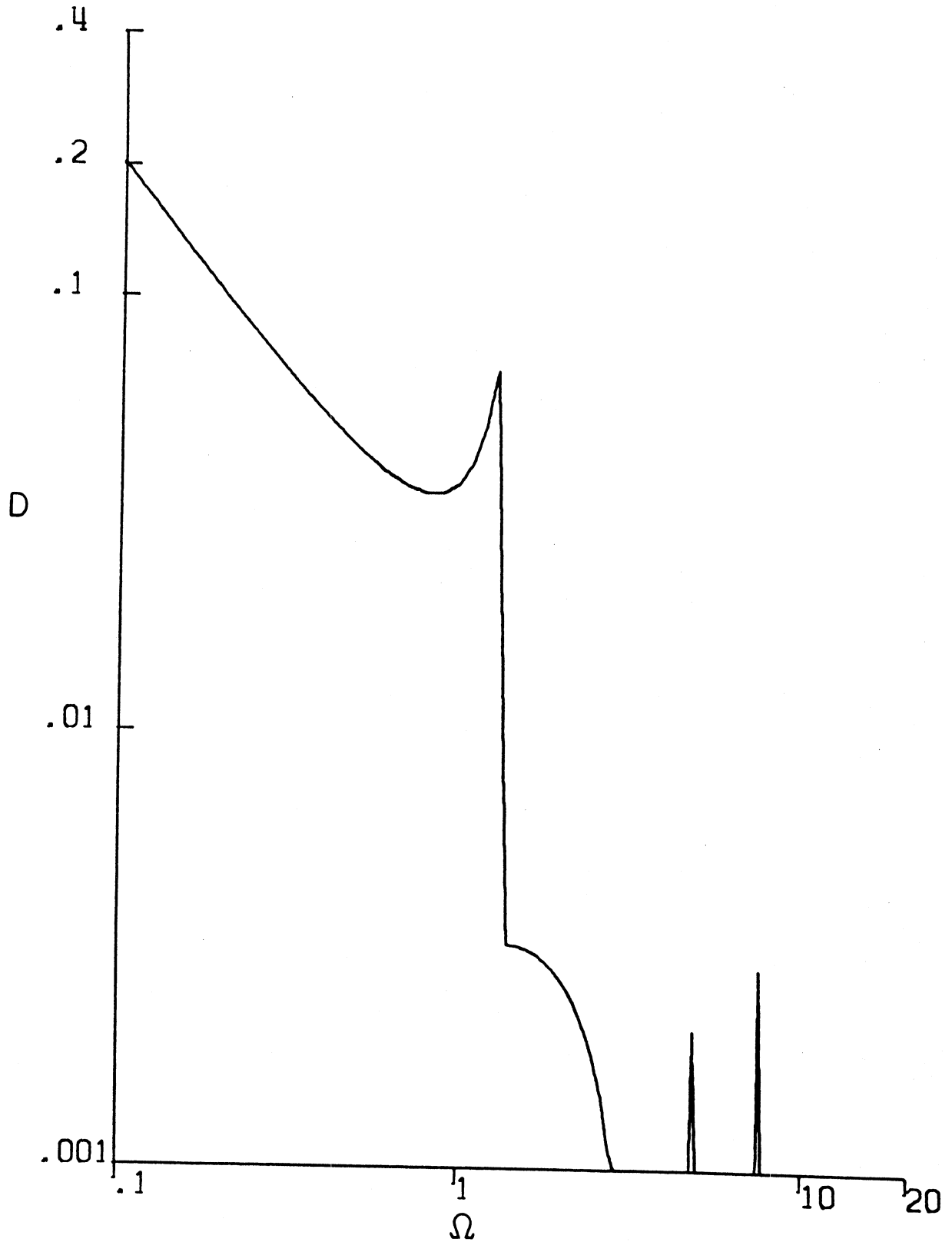
Figure 37. Locally Standing Waves -- Displacement Spectra for Two Layers and Shallow Source ($\beta_1 = \rho_1 = h_1 = h_2 = 1$, $\beta_2 = \rho_2 = 2$, $\xi = 0$, $\eta = 0.2$, $x = 2$, $z = 0$)
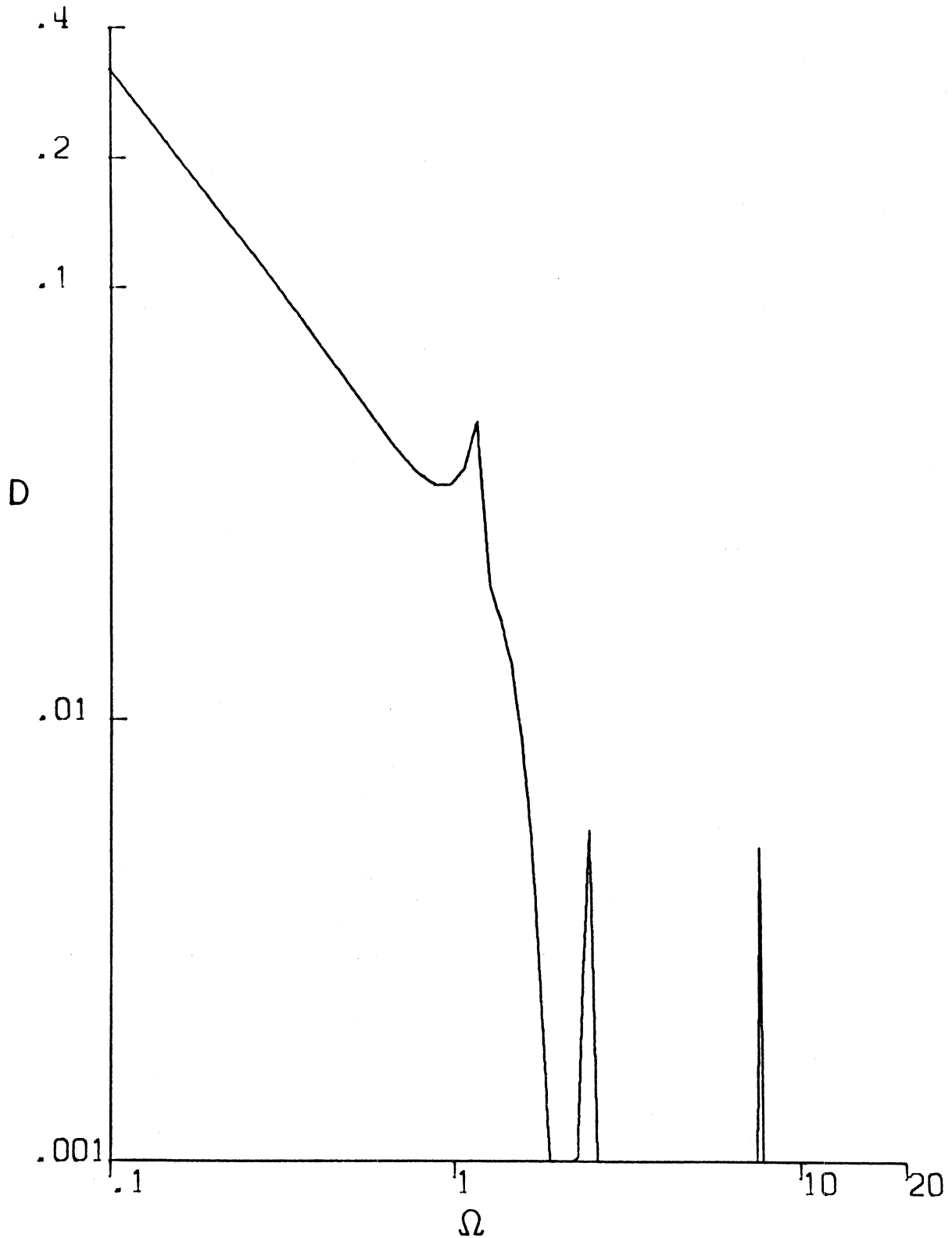
Figure 38. Locally Standing Waves -- Displacement Spectra for Three Layers and Shallow Source ($\beta_1 = \rho_1 = h_1 = h_2 = h_3 = 1$, $\beta_2 = \rho_2 = 2$, $\beta_3 = \rho_3 = 3$, $\xi = 0$, $\eta = 0.2$, $x = 2$, $z = 0$)

coefficients α_j shows they are frequency independent for each mode (progressive or locally standing). Therefore, energy density of each progressive mode in addition to being x-independent is also frequency independent. Energy density of locally standing modes is exponentially decreasing with increasing x. In e-ω space and for progressive modes the situation is depicted in Figure 39. Below the first cut-off frequency, no contribution to the energy density arises from the progressive modes. After the first cut-off frequency, only the first mode contributes; after the second cut-off frequency, the first two modes contribute, and so on. It is evident from Figure 39 that for shallow source, higher modes contribute less to the energy density compared to the lower progressive modes. For shallow source, the contribution of the second progressive mode to energy density is about 74.3% of the first mode contribution. Contributions of the third, fourth and fifth mode are 38.6%, 11.2% and 1.02%, respectively, of the first mode contribution. For deep source (dashed line) the contributions of second, third and fourth mode are 6.91, 8.54 and 4.54 times greater than the contribution to energy density of the first mode. The fifth mode contributes 49.3% of energy density of the first mode, for example. Therefore, as the source location changes from shallow to deep the maximum energy density contribution of single mode shifts from the first mode to higher modes.

The total energy density for a single layer model is shown in Figure 40. As indicated earlier, the total energy density consists of energy density due to progressive and locally standing modes. The former are presented by e=const planes in e-x-Ω space while the latter
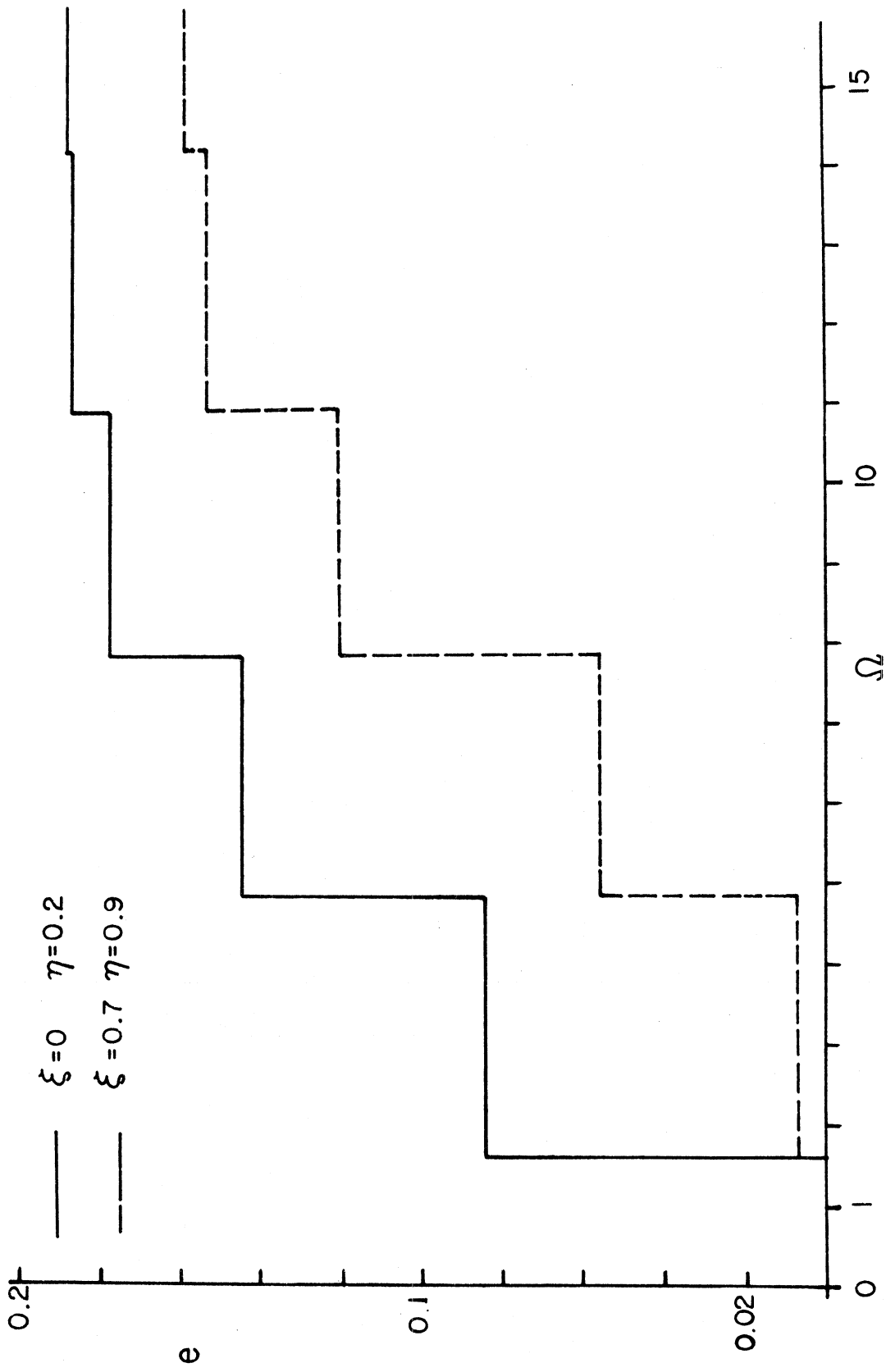
Figure 39. Single Layer Progressing Waves:
Energy Density for Shallow (Deep)
Source ($\beta_1 = \rho_1 = h_1 = 1$, $x = 2$, $z = 0$)
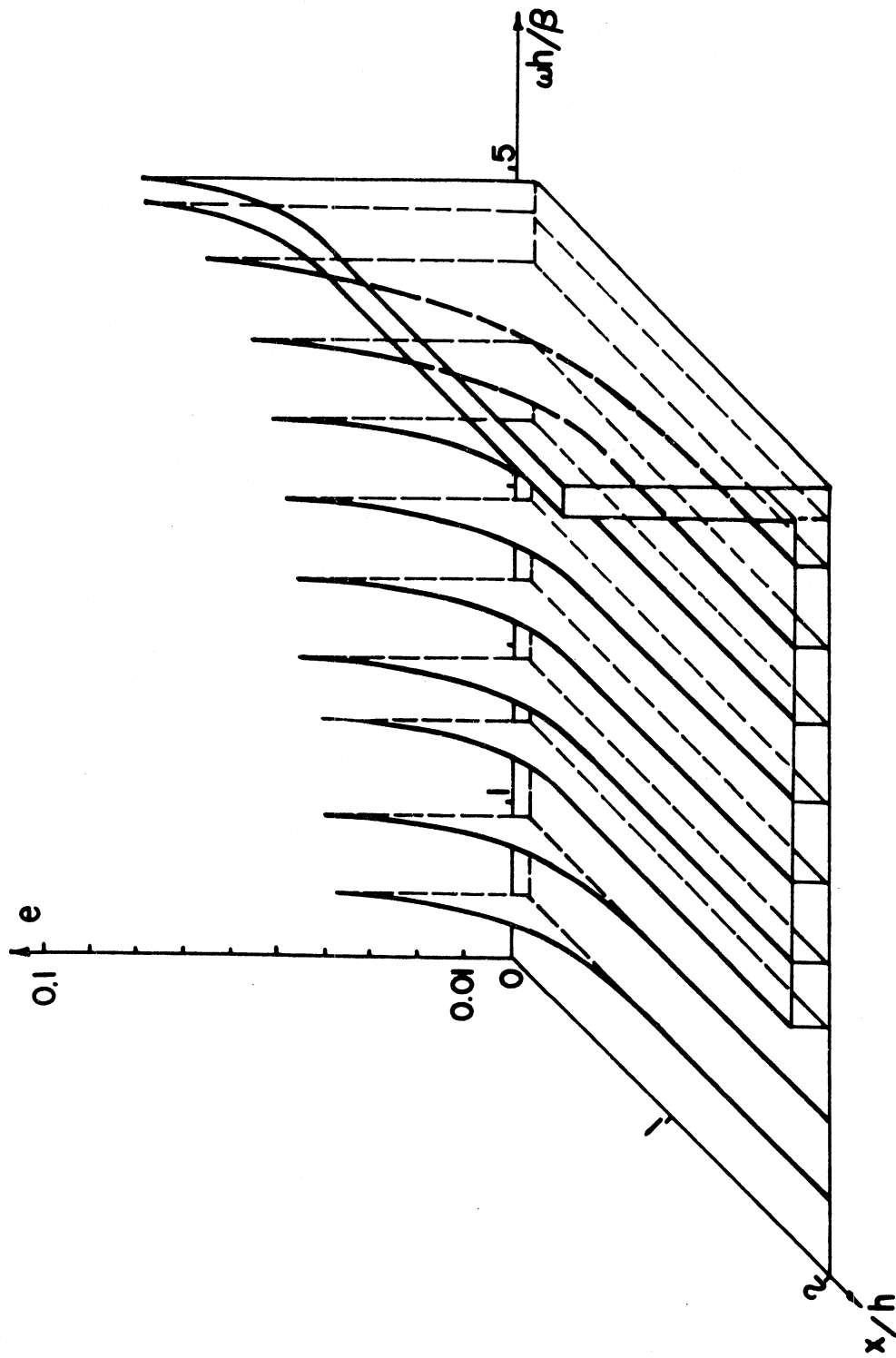
Figure 40. Energy Density for Single Layer and Deep Source
($\beta_1 = \rho_1 = h_1 = 1$, $\xi = 0.7$, $\eta = 0.9$, $z = 0$)

decrease with increasing x (only two cut-off frequencies are included in the frequency range shown in Figure 40).

In Figure 40, one finds the contribution of locally standing waves to the total energy density to be of importance up to distances x=0(h) only. For $x/h_1 > 1$ their contribution becomes negligible and energy density reduces to that of progressive waves only.

In the case of two layers, expansion coefficients α_j given by (2.12) are frequency dependent for each mode j while in the case of a single layer, they are frequency independent. The total energy density for a surface station in the two layer problem is shown in Figure 41. The results again indicate influence of locally standing waves for $x/h_1 < 1$. For $x/h_1 > 1$, their contribution to displacement amplitudes become negligible and energy density consists of progressive modes only.

2.6 Rotation Spectra
2.6.1 Progressing Waves

The z-component of the rotation spectra (1.58) is evaluated in a manner analogous to the displacement spectra. The results are illustrated by Figures 42 through 45. The rotation spectra for single layer case and for various depths of the source are shown by Figures 42 and 43 ($\rho_1 = 1$, $h_1 = 1$, $\beta_1 = 1$, $\xi = 0.2$, $v_0 = 1$, $a = 1$). The rotation spectra for two layers are illustrated in Figures 44 and 45 ($\rho_2 = 2$, $h_2 = 1$, $\beta_2 = 2$). It appears from these results that the two-layer model is more sensitive to the depth of the source relative to a single layer model. Similar situation was encountered for the displacement spectra (see (2.4)).
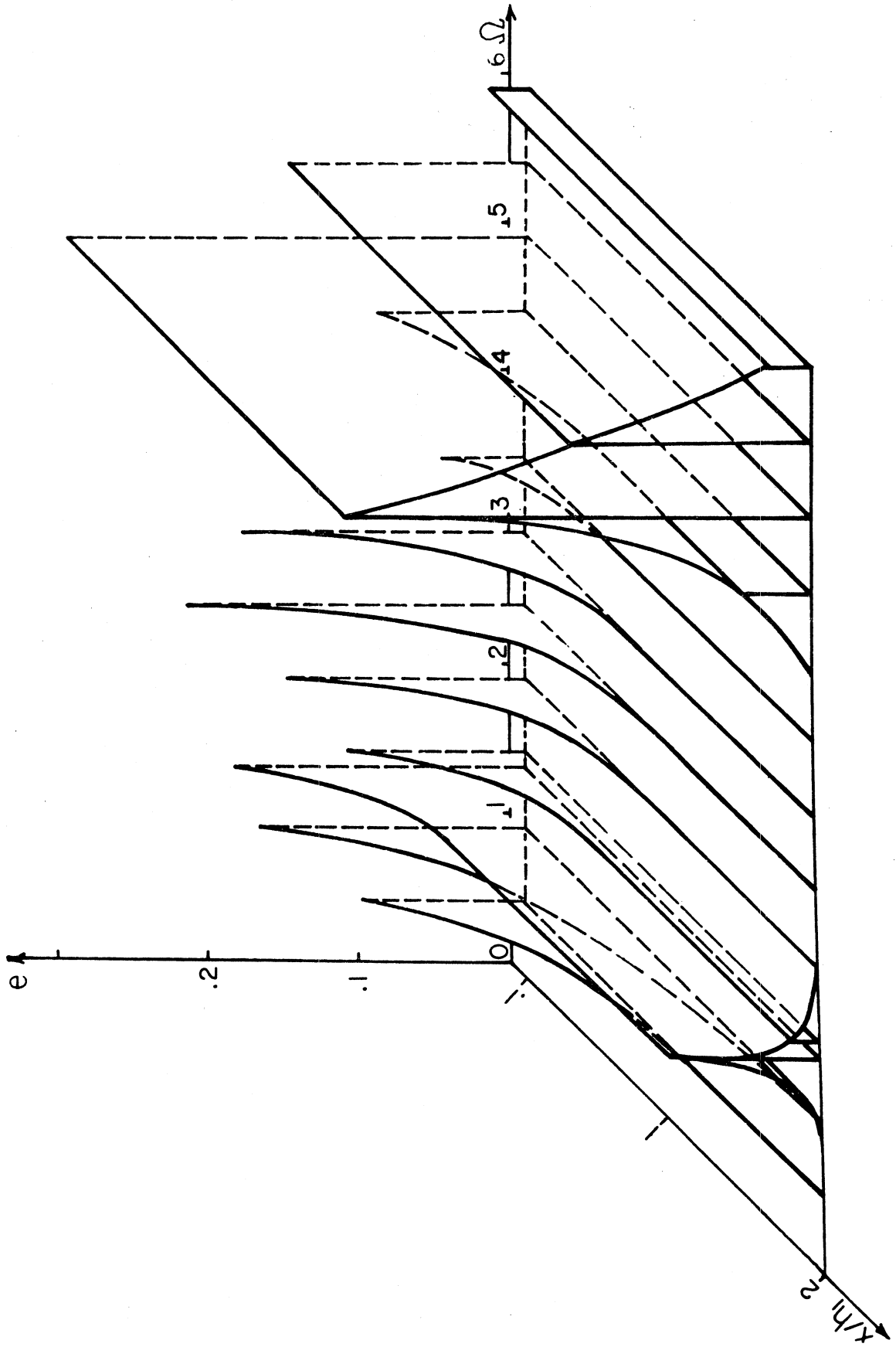
Figure 41. Energy Density for Two Layers and Deep Source
$(\beta_1 = \rho_1 = h_1 = h_2 = 1, \ \beta_2 = \rho_2 = 2, \ \xi = 0.7, \ \eta = 0.9, \ z = 0)$
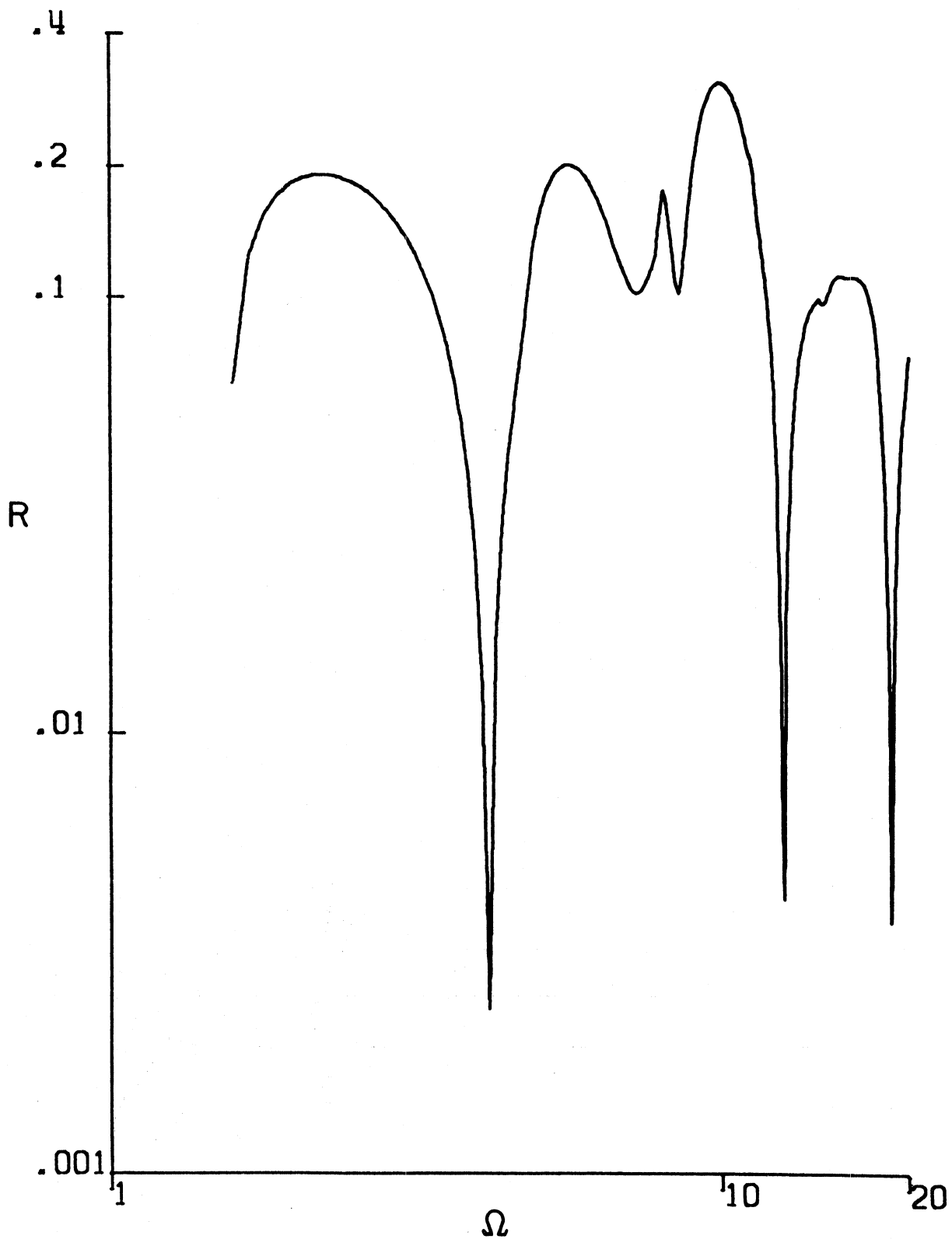
Figure 42.   Progressing Waves -- Single Layer Rotation Spectra for Shallow Source ($\beta_1 = \rho_1 = h_1 = 1$, $\xi = 0$, $\eta = 0.2$, $x = 2$, $z = 0$)
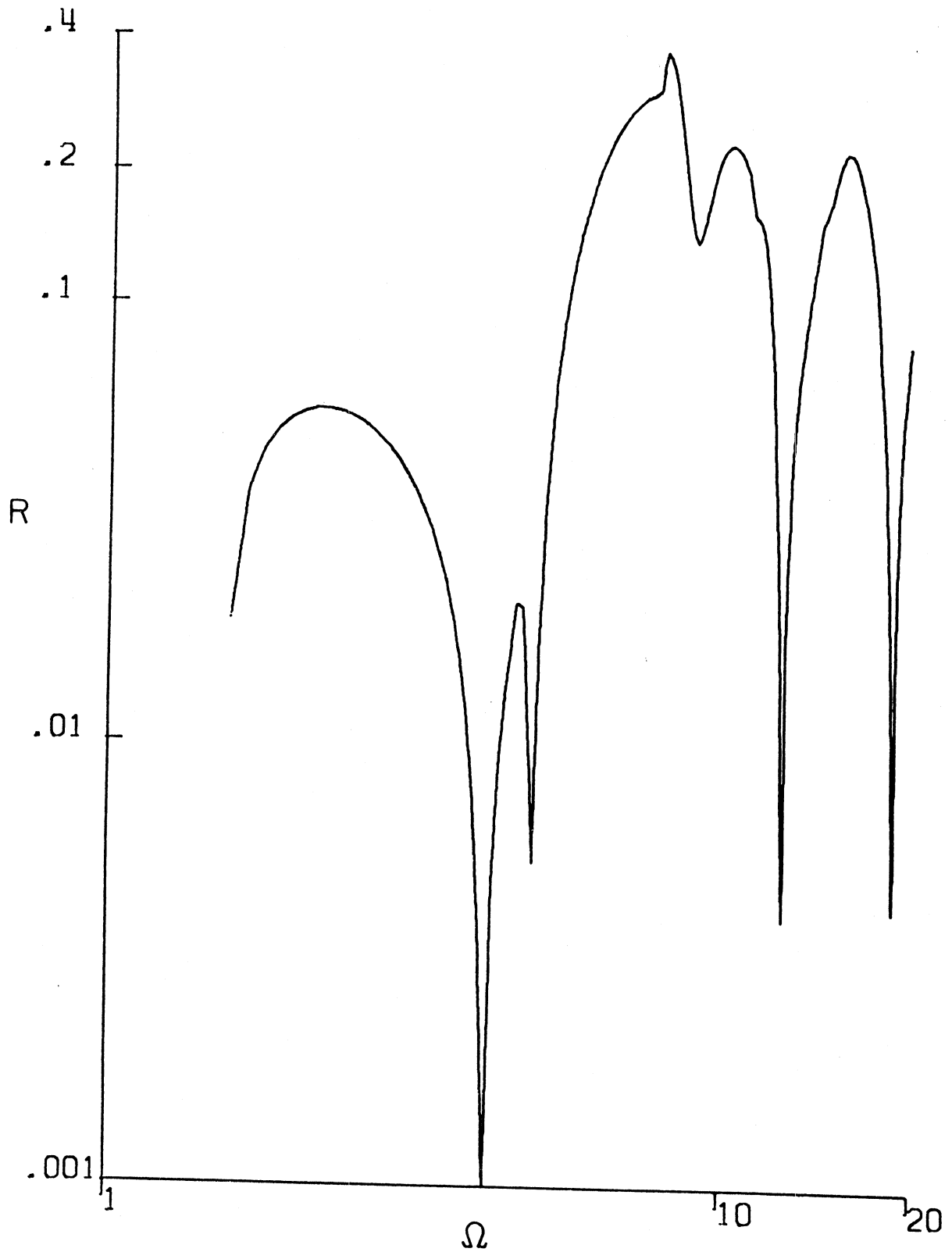
Figure 43.   Progressing Waves -- Single Layer Rotation Spectra for
             Deep Source ($\beta_1 = \rho_1 = h_1 = 1$, $\xi = 0.7$, $\eta = 0.9$, $x = 2$, $z = 0$)
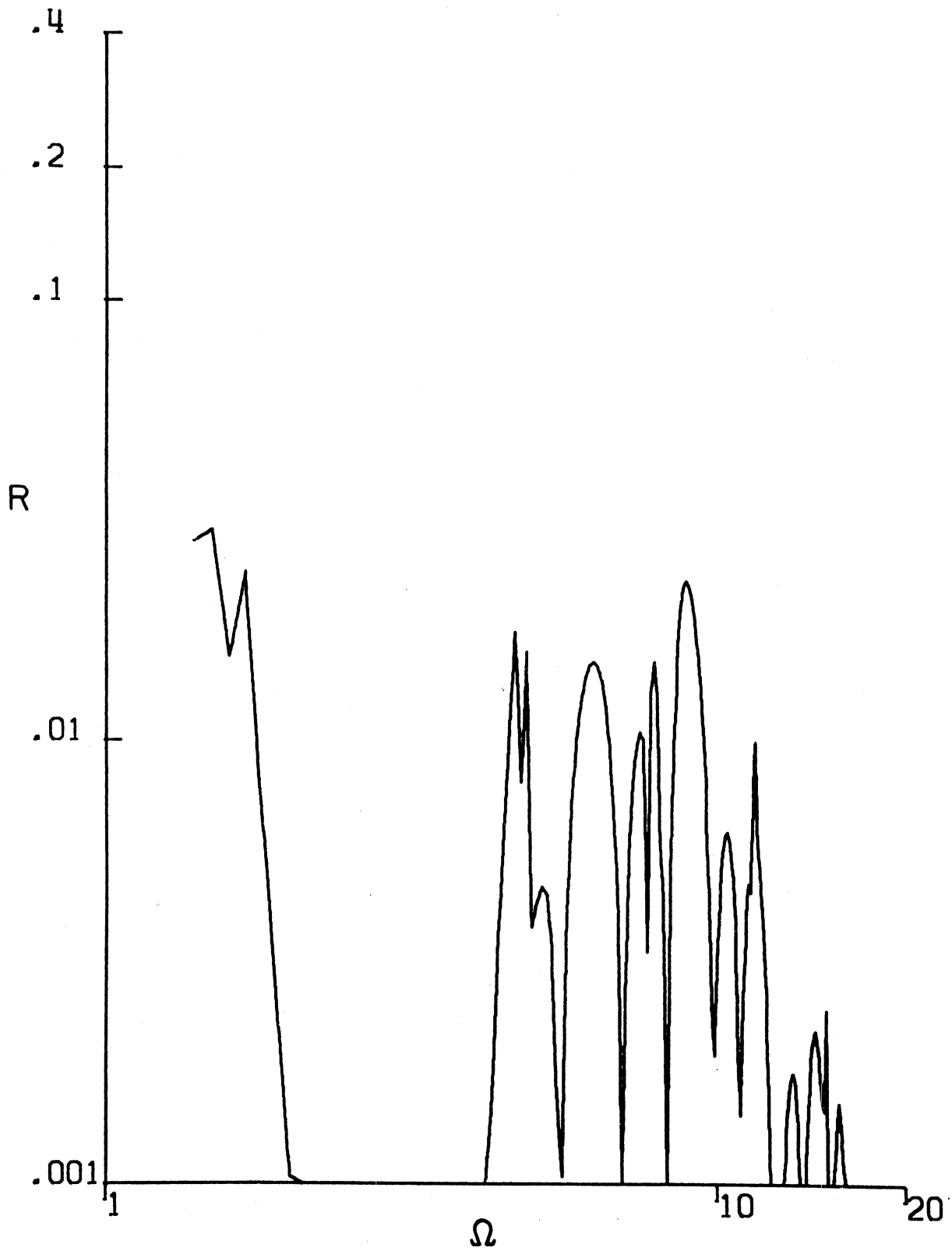
Figure 44. Progressing Waves -- Two Layers Rotation Spectra for Shallow Source ($\beta_1 = \rho_1 = h_1 = h_2 = 1$, $\beta_2 = \rho_2 = 2$, $x = 2$, $z = 0$, $\xi = 0$, $\eta = 0.2$)
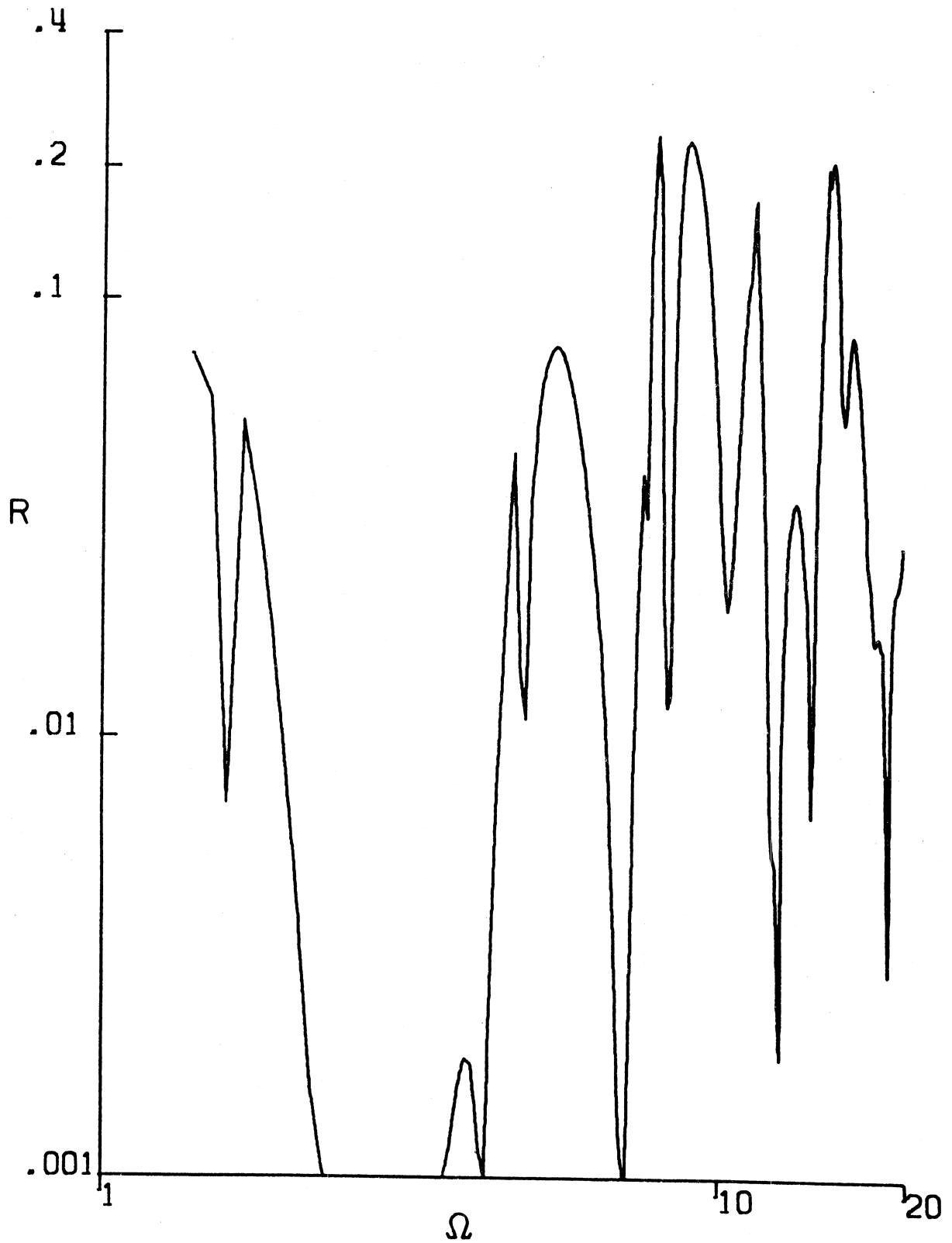
Figure 45. Progressing Waves -- Two Layers Rotation Spectra for Deep Source ($\beta_1 = \rho_1 = h_1 = h_2 = 1$, $\beta_2 = \rho_2 = 2$, $\xi = 0.7$, $\eta = 0.9$, $x = 2$, $z = 0$)

2.6.2 Locally Standing Waves

Examples of the rotation spectra due to locally standing waves for two and three layers are presented by Figures 46 through 49, respectively. These spectra have been evaluated for shallow and deep source to examine its influence upon the amplitudes of rotation spectra. By comparing these results, it follows that at higher frequencies, the three layer model is more sensitive to the depth of the source relative to the two layer model. Of course, on physical grounds, one expects in both cases that deep source excites higher frequency modes compared to the shallow source. This is in agreement with the results for displacement frequency spectra (see (2.4)).

2.7 Rotation Versus Displacement Spectra

It is of considerable engineering interest to establish whether there exists a simple relation between rotation and displacement spectra. A question often arises as to how to calculate the rotation spectra if the displacement spectrum is known.

For the case of a single layer, shallow source and progressive waves, the ratio of rotation versus displacement spectra (R/D) is shown in Figure 50. It can be seen that the ratio R/D increases with frequency. Division of this R/D by frequency Ω provides results presented in Figure 51.

Spectral ratios $R/D\Omega$ smoothed along the dimensionless frequency axis (Holloway, 1958) are shown in Figure 52 (see Appendix B for details of smoothing procedure). This figure includes results for two
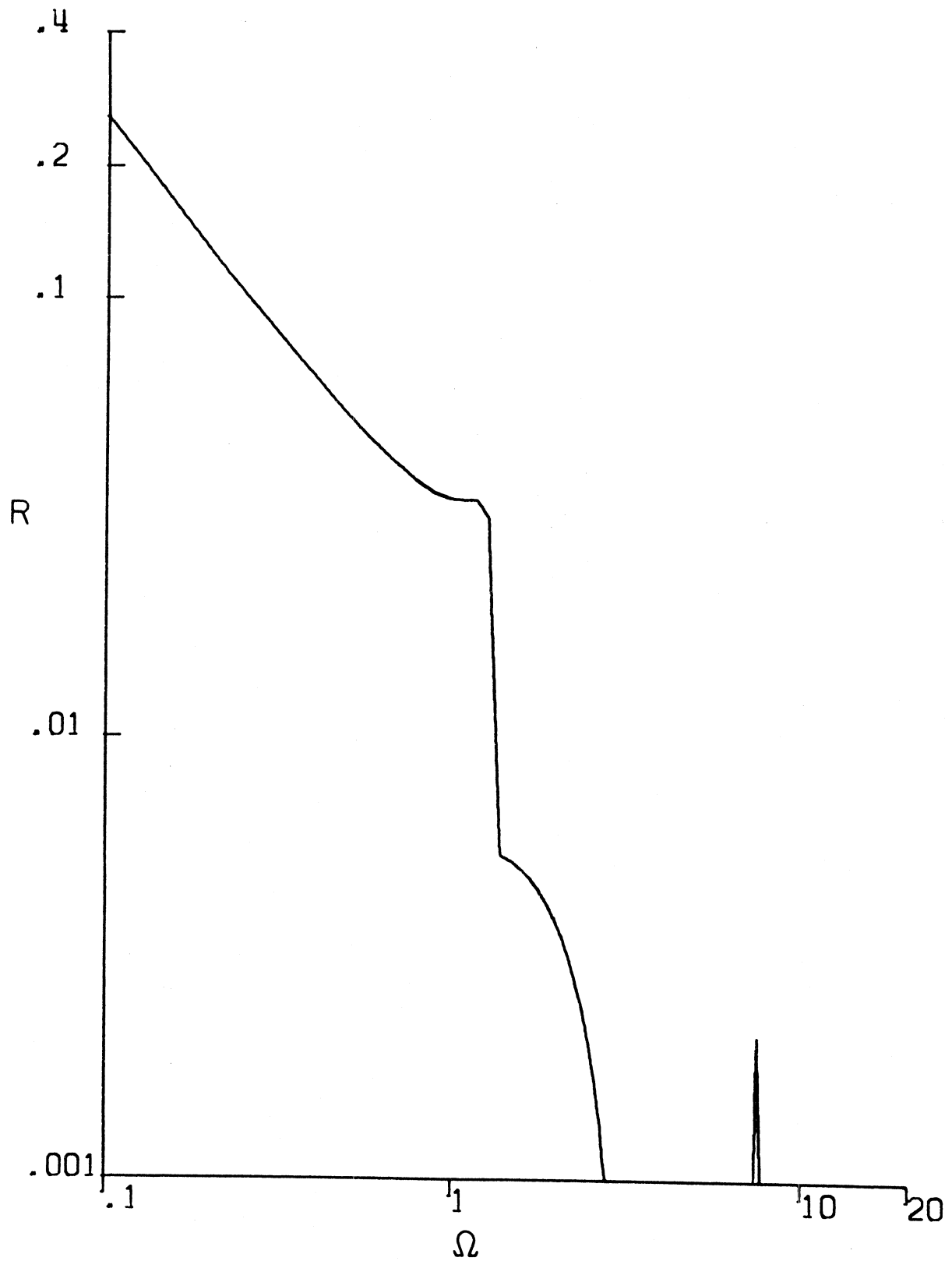
Figure 46. Locally Standing Waves -- Two Layers Rotation Spectra for Shallow Source ($\beta_1 = \rho_1 = h_1 = h_2 = 1$, $\beta_2 = \rho_2 = 2$, $\xi = 0.0$, $\eta = 0.2$, $x = 2$, $z = 0$)
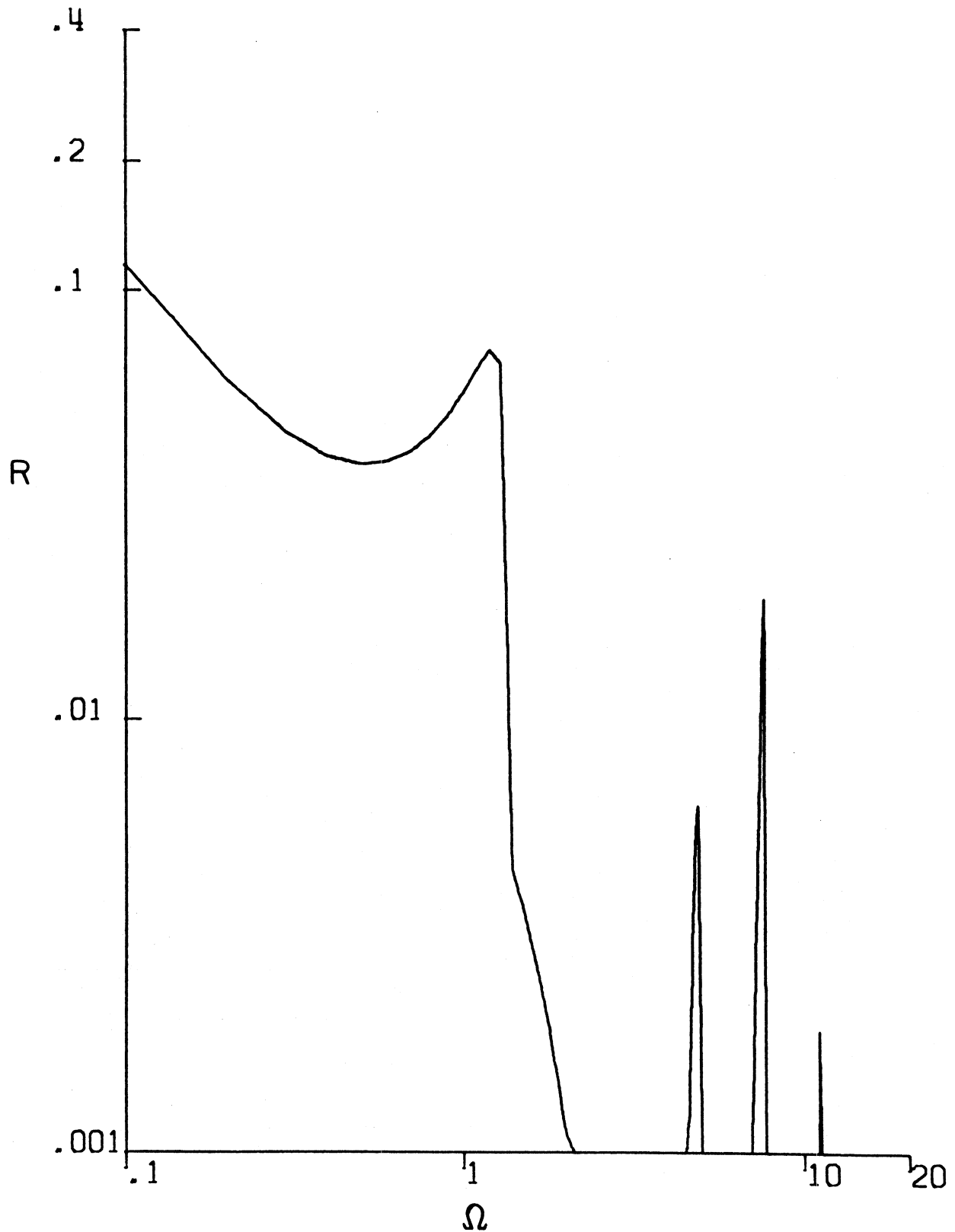
Figure 47.   Locally Standing Waves -- Two Layers Rotation Spectra for Deep Source ($\beta_1 = \rho_1 = h_1 = h_2 = 1$, $\beta_2 = \rho_2 = 2$, $\xi = 0.7$, $\eta = 0.9$, $x = 2$, $z = 0$)
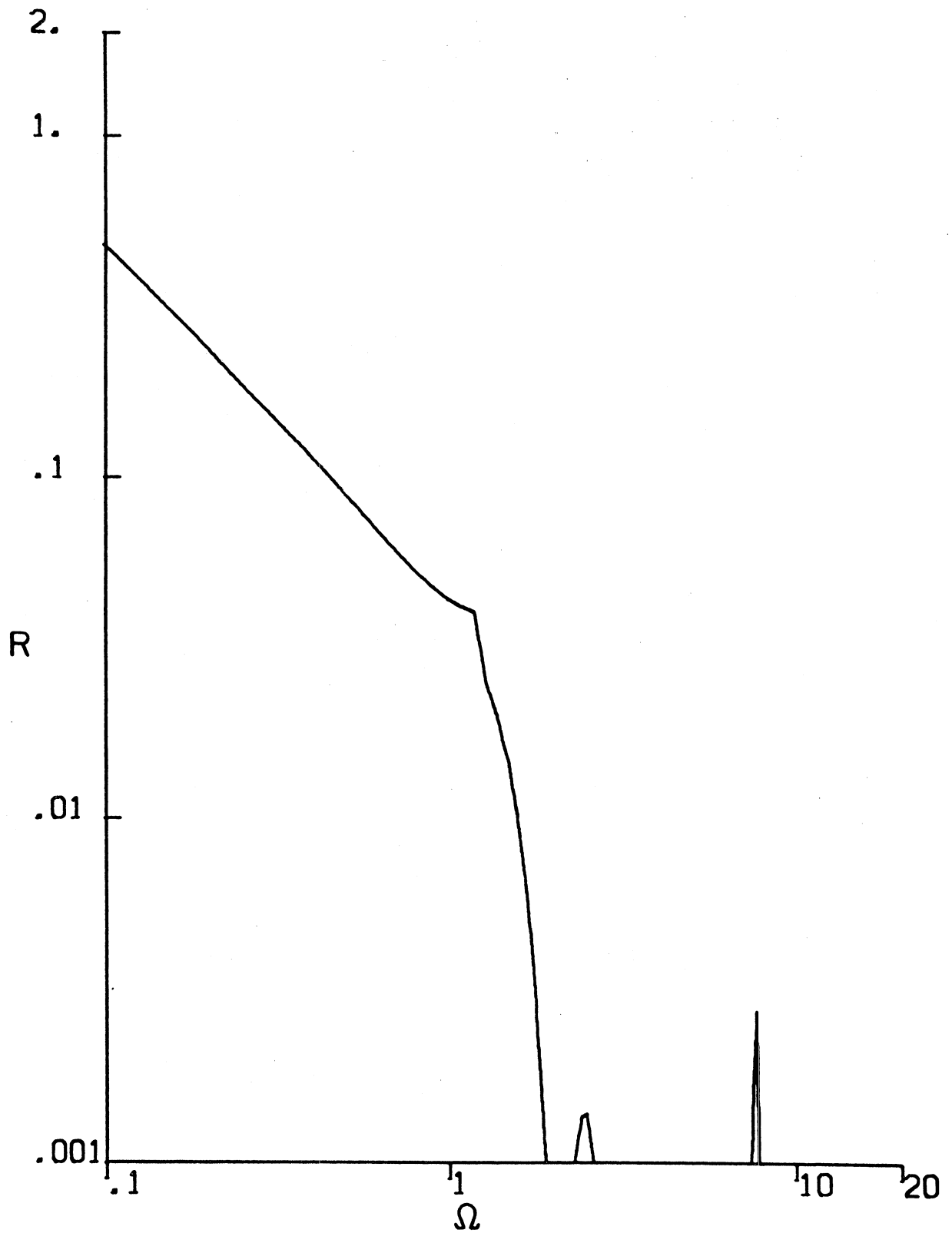
Figure 48. Locally Standing Waves -- Three Layers Rotation Spectra
for Shallow Source ($\beta_1 = \rho_1 = h_1 = h_2 = h_3 = 1$, $\beta_2 = \rho_2 = 2$,
$\beta_3 = \rho_3 = 3$, $\xi = 0$, $\eta = 0.2$, $x = 2$, $z = 0$)
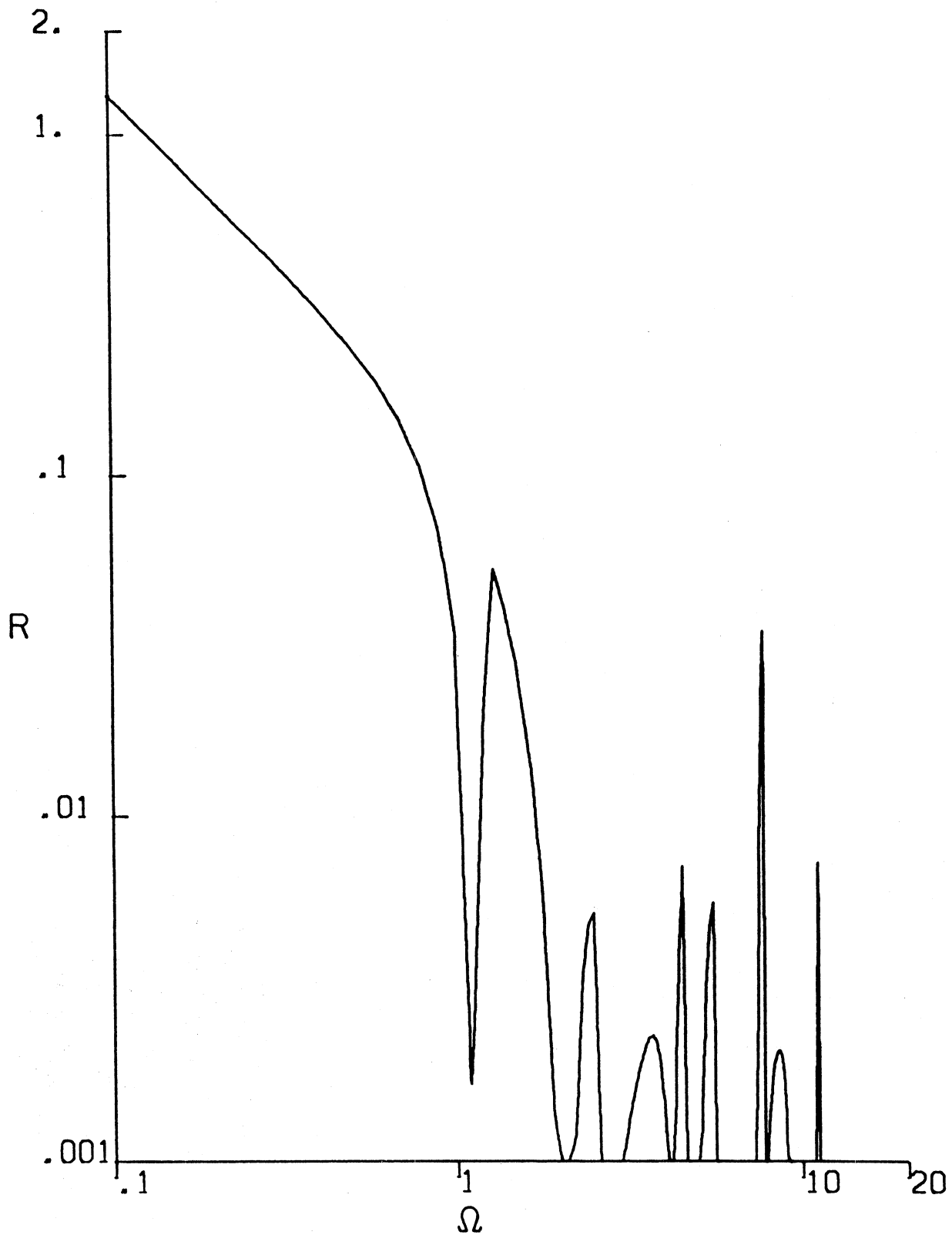
Figure 49.   Locally Standing Waves -- Three Layers Rotation Spectra for Deep Source ($\beta_1 = \rho_1 = h_1 = h_2 = h_3 = 1$, $\beta_2 = \rho_2 = 2$, $\beta_3 = \rho_3 = 3$, $\xi = 0.7$, $\eta = 0.9$, $x = 2$, $z = 0$)
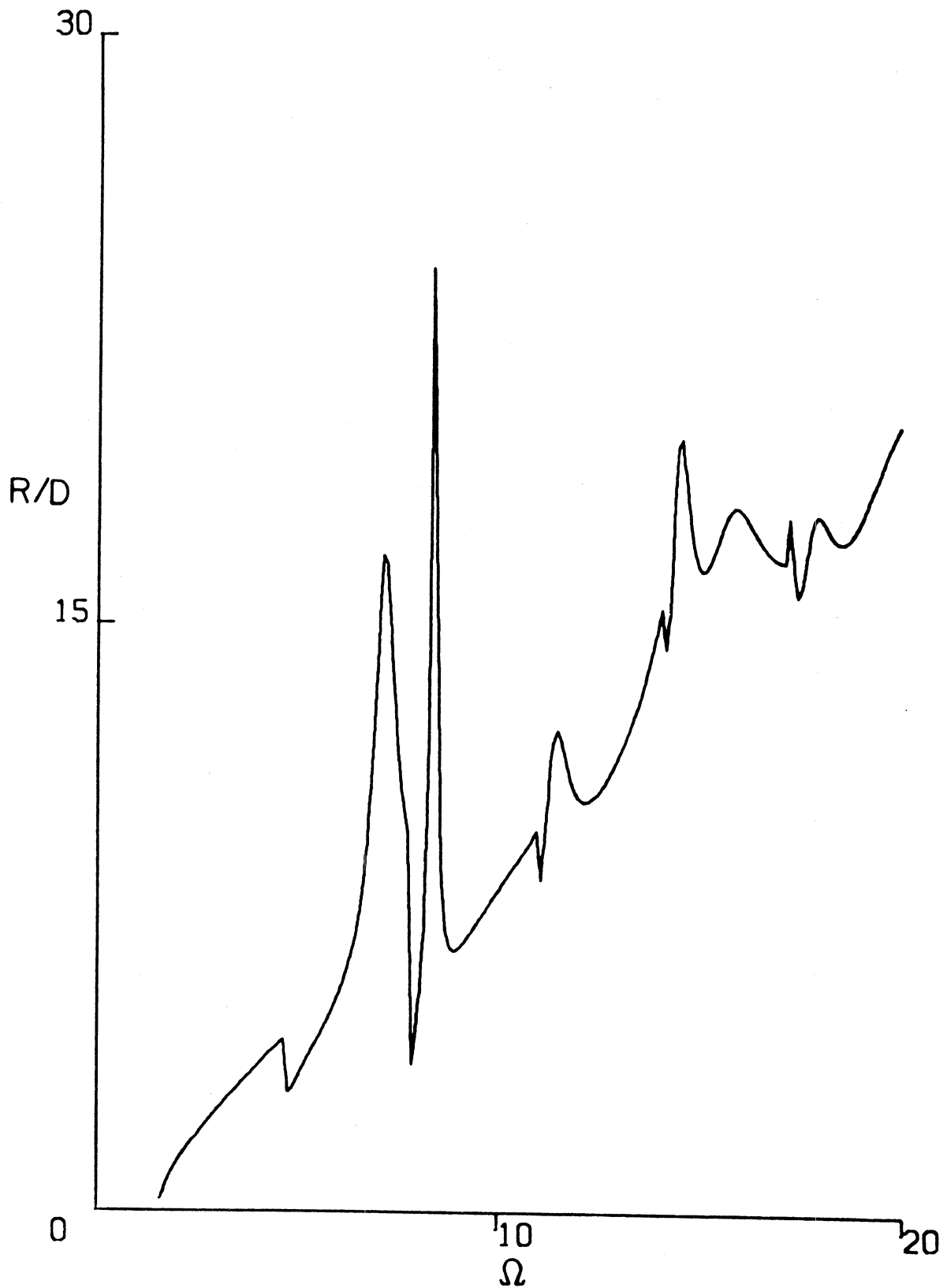
Figure 50. Progressing Waves -- Single Layer Ratio of Rotation vs. Displacement Spectra, Shallow Source ($\beta_1 = \rho_1 = h_1 = 1$, $\xi = 0$, $\eta = 0.2$, $x = 2$, $z = 0$)
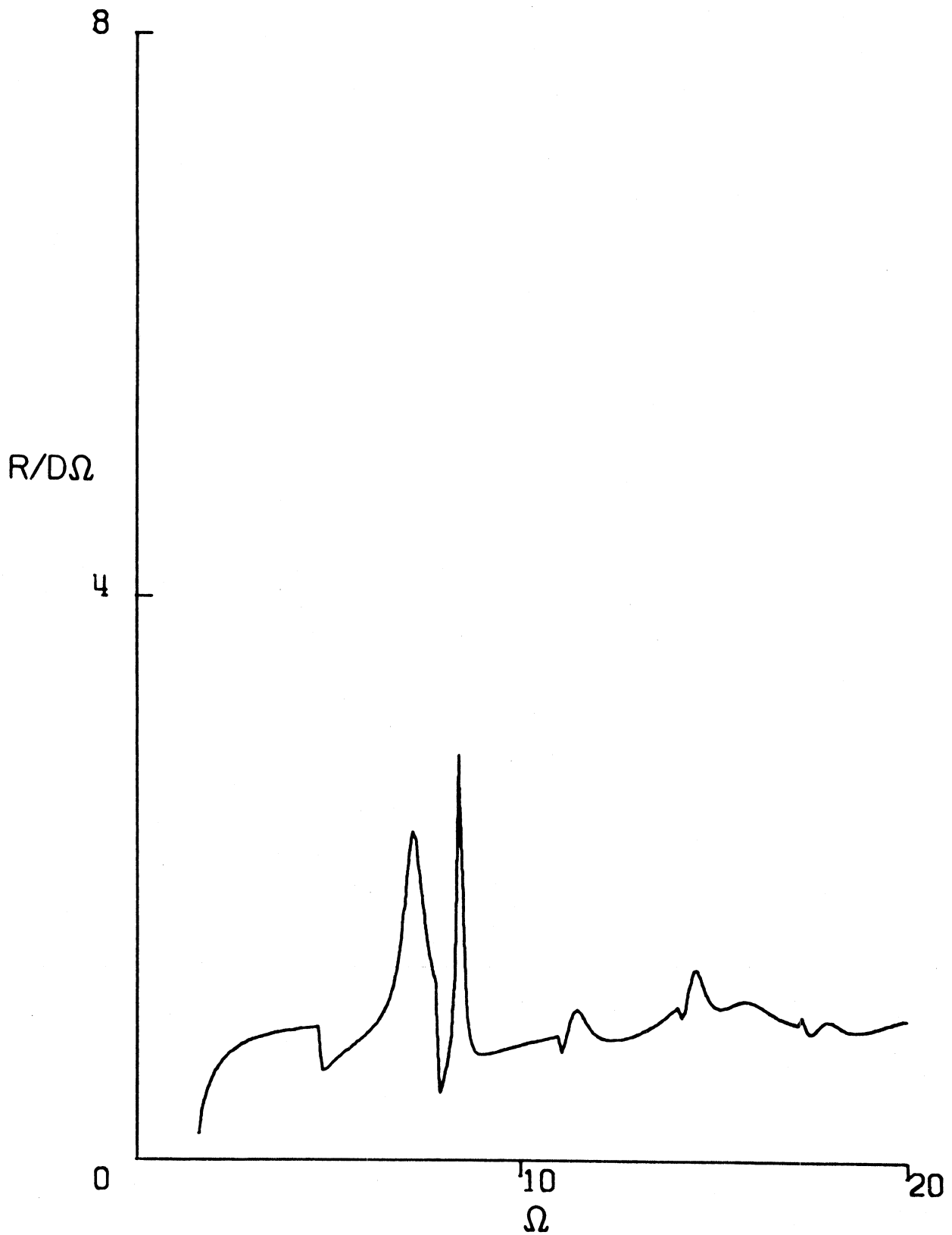
Figure 51.   Progressing Waves -- Single Layer: R/(DΩ), Shallow Source
($\beta_1 = \rho_1 = h_1 = 1$, $\xi = 0$, $\eta = 0.2$, $x = 2$, $z = 0$)
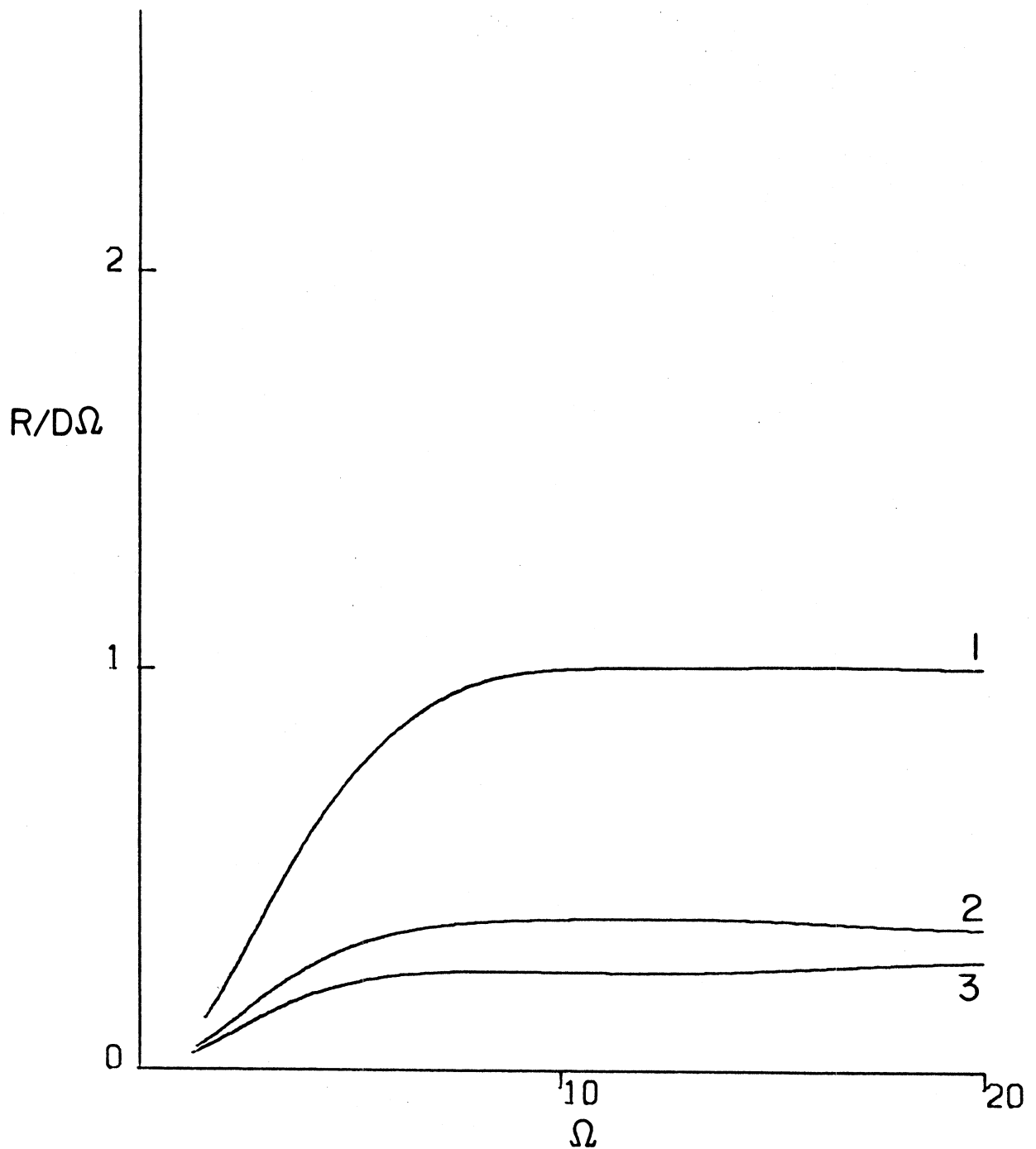
Figure 52. Progressing Waves -- Smoothed Ratio R/DΩ for Shallow Source
$\xi = 0$, $\eta = 0.2$, $x = 2$, $z = 0$: 1) Single Layer ($\beta_1 = \rho_1 = h_1 = 1$);
2) Two Layers ($\beta_1 = \rho_1 = h_1 = h_2 = 1$, $\beta_2 = \rho_2 = 2$); 3) Three
Layers ($\beta_1 = \rho_1 = h_1 = h_2 = h_3 = 1$, $\beta_2 = \rho_2 = 2$, $\beta_3 = \rho_3 = 3$)
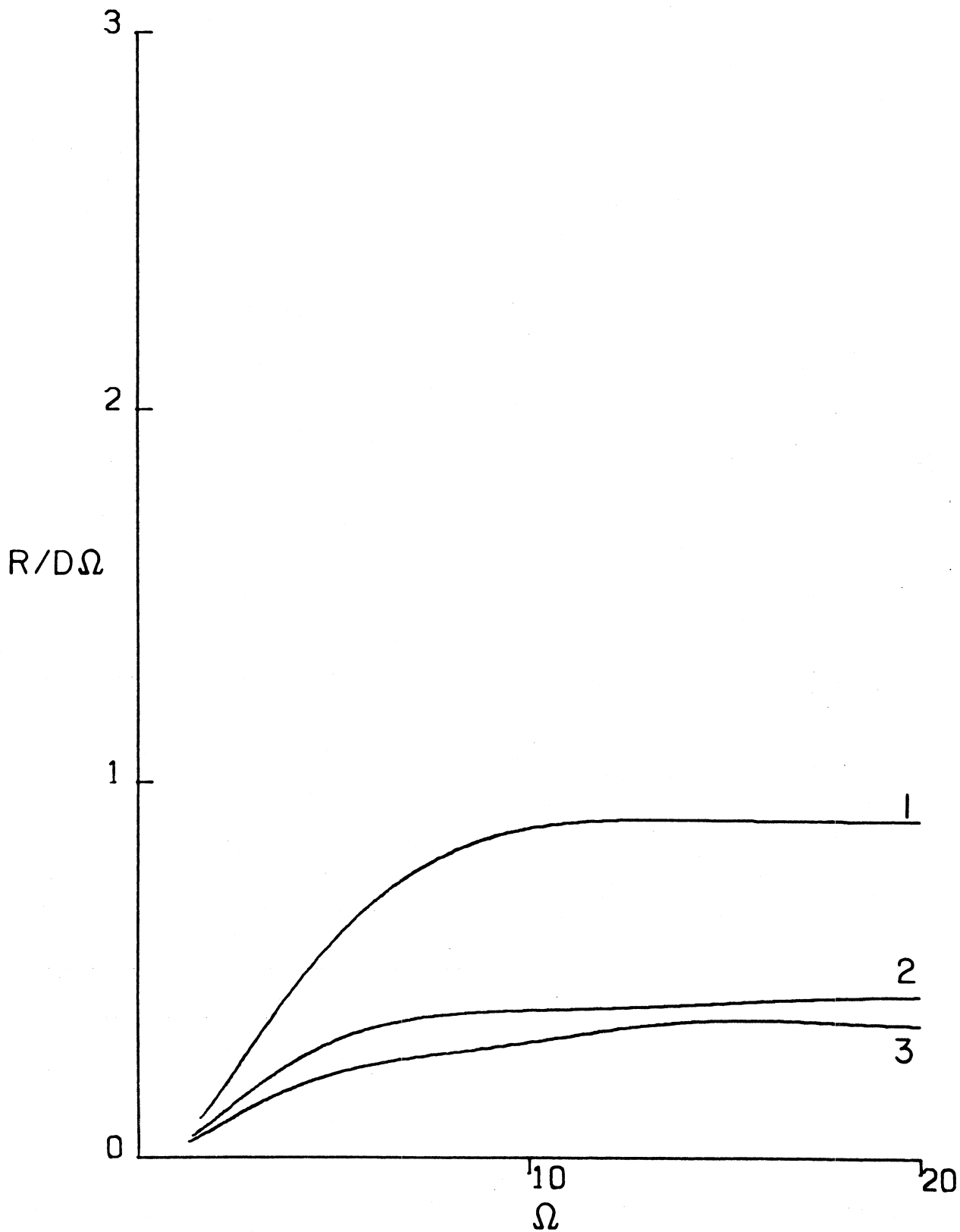
Figure 53.   Progressing Waves -- Smoothed Ratio $R/D\Omega$ for Deep Source
$\xi = 0.7$, $\eta = 0.9$, $x = 2$, $z = 0$: 1) Single Layer $(\beta_1 = \rho_1 = h_1 = 1)$;
2) Two Layers $(\beta_1 = \rho_1 = h_1 = h_2 = 1, \beta_2 = \rho_2 = 2)$; 3) Three
Layers $(\beta_1 = \rho_1 = h_1 = h_2 = h_3 = 1, \beta_2 = \rho_2 = 2, \beta_3 = \rho_3 = 3)$

and three layer models. It follows from Figure 52 that the ratio of smoothed $R/D\Omega$ spectra remains constant for a wide range of frequencies. The results for deep source, depicted by Figure 53 suggest small influence of depth of the source upon the smoothed $R/D\Omega$ amplitudes.

For shallow and deep sources and locally standing waves, the smoothed R/D spectra are presented in Figures 54 and 55.

2.8 Evaluation of the Response in Time Domain

The time response $v(x,z,t)$ is evaluated by application of the inverse Fourier transform to the frequency response $v(x,z,\omega)$ in (1.47)

$$v(x,z,t) = f(t) * \mathcal{G}_j(x,z,t) \quad . \tag{2.17}$$

In the above equation, $f(t)$ represents the input function (2.5), * denotes the convolution (Carrier, et. al., 1966), and $\mathcal{G}_j(x,z,t)$ is the inverse Fourier transform of the function defined by

$$G(z,x,\omega) = \sum_j \alpha_j(\omega)\phi_j(\omega,z)e^{ik_j x} \quad . \tag{2.18}$$

Since the function $G(x,z,\omega)$ is in general too complicated to invert in time domain in a closed form, the time response $v(x,z,t)$ is evaluated numerically by considering the integral

$$v(x,z,t) = \frac{1}{2\pi} \int_{-\infty}^{\infty} F(\omega)G(x,z,\omega)e^{i\omega t} \, d\omega \quad . \tag{2.19}$$

An outline of the numerical procedure is given in Appendix C.

2.8.1. Analysis of Results

For illustration of the time response $v(x,a,t)$ a case of a single layer is considered. The layer is assumed to have the shear wave
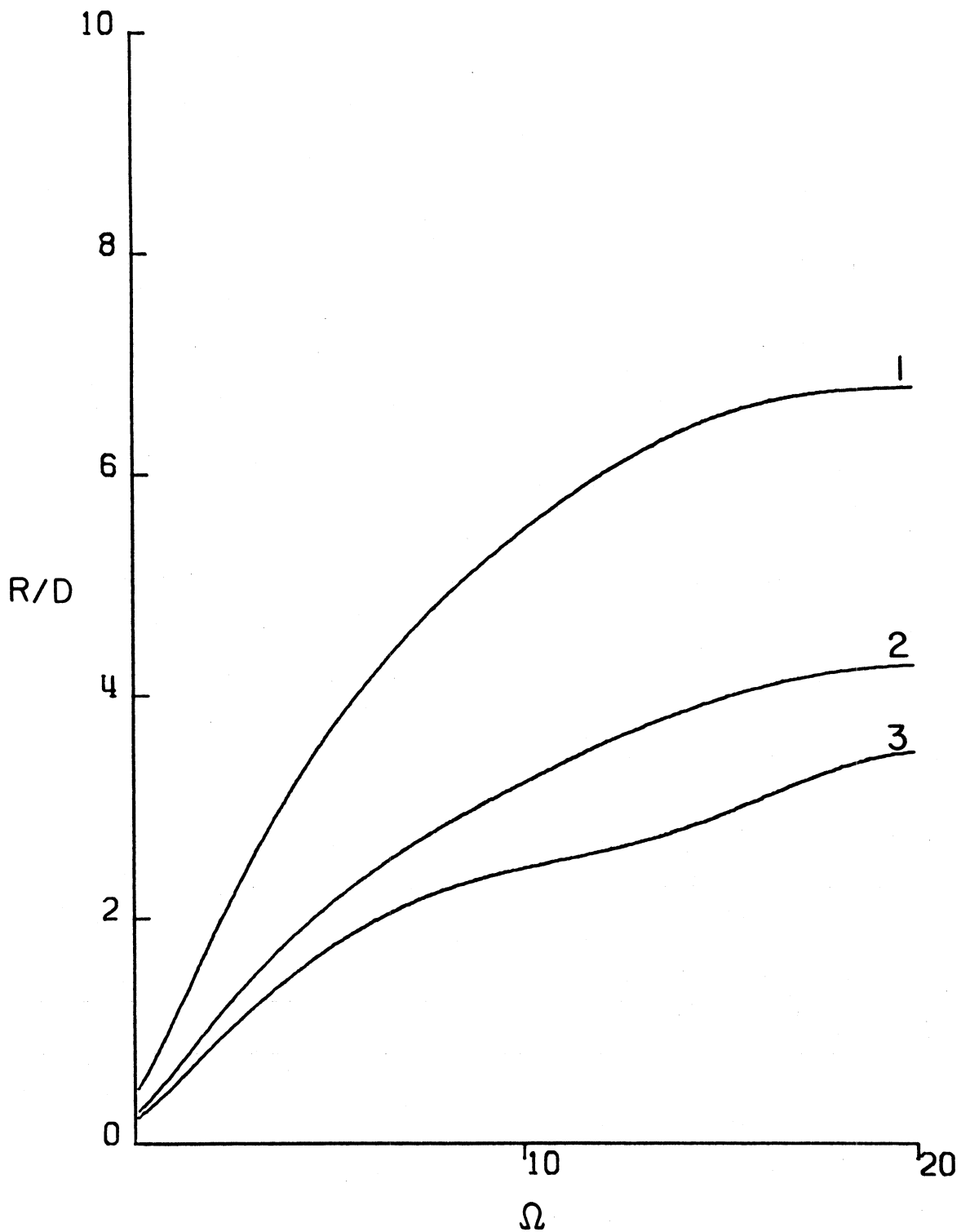
Figure 54. Locally Standing Waves -- Smoothed Ratio R/D for Shallow Source $\xi = 0.0$, $\eta = 0.2$, $x = 2$, $z = 0$: 1) Single Layer ($\beta_1 = \rho_1 = h_1 = 1$); 2) Two Layers ($\beta_1 = \rho_1 = h_1 = h_2 = 1$, $\beta_2 = \rho_2 = 2$); 3) Three Layers ($\beta_1 = \rho_1 = h_1 = h_2 = h_3 = 1$, $\beta_2 = \rho_2 = 2$, $\beta_3 = \rho_3 = 3$)
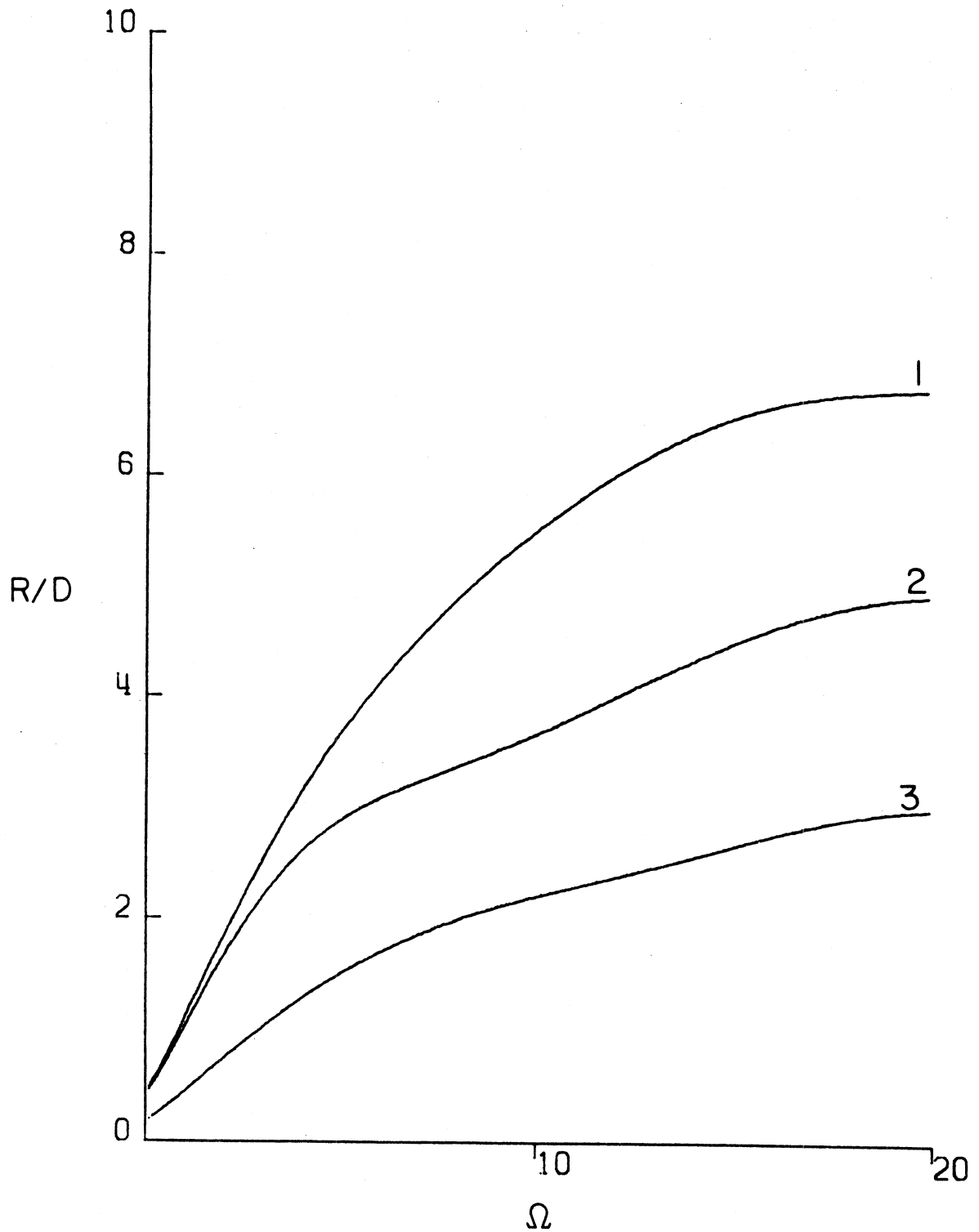
Figure 55. Locally Standing Waves -- Smoothed Ratio R/D for Deep
Source $\xi = 0.7$, $\eta = 0.9$, $x = 2$, $z = 0$: 1) Single Layer ($\beta_1 = \rho_1 = h_1 = 1$); 2) Two Layers ($\beta_1 = \rho_1 = h_1 = h_2 = 1$, $\beta_2 = \rho_2 = 2$);
3) Three Layers ($\beta_1 = \rho_1 = h_1 = h_2 = h_3 = 1$, $\beta_2 = \rho_2 = 2$, $\beta_3 = \rho_3 = 3$)

velocity β_1, density ρ_1, and thickness h_1, all equal to unity. The shallow source ($\xi = 0.0$, $\eta = 0.2$; see (2.3)) is considered first.

The difficulties arise if one attempts to work with the Fourier transform of (2.2) of the input field (2.1) since it has only the generalized Fourier transform, unbounded for $\omega = 0$ (see (2.6)). Since the response in layered medium is to be evaluated in some finite interval of time $(0, t^*)$ it is convenient to introduce an equivalent temporal input function $f_e(t)$ instead of $f(t)$. Denoting by $w(x,z,t)$ and $w_e(x,z,t)$ the time response in the layered medium due to input function $f(t)$ and $f_e(t)$, respectively, the criterion for constructing the equivalent function $f_e(t)$ is given by the requirement that $w_e(x,z,t) = w(x,z,ta_1)$ for $t \in [a_1, t^*]$. The parameters $a_1 \geq 0$ and t^* result from the construction of the $f_e(t)$. A choice of equivalent input field is presented by Figure C1 as an odd periodic function with period T. It is seen from Figure C1 that $f_e(t) = f(t)$ for $t \in [a_1, T/2]$. The parameter a_1 is chosen sufficiently large compared to T to ensure that the equivalent time response w_e is equal to the original response w for interval of time $t \in [a_1, t^*]$. Namely, the motion $w_e(x,z,t)$ starts initially from zero. From $t = a_1$ on, the motion is the same as $w(x,z,t-a_1)$ provided that a_1 is sufficiently large (see Figure C1) so the motions due to the remaining part of $f_e(t)$ do not reach the observation station x,z in the time interval (a_1, t^*).

For locally standing waves and the station $x = 0.5$, $z = 0.0$, results are presented by Figure 56. Of course, one has to take into account that actual response is represented by nonzero part in the
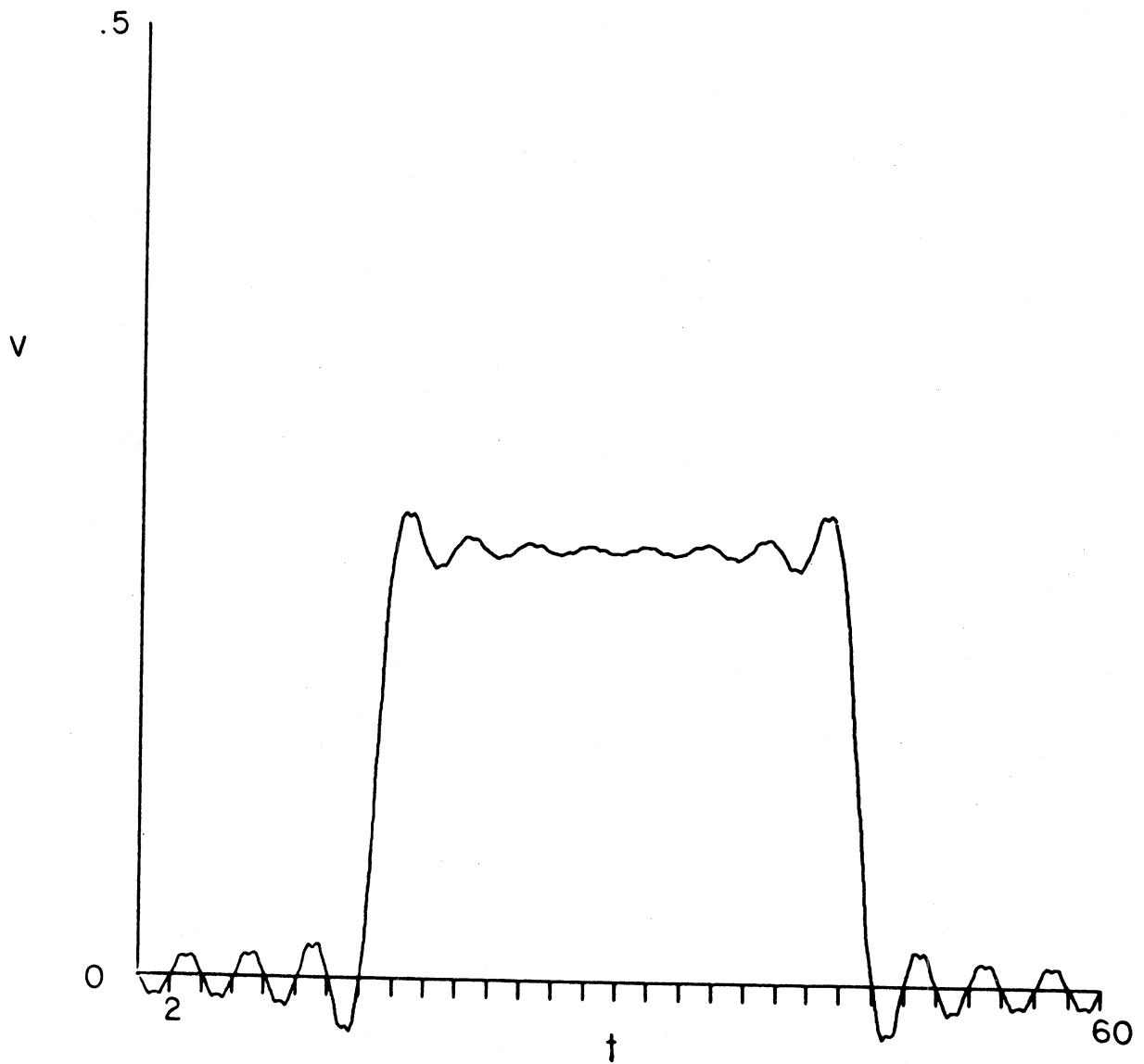
Figure 56. Locally Standing Waves -- Time Response for Single Layer
$v(0.5, 0.t)$--($\beta_1 = \rho_1 = h_1 = 1$, $\xi = 0$, $\eta = 0.2$, $x = 0.5$, $z = 0$)

region $t \le 30$ due to the property of application of the Fast Fourier Transform (Brigham, 1974). Thus, after initially being zero (see Appendix C) response reaches the long time limit (static solution) at which it remains. It can be seen that a relatively strong vibration is present in the response. This turns out to be due to waves (rays) which are perpendicular upon the surface of the layer. Namely, at cut-off frequencies $\Omega = (2j-1)\pi/2$, $j=1,2, \ldots$, the wave number which satisfies the frequency equation is equal to zero (Figure 2). As discussed in the evaluation of the frequency response, this corresponds to vertical rays which reflect back and forth from the faces of the layer. For $x \ne 0$ and $k_j = 0$, the term $e^{-k_j x}$ becomes one, which is relatively large compared to $e^{-k_j x}$ for a nonzero wave number, thus contributing significantly to the frequency response at the cut-off frequencies. The first two cut-off frequencies $\Omega = \pi/2$ and $3\pi/2$ correspond to the waves of periods $T = 4$ and $4/3$, respectively. The waves of the period $T = 4$ are clearly displayed for displacement field in Figure 56. Even the waves with period $T = 4/3$ can be seen; however, their contribution is insignificant compared to the former ones since the value of expansion coefficients α_j in (1.47) at the higher frequencies are small.

For the same station and progressing waves, the situation is presented in Figure 57. By superposition of the results for locally standing and progressing waves, the total wave field is given by Figure 58. Again, actual response is the nonzero part in $t \le 30$. As it can be seen from Figure 58, for a station close to the source,
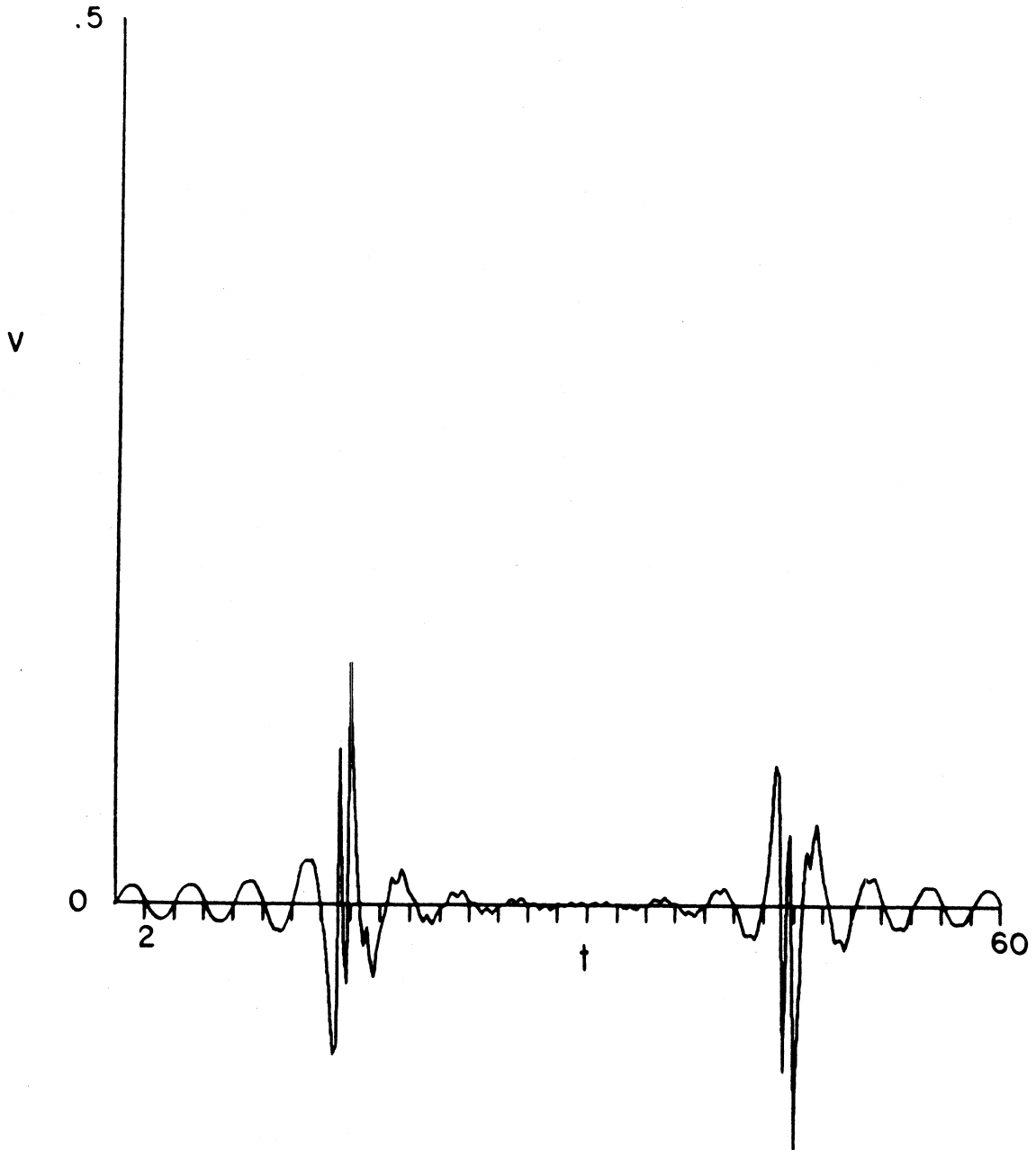
Figure 57.   Progressing Waves -- Time Response for Single Layer
v(0.5,0,t) -- ($\beta_1 = \rho_1 = h_1 = 1$, $\xi = 0$, $\eta = 0.2$, $x = 0.5$, $z = 0$)
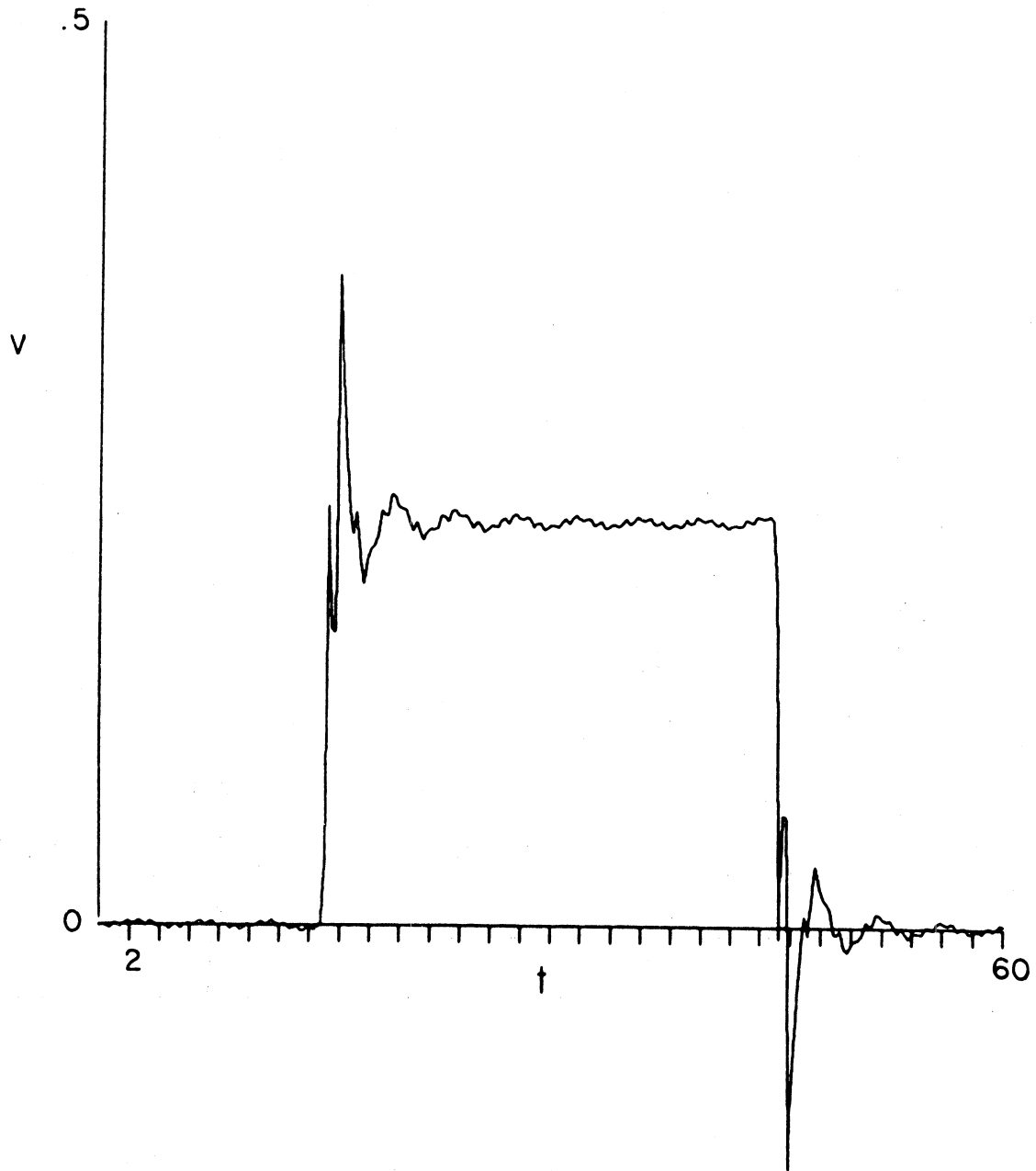
Figure 58. Time Response for Single Layer and Shallow Source $v(0.5, 0, t)$
($\beta_1 = \rho_1 = h_1 = 1$, $\xi = 0$, $\eta = 0.2$, $x = 0.5$, $z = 0$)

contribution of locally standing waves is significant compared to the contribution of progressing waves. For stations $z = 0$ and $x = 1$, 1.5 and 2, the total wave fields for shallow source are shown by Figures 59 through 61. As the distance from the source increases, the influence of locally standing waves diminishes. This is illustrated in Figure 62 by the amplitude of the long time limit displacement due to locally standing waves, A_s, and the maximum amplitude of total displacement field, A_d. For example, at distances of one thickness of the layer from the source amplitude due to locally standing waves accounts for about 38% of the maximum amplitude for shallow source and about 21% for deep source. For source distance $x = 2$, this contribution is 14% and 7%, respectively.

The results in Figure 62 illustrate the influence of the locally standing waves in total wave field compared to the progressing waves. For distances from the source greater than two thicknesses of the layer, the displacement due to locally standing waves can be neglected. However, within the distance from the source which is less than the thicknesses of the layer, the locally standing waves contribute significantly to the displacement field and cannot be ignored. These results imply that for structures in immediate vicinity of a fault, the contribution of locally standing waves must be incorporated in safety analysis of the structures. Failure to do so might result in unsafe design by increasing the risk to damage of the structures in the event of an earthquake.
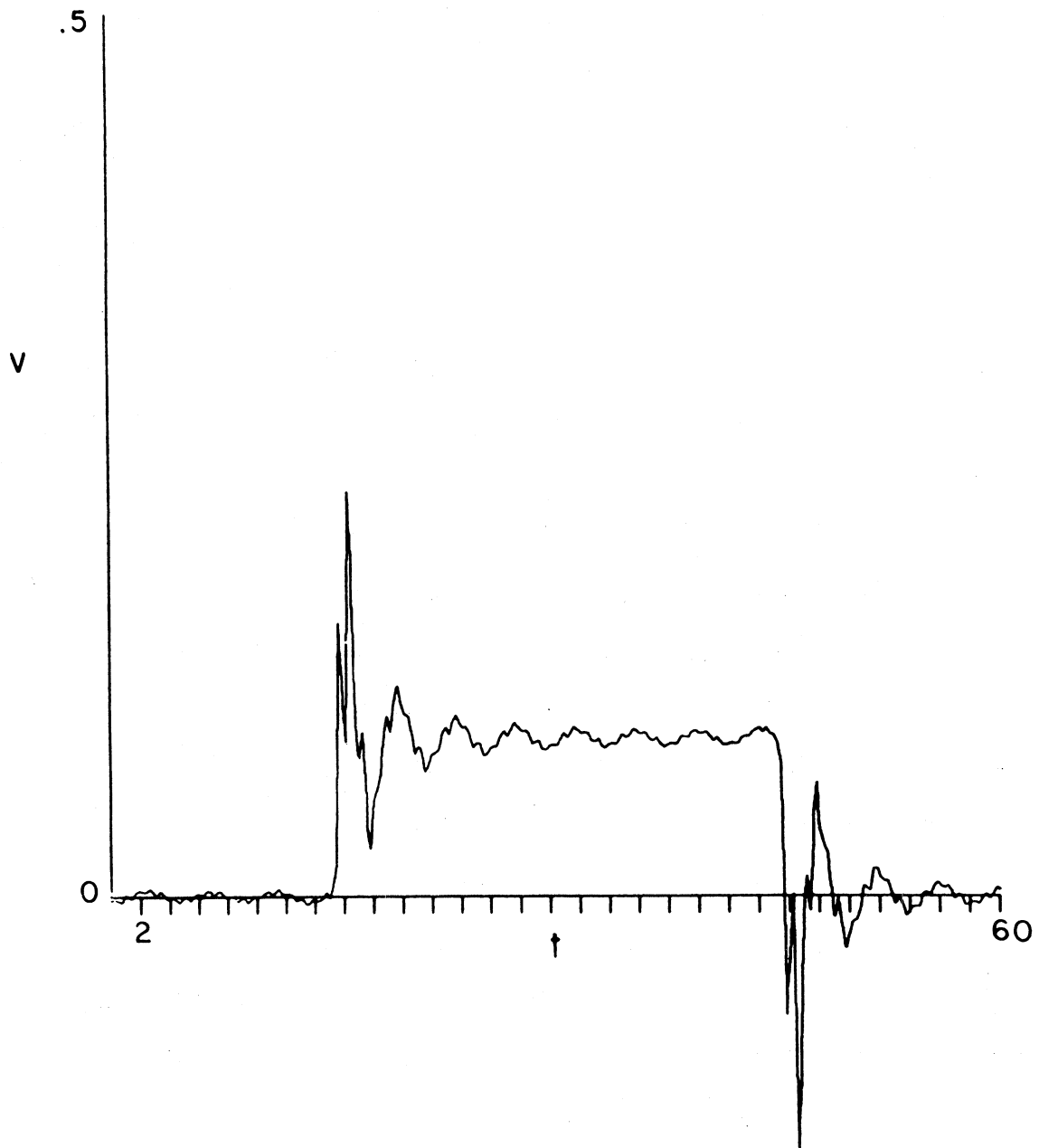
Figure 59. Time Response for Single Layer and Shallow Source $v(1.0,0,t)$
($\beta_1 = \rho_1 = h_1 = 1$, $\xi = 0$, $\eta = 0.2$, $x = 1$, $z = 0$)
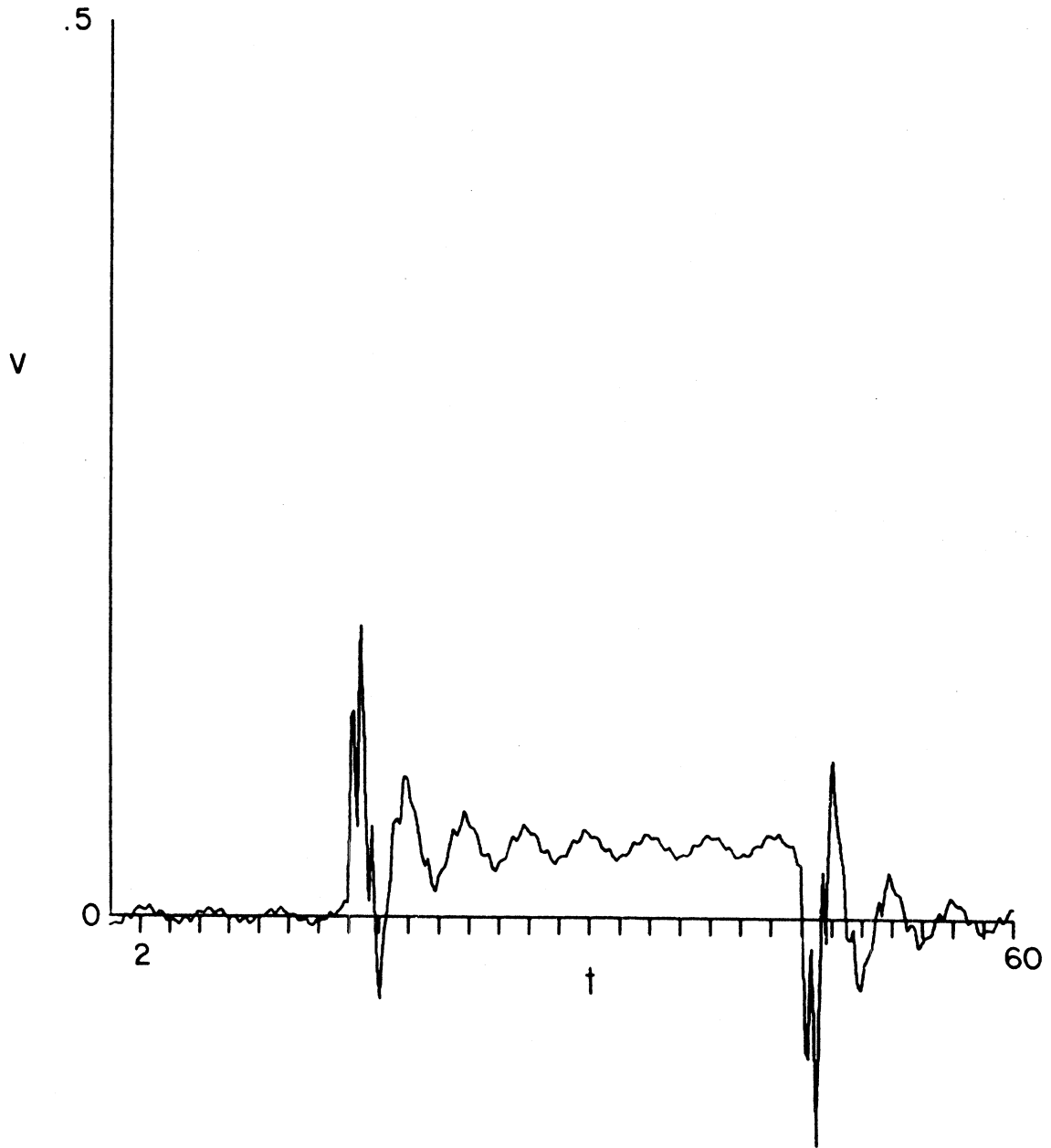
Figure 60. Time Response for Single Layer and Shallow Source $v(1.5,0,t)$
$(\beta_1 = \rho_1 = h_1 = 1,\ \xi = 0,\ \eta = 0.2,\ x = 1.5,\ z = 0)$
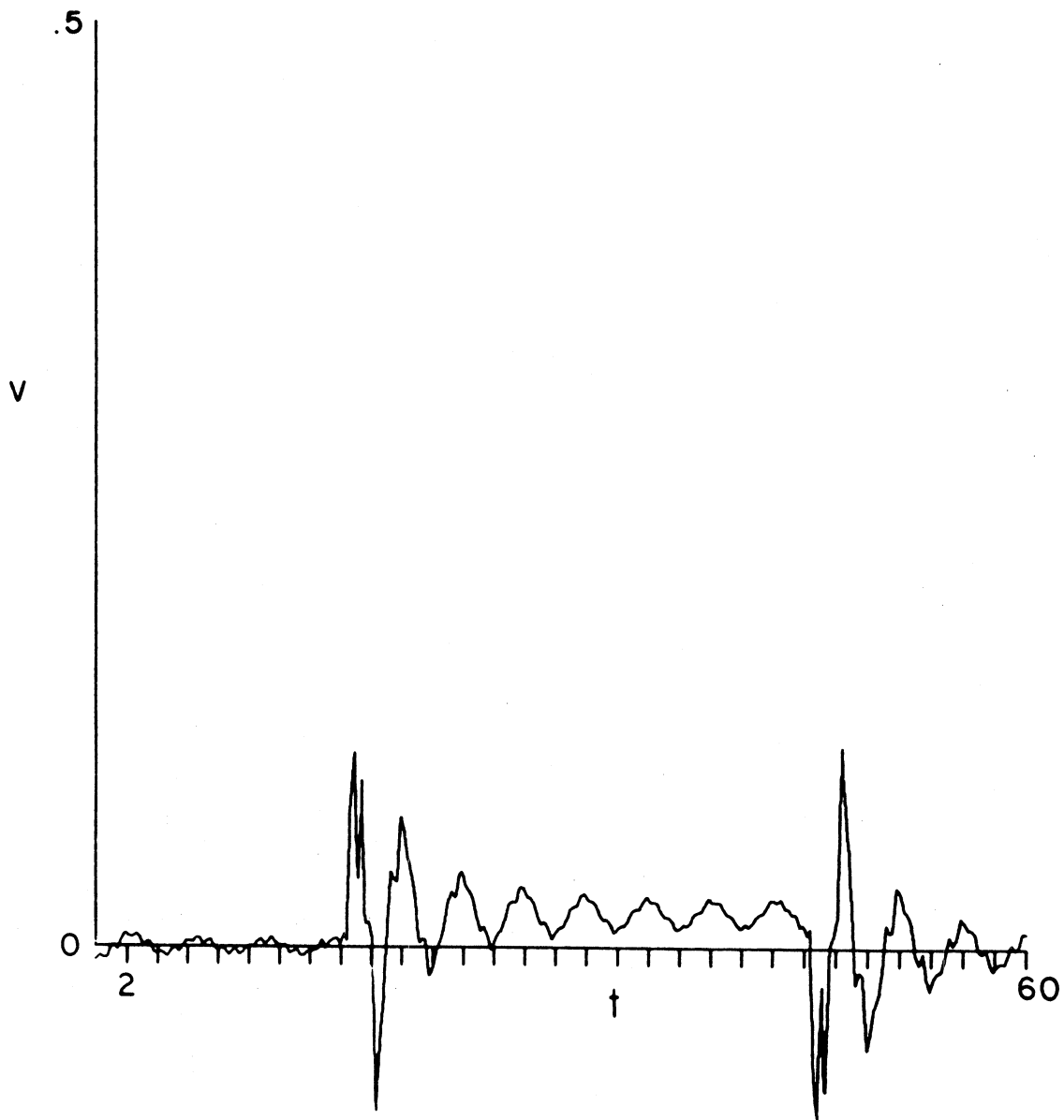
Figure 61. Time Response for Single Layer and Shallow Source $v(2,0,t)$
($\beta_1 = \rho_1 = h_1 = 1$, $\xi = 0$, $\eta = 0.2$, $x = 2$, $z = 0$)
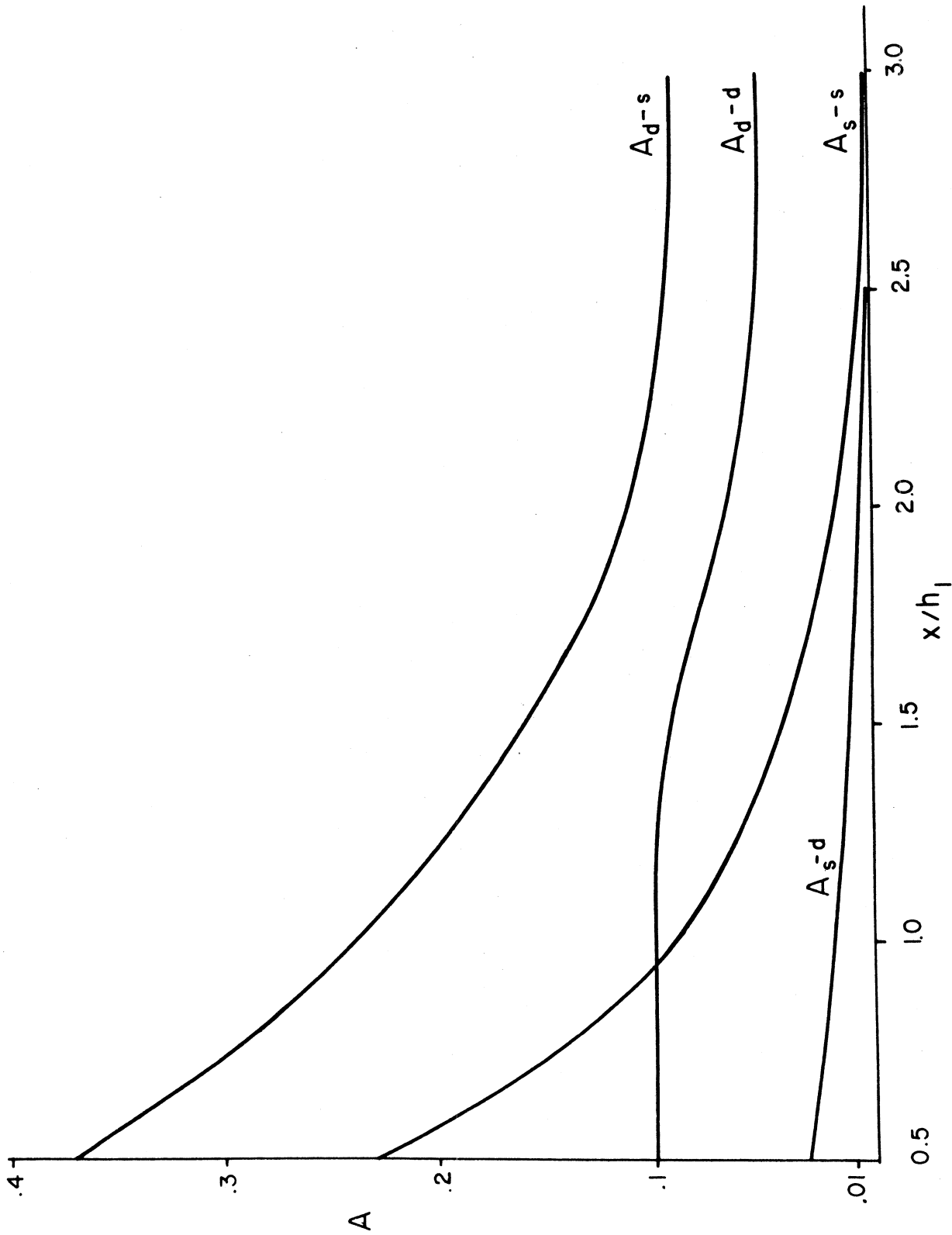
Figure 62. Maximum Amplitude of Time Responses for Single Layer ($\beta_1 = \rho_1 = h_1 = 1$, $z = 0$) A_d-s Total Wave Field, Shallow Source $\xi = 0$, $\eta = 0.2$; A_d-d Total Wave Field, Deep Source $\xi = 0.7$, $\eta = 0.9$; A_s-s Locally Standing Waves, Shallow Source $\xi = 0$, $\eta = 0.2$; A_s-d Locally Standing Waves, Deep Source $\xi = 0.7$, $\eta = 0.9$

3. <u>Summary</u>

The problem studied in this work consists of a layered medium perfectly bonded upon a rigid half space. Elastic medium is subjected to antiplane strain displacement field in such a way as to simulate a simple model of a strike-slip fault. The frequency spectra are devised for an arbitrary number of layers. Particular examples of one, two and three layers are evaluated in detail.

It is confirmed that deeper source excites higher frequency modes more compared to the shallow source. Overall sensitivity of resulting motions on the depth of the source appears to be greater as the number of layers increases. Contribution of locally standing waves (which decay exponentially with distance from the source) to kinetic energy density appears significant within the distance from the source compared to one thickness of the top layer.

Inversion of the results in time domain for a single layer implies that the displacement field due to locally standing waves is substantial compared to the contribution from progressing wave for distances from the source which are less than two thicknesses of the layer.

Comparison of rotation and displacement spectra shows that for progressing waves, the average ratio of rotation spectrum versus the product of the frequency and displacement spectrum, remains constant for a wide range of frequencies. This suggests the possibility of determining the rotation spectrum from known displacement spectrum and vice versa.

REFERENCES

Achenbach, J.D. (1973). Wave Propagation in Elastic Solids, Amsterdam, North-Holland.

Alsop, L.E. (1966). Transmission and Reflection of Love Waves at Vertical Discontinuity, Journ. Geophys. Res., 71, No. 16, 3963-3384.

Anderson, J.G., and M.D. Trifunac (1977). Current Computational Methods in Studies of Earthquake Source Mechanisms and Strong Ground Motion, Proceedings of the Symposium on Applications of Computer Methods in Engineering, 2, 929-940, L.C. Wellford, Jr. (ed.), Los Angeles, U.S.C.

Apsel, R.J., J.E. Luco, and J.A. Orcutt (1977). Body Wave and Surface Wave Propagation in a Multi-Layered Half-Space, abstract, Annual Meeting of the Seismological Society of America, Sacramento.

Brigham, E.D. (1974). The Fast Fourier Transform, New Jersey, Prentice-Hall.

Carrier, G.F., M. Krook, and C.E. Pearson (1966). Functions of a Complex Variable, MacGraw Hill, New York.

Haskell, N.A. (1953). The Dispersion of Surface Waves on Nulti-Layered Media, Bull. Seism. Soc. Amer., 43, 17-34.

Helmberger, D.V. (1974). Generalized Ray Theory for Shear Dislocations, Bull. Seism. Soc. Amer., 64, 45-64.

Herrera, I. (1964). On a Method to Obtain a Green's Function for a Multi-Layered Half-Space, Bull. Seism. Soc. Amer., 54, 1087-1096.

Holloway, J.L., Jr. (1958). Smoothing and Filtering of Time Series and Space Fields, Advances in Geophys. 4, 351-389.

McGarr, H., and L.E. Alsop (1967). Transmission and Reflection of Rayleigh Waves and Vertical Boundaries, Jour. Geophys. Res. 72, No. 8, 2169-2180.

Newmark, N.M., and E. Rosenblueth (1971). Fundamentals of Earthquake Engineering, Prentice Hall, New Jersey.

Sneddon, I.H. (1973). The Uses of Integral Transforms, McGraw-Hill, New York.

Trifunac, M.D., and A.G. Brady (1976). Correlations of Peak Acceleration, Velocity and Displacement with Earthquake Magnitude, Distance and Site Conditions, Earthquake Engr. Struct. Dyn., 4, 455-471.

Trifunac, M.D. (1976). Tectonic Stress and Source Mechanics of the
    Imperial Valley, California, Earthquake of 1940, Bull. Seism. Soc.
    Amer., 62, 1283-1302.

Wong, H.L., and M.D. Trifunac (1978). Synthesizing Realistic Ground
    Motion Accelerograms, U.S.C., Department of Civil Engineering,
    Report No. CE 78-07, Los Angeles.

APPENDIX A

An alternate approach to derive the representation for displacement field $v(x,z,\omega)$ due to input displacement $v(x=0,z,\omega)$ = $F(\omega)g(z)$ is shown here for the case of a single layer.

For a layer $x,y \in (-\infty,\infty) \times [0,h]$ the steady state wave motion is governed by

$$\left(\nabla^2 + \frac{\omega^2}{\beta^2}\right) v(x,z,\omega) = 0 \ , \qquad \nabla^2 \equiv \frac{\partial^2}{\partial x^2} + \frac{\partial^2}{\partial z^2} \ , \tag{A.1}$$

where ω and β represent the circular frequency and the shear wave velocity respectively. The boundary conditions are specified by

$$\frac{\partial v(x,0,\omega)}{\partial z} = 0 \tag{A.2}$$

$$v(x,h,\omega) = 0 \tag{A.3}$$

and

$$v(0,x,\omega) = F(\omega)g(z) \tag{A.4}$$

with $g(z)$ and $F(\omega)$ being the known functions.

The wave motion is antisymmetric with regard to x; thus, the sine Fourier transform is introduced (Sneddon, 1973)

$$\tilde{f}(\xi) = 2 \int_0^\infty f(x)\sin \xi x \ dx \tag{A.5}$$

$$f(x) = \frac{1}{\pi} \int_0^\infty f(\xi)\sin \xi x \ d\xi \ . \tag{A.6}$$

Application of the sine Fourier transform to equation of motion (A.1) implies

$$v_{zz}(\xi,z,\omega) + \left(\frac{\omega^2}{\beta^2} - \xi^2\right) \tilde{v} = -2\xi g(z)F(\omega) \tag{A.7}$$

At this point, one can extend v as an even function with respect to z=0. In particular, the extension over interval $4z_1 = 4h_1$ is shown in Figure 10a. Consequently

$$\tilde{v}_z(\xi,0,\omega) = \tilde{v}_z(\xi,2h,\omega) = 0 \qquad (A.8)$$

The last property calls for application of finite cosine transform defined by a pair (Sneddon, 1973)

$$\tilde{v}*(\xi,n,\omega) = \int_0^{2h} \tilde{v}(\xi,z,\omega)\cos \frac{n\pi z}{2h} z \qquad (A.9)$$

$$\tilde{v}(\xi,z,\omega) = \frac{1}{2h} \tilde{v}*(\xi,0,\omega) + \frac{1}{h} \sum_{n=1}^{\infty} \tilde{v}*(\xi,n,\omega)\cos \frac{n\pi z}{2h} \qquad (A.10)$$

It follows then from (A.7) and (A.8) that double transform of the displacement field is given by

$$\tilde{v}*(\xi,n,\omega) = - \frac{2\xi F(\omega)}{q^2 - \left(\frac{n\pi}{2h}\right)^2} b_n \quad , n=1,2, \ldots, \qquad (A.11)$$

where

$$q^2 \equiv \frac{\omega^2}{\beta^2} - \xi^2 \qquad (A.12)$$

$$b_n = \int_0^{2h} g(z)\cos \frac{n\pi\zeta}{2h} d\zeta \quad . \qquad (A.13)$$

Application of inversion (A.10) to (A.11) provides

$$\tilde{v}(\xi,z,\omega) = - \frac{2F(\omega)}{h} \sum_{n=1}^{\infty} \frac{\xi b_n}{q^2 - \left[\frac{n\pi}{2h}\right]^2} \cdot \cos \frac{n\pi z}{2h} \quad . \qquad (A.14)$$

To satisfy boundary condition (A.3) one replaces n in (A.14) by 2m-1, i.e.,

$$\tilde{v}(\xi,z,\omega) = -\frac{2F(\omega)}{h} \sum_{m=1}^{\infty} \frac{\xi}{q^2 - \left[\frac{(2m-1)\pi}{2h}\right]^2} b_{2m-1} \cdot \cos\frac{(2m-1)\pi}{2h} \quad . \tag{A.15}$$

Inversion of sine Fourier transform implies

$$v(x,z,\omega) = -\frac{2F}{h\pi} \sum_{m=1}^{\infty} b_{2m-1} \cdot \cos\frac{(2m-1)\pi z}{2h} \cdot \int_0^{\infty} \frac{\xi\sin\xi x}{q^2 - \left[\frac{(2m-1)\pi}{2h}\right]^2} d\xi \quad . \tag{A.16}$$

The ξ-integral is evaluated next. Since the integral is an even function of ξ one has

$$I = \int_0^{\infty} \frac{\xi\sin\xi x}{q^2 - \left[\frac{(2m-1)}{2h}\right]^2} d\xi = \frac{1}{q_i} \int_{-\infty}^{\infty} \frac{\xi e^{i\xi x}}{q^2 - \left[\frac{(2m-1)\pi}{2h}\right]^2} d\xi \quad . \tag{A.17}$$

The poles of the integrand are determined by

$$q^2 - \left[\frac{(2m-1)\pi}{2h}\right]^2 = 0 \quad , \qquad m=1,2,3,\ldots \tag{A.18}$$

or

$$\frac{\omega^2}{\beta^2} - \xi_m^2 = \left[\frac{(2m-1)\pi}{2h}\right]^2 \quad , \qquad m=1,2,\ldots \tag{A.19}$$

The last equation is recognized as the frequency equation for a single layer model derived earlier by different methods. Assuming that

$$\xi_m^2 > 0 \quad , \qquad\qquad m \le n$$
$$\xi_m^2 < 0 \quad , \qquad\qquad m > n \tag{A.20}$$

The poles for the I-integral (A.17) are depicted by Figure (A1). The real poles ξ_m, m=1, ..., n represent progressive modes while the pure imaginary poles $i\xi_m$, m=n+1, ... lead to locally standing waves.
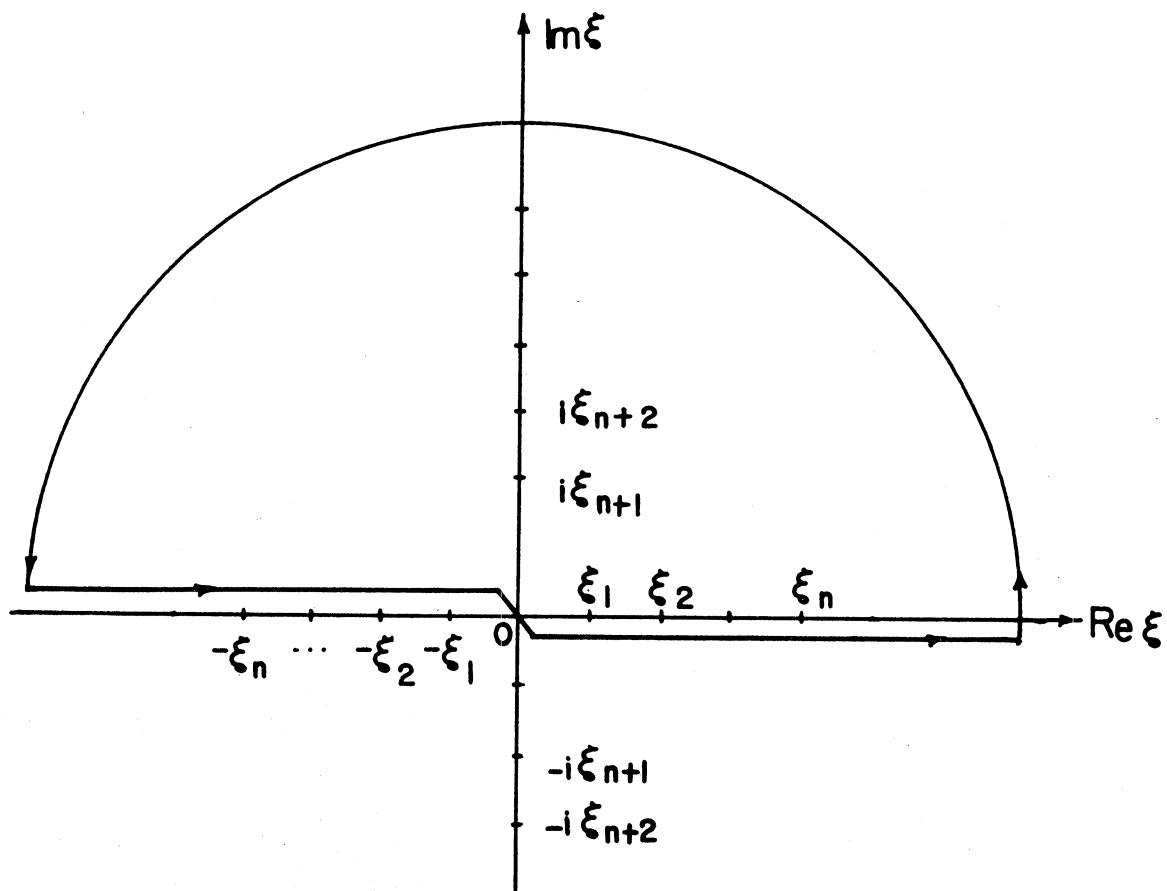
Figure A1. Poles in Complex ξ-Plane

Application of Jordan's lemma (Carrier, et. al., 1966) leads to the value of the ξ-integral

$$I = \int_0^\infty \frac{\xi \sin \xi x}{q^2 - \left[\frac{(2m-1)\pi}{2h}\right]^2} \, d\xi = -\frac{\pi}{2} \left\{ \sum_{m=1}^n e^{i\xi_m x} + \sum_{m=n+1}^\infty e^{-\xi_m x} \right\} ,$$

(A.21)

where ξ_m is the solution of equation (A.19). Consequently, the displacement field (A.16) is given by

$$v(x,z,\omega) = \frac{F(\omega)}{h} \left\{ \sum_{m=1}^n b_{2m-1} \cdot \cos \frac{(2m-1)\pi z}{2h} e^{i\xi_m x} \right.$$

$$\left. + \sum_{m=n+1}^\infty b_{2m-1} \cdot \cos \frac{(2m-1)\pi z}{2h} e^{-\xi_m x} \right\} .$$

(A.22)

This is the same result derived earlier by modal analysis.

Smoothing Procedure

Given a sample of m discrete values $\{y_t\}$, t=0,1,2, ... m-1, a smoothed set $\phi\{y_t\}$, t=0,1,2, ..., m=1 is defined by (Holloway, 1958) as

$$\phi\{y_t\} = \sum_{k=-n}^{n} w_k u_{t+k} \ , \qquad t=0,1,2, \ ..., \ m-1 \ , \qquad (B.1)$$

where $\{w_k\}$, k=0,±1,±2, ..., ±n represents a set of weighting functions such that

$$\sum_{k=-n}^{n} w_k = 1 \ , \qquad (B.2)$$

and n is assumed to be an even number.

In present works, the weighting function is chosen to be of triangular type (Figure B1)

$$w_k = \frac{1}{\sigma} w(kS)\delta(\Delta - kS) \ , \qquad k=0,±1,±2, \ ..., \ ±n \qquad (B.3)$$

where

$$w(s) = \begin{cases} 1 + s/a \ , & -a < s \leq 0 \\ 1 - s/a \ , & a > s \geq 0 \end{cases} \qquad (B.4)$$

$$s = a/n \qquad (B.5)$$

$$\sigma = \sum_{k=-n}^{n} w_k \qquad (B.6)$$

and δ represents the Dirac's delta function. In particular, "n" and "a" are assumed to be 20 and 10, respectively.

It is seen from (B.1) that the set of m sampled values of $\{y_t\}$ must
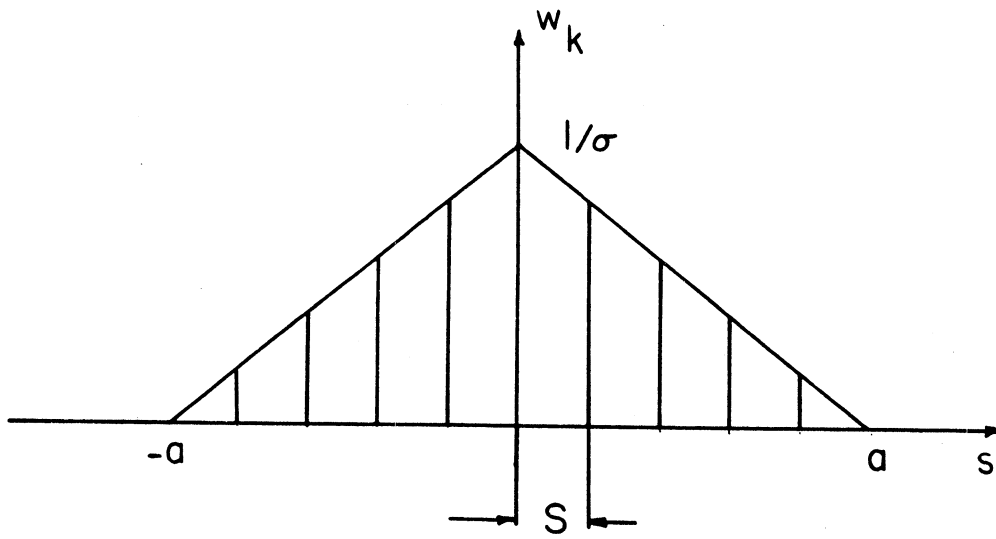
Figure B1. Weight Function for Smoothing
Procedure

be approximately extended to the left and to the right with respect to the first (t=0) and the last (t=m-1) sample value respectively. This is done in the following manner

$$y_k = 0 \qquad , \qquad k = -n, \ldots, -1$$
$$y_{ki} = y_{m-1} \qquad , \qquad k = m, m+1, \ldots, m-1+n \quad .$$

(B.7)

The process of smoothing can be repeated until satisfactory appearance of the data is achieved.

APPENDIX C

The Inverse of the Fourier Transform

Numerical calculation of $v(x,z,t)$ in (2.19) calls for the application of the Fast Fourier Transform algorithm (FFT).

To avoid difficulties stemming from the ramp function (2.2) which has the Fourier transform in generalized sense only and is unbounded for $\omega=0$ (2.6), the input function $f(t)$ in (2.5) is replaced by an equivalent one, $f_e(t)$. The equivalent input function is defined by (Figure C1)

$$f_e(t) = \begin{cases} f_+(t) , & 0 \leq t \leq T/2 \\ -f_+(t) , & -T/2 \leq t \leq 0 \end{cases} \tag{C.1}$$

Function $f_+(t)$ is given by

$$f_+(t) = \begin{cases} H(t - a_1)f(t - a_1) , & 0 \leq t \leq T/4 \\ f_m(t) , & T/4 \leq t \leq T/2 \end{cases} \tag{C.2}$$

where $H(\ )$ represents the Heaviside step function, $f_m(t)$ stands for an axial symmetrical extension of $H(t - a_1)f(t - a_1)$ about axis $t = T/4$, T is a period, and a_1 is a parameter to be specified later. Therefore, the equivalent function is an odd periodic function, i.e.,

$$f_e(-t) = -f_e(t)$$
$$f_e(t + T) = f_e(t) \tag{C.3}$$

In particular, for a set of parameters for function $f(t)$ ($a = 1$, $t_0 = 1s$, $v_0 = 1m$, $\zeta = 0.2$) period T is chosen to be $T = 8a_1 + 4$. The time response due to equivalent input function $f_e(t)$ provides response due to original
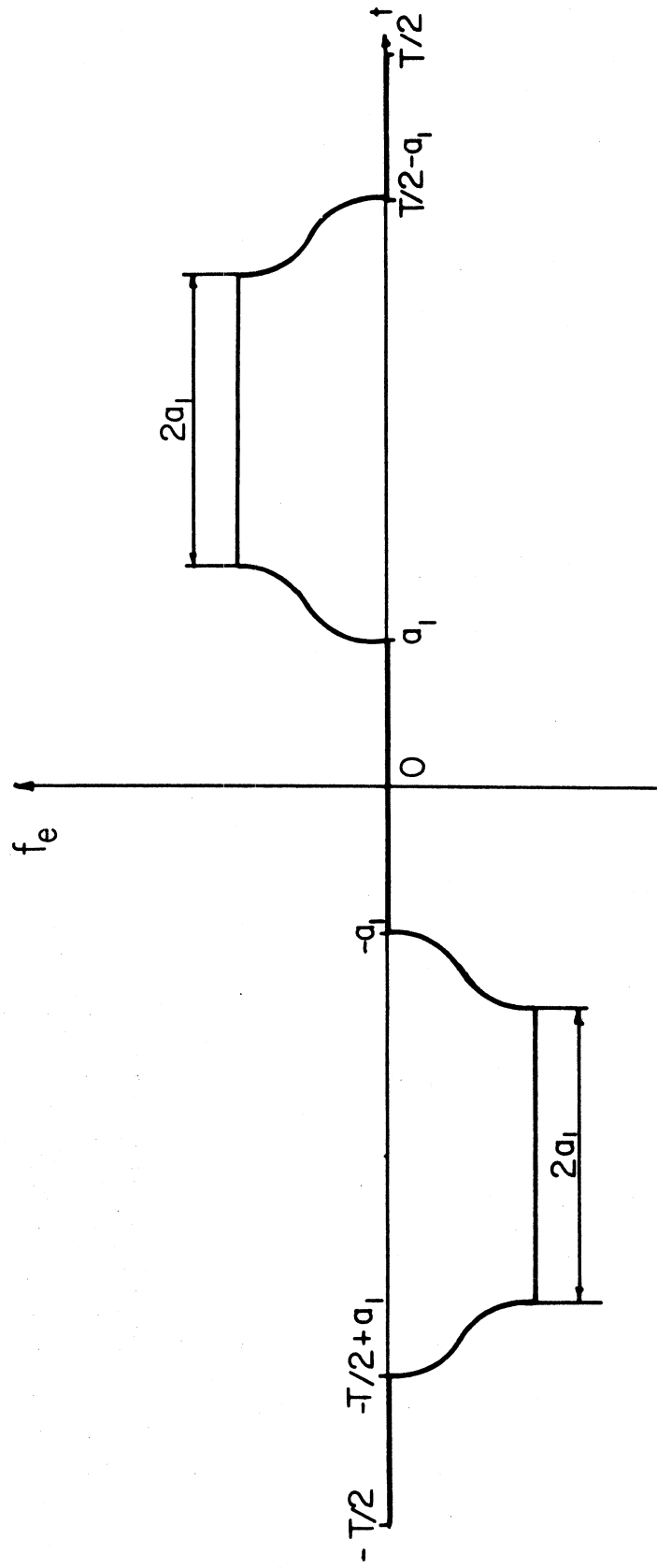
Figure C1. Equivalent Input Function

input $f(t)$ in region $a_1 \leq t \leq T/4$. It should be noted that the Fourier transform of $f_e(t)$ reduces to Fourier series expansion, i.e.,

$$F_e(\Omega) - i\pi \sum_n b_n [\delta(\Omega - \Omega_n) - \delta(\Omega + \Omega_n)] \qquad (C.4)$$

$$\Omega_n = \frac{2\pi}{T} n \quad , \quad b_n = \frac{2}{T} \int_{-T/2}^{T/2} f_e(t) \sin\frac{2n\pi}{T} t \ dt \quad . \qquad (C.5)$$

Choosing sampling interval $\Delta\Omega = \pi/60$ it follows that required period $T = 120$. Number of sampling points is taken to be $N = 2^9 = 512$, which implies the Nyquist frequency $\Omega_{Ny} = \frac{N}{2} \cdot \Delta\Omega$. Consequently, the sampling increment in time domain is specified by $\Delta T = T/N$. The program for evaluation of the Fast Fourier transform in this work is a slight modification of the program supplied by Wong and Trifunac (1977).